



universität  
wien

# DISSERTATION / DOCTORAL THESIS

„Atomic structure of low-dimensional materials and their  
*in-situ* transformation in the transmission electron  
microscope“

verfasst von / submitted by  
Ursula Ludacka, BSc MSc

angestrebter akademischer Grad / in partial fulfilment of the requirements for the degree of  
Doktorin der Naturwissenschaften (Dr. rer. nat.)

Wien, 2019/ Vienna 2019

Studienkennzahl lt. Studienblatt /  
degree programme code as it appears on the student  
record sheet:

A 796 605 411

Dissertationsgebiet lt. Studienblatt /  
field of study as it appears on the student record sheet:

Physik

Betreut von / Supervisor:

Assoz. Prof. Dr. Jani Kotakoski



## Abstract

Transmission electron microscopy is a powerful method for investigating the atomic structure of thin specimens, and especially two-dimensional materials, such as graphene, hexagonal boron nitride (hBN), molybdenum disulfide (MoS<sub>2</sub>) and other structures at the nanometer length scale. However, a transmission electron microscope (TEM) is not limited to simple investigation of these structures in a static form, but can also be used to study their deformation under external manipulation, such as mechanical strain, or due to electron irradiation induced structure altering processes during the observation.

In this thesis, TEM has been used as a purely investigatory tool for a number of studies. For example, studying the density of Si impurities in monolayered hBN, introduced during chemical vapour deposition (CVD) growth. As hBN is prone to chemical etching processes due to its chemical structure, investigating this material with high energy electrons can be rather challenging. Using fast techniques in a scanning transmission electron microscope (STEM), enabled imaging of Si impurities not caused by electron irradiation, with only a minor trade-off in resolution. For investigating and quantifying the amount of intercalated potassium within carbon nano-onions, different TEM techniques were applied, including *Z*-contrast STEM imaging with atomic resolution and electron energy loss spectrometry (EELS). The latter is a powerful tool to generate spectrum images in which only electrons of a certain energy loss are used for image formation, leading to the characterization of the elemental distribution in a specimen. These measurements revealed the spatial distribution of intercalated potassium within and around the carbon nano-onions

By switching to reciprocal space via diffraction mode in a TEM, additional details of the studied structures can be revealed. It is demonstrated that the intensity distribution within the diffraction pattern depends on the chemical elements building up the materials, and that the three-dimensional structure

of nominally two dimensional (2D) materials can be revealed. It is shown that a pristine 2D material tends to exhibit ripples in the third dimension, which can be oriented by applying mechanical strain providing means for controlling the material properties inside the microscope.

Due to the high-energy electron irradiation during TEM investigation, structural damage of the studied materials is often inevitable. One manifestation of this is knock-on damage that can lead to increasing disorder of an initially crystalline graphene sample, assisted by *in-situ* heating of the sample during the experiment. The lattice disorder can also be observed through changes in the diffraction pattern; starting from a pattern with distinct spots that corresponds to the ordered structure, it gradually changes through the spreading of the spots along the azimuthal angle until a structure with a closed ring, corresponding to a completely disordered 2D structure, emerges.

In conclusion, the work presented in this thesis both demonstrates the use of TEM for the structural characterization of low-dimensional materials as well as its capability for tracking structural changes while they occur inside the microscope, which provides new means for tailoring novel materials for applications.

Transmissionselektronenmikroskopie ist eine vielseitige Methode um Proben auf atomarer Ebene zu erforschen. Im Speziellen 2D Materialien, wie Graphen, hBN, MoS<sub>2</sub> und weitere Nanostrukturierte Materialien sind für diese Art der Untersuchung besonders geeignet. Doch nicht nur statische Untersuchungen lassen sich in TEMs durchführen, sondern auch die Messung dynamischer Vorgänge, wie Zugversuche aber auch Umbauprozesse im Material, aufgrund der Bestrahlung mit hochenergetischen Elektronen.

In dieser Arbeit wurden verschiedene Bauformen von TEMs verwendet. Ein modernes STEM wurde verwendet um die Dichte von Si Verunreinigungen in monolagigem hBN, zu untersuchen. Diese wurden aufgrund von chemical vapour deposition (CVD) Wachstum in das Material eingebracht. Doch hBN ist ein nicht einfach zu untersuchendes Material in einem Elektronenmikroskop,

da es zu chemischen Ätzprozessen während der Elektronenbestrahlung kommt. Hier eignen sich insbesondere Methoden, die nur kurze Verweildauern des Strahls auf der Probe benötigen, wie zum Beispiel schnelle STEM Rastertechniken. Hier büßt man allerdings einen Teil der Bildqualität ein.

Für die quantitative Untersuchung von Kohlenstoff Nanozwiebeln wurden verschiedene TEM Techniken angewendet, allen voran  $Z$ -Kontrast STEM Aufnahmen und EELS. Mit letztgenannter Technik können zum Beispiel so genannte Spektrum Abbildungen aufgenommen werden. Hierbei werden, mithilfe eines EELS Spektrometers, nur Elektronen mit bestimmten Energieverlusten zur Bildgebung verwendet. Dadurch lässt sich die Verteilung von Kaliumatomen in Kohlenstoff-Nanozwiebeln bestimmen.

Ein weiterer Modus in der Elektronenmikroskopie, ist der Beugungsmodus, welcher Einblicke in den reziproken Raum gewährleistet. Hierbei können weitere Aspekte des zu Untersuchenden Materials enthüllt werden. Betrachtung der Intensitätsverteilung innerhalb eines Beugungsbildes, lässt Rückschlüsse auf die drei-dimensionale Struktur eines 2D Materials zu. Es zeigt sich, dass diese nicht flach sind, sondern verschieden ausgeprägte Korugationen aufweisen. Die im unbelasteten Material anfänglich randomisierte Verteilung der Wellen, lässt sich gezielt durch Anbringen einer äußeren Zugkraft, mithilfe eines Spezial TEM Probenhalters, beeinflussen.

Durch die, notwendigerweise hohe Energie, der in einem TEM eingestrahleten Elektronen, kommt es häufig zu unvermeidbaren Schäden an der Probe. Einer dieser Strahlungsschäden ist der so genannte Anstoßeffect, welcher zu Umbaueffekten in 2D Materialien führt. Diese verlieren dabei zunehmend ihre geordnete Struktur und werden in ungeordnete, 2D Strukturen umgewandelt. Auch diese Prozesse lassen sich mithilfe des Beugungsmodus beobachten. Anfänglich scharfe Beugungspunkte, werden schwächer in ihrer Intensität und es kommt zu einer allmählichen Ausbildung eines ringförmigen Beugungsbildes.

Zusammenfassend sei gesagt, dass die in dieser Arbeit demonstrierten TEM Methoden, Grundlagen für die Erzeugung von 2D Materialien mit massgeschneiderten Eigenschaften, aufzeigt.



# Acknowledgements

During the last years I had the opportunity to work with an amazing group of people. I experienced growth on both a scientific and personal level. It was an eventful, adventurous journey, bringing me to amazing places in the world and a trek into the very depth of electron microscopy. For all this I want to say: thank you!

First and foremost I want to express my sincere gratitude to my supervisor Prof. Jani Kotakoski, during the course of this thesis he offered immense amounts of support and wise guidance. He also motivated me to dare things and trusted me with my decisions. His supervision not only guided me through the years of my Ph.D. thesis, but also helped me gain confidence and knowledge in the vast world of microscopy.

In these regards I want to as well thank Prof. Christian Rentenberger and Prof. Thomas Waitz who showed great trust in my abilities and who first introduced me to electron microscopy. I also want to thank Prof. Jannik Meyer for many fruitful discussions and helping me in my first steps with the Titans. Thank you for encouraging me on my path!

All of this would not have been possible without my great work group who made these years simply fly by and created tons of great memories, both from a scientific point of view as well as in terms of friendship: Clemens Mangler, who definitely is king of the lab (and vacuum) and whom I could always count on when coming up with new ideas and technical help, Kimmo Mustonen, Viera Skakalova, Christian Kramberger, Toma Susi, Bernhard Bayer, Kenan Elibol, Andreas Mittelberger, Giacomo Argentero, Stefan Hummel, Stefan Noisternig,

Mukesh Tripathi, Christoph Hofer, Oleg Domanov, Gregor Leuthner, Heena Inani, Georg Zagler, Alexander Chirita and Daniel Scheinecker. Thank you as well for the unforgettable conferences, which I look back to with a big smile. Regina Pinter, thank you for your patience and the help regarding administrative things.

As well I want to thank my new colleagues from EMAT for their support during my first months here in the group and Liesbet Laurens for her help with the final layout of the thesis.

Last but not least, I want to thank my wonderful parents for all their time and support through the years with all the ups and downs life is surprising us with.

# Contents

<b>1</b>	<b>List of publications</b>	<b>9</b>
<b>2</b>	<b>Introduction</b>	<b>11</b>
<b>3</b>	<b>Materials &amp; methods</b>	<b>13</b>
3.1	Materials . . . . .	13
3.1.1	Graphene . . . . .	16
3.1.2	Hexagonal boron nitride (hBN) . . . . .	20
3.1.3	Molybdenum disulfide (MoS <sub>2</sub> ) . . . . .	21
3.1.4	Van der Waals heterostructures . . . . .	24
3.1.5	Corrugations in 2D materials . . . . .	28
3.2	Sample preparation . . . . .	30
3.3	Electron microscopy . . . . .	34
3.3.1	Electron–matter interactions . . . . .	39
3.3.2	Transmission electron microscopy (TEM) . . . . .	43
3.4	2D materials in the electron microscope . . . . .	61
<b>4</b>	<b>Results</b>	<b>69</b>
4.1	Substitutional Si impurities in monolayer hexagonal boron nitride	69
4.2	Analysis of K intercalated carbon nano-onions . . . . .	73
4.3	Electron scattering factors in transmission electron microscopy	79
4.4	Ripples in different 2D materials . . . . .	82
4.4.1	Energy filtered analysis of diffraction patterns . . . . .	98
4.5	Pulling graphene . . . . .	100

4.6 Defects in graphene . . . . .	115
<b>5 Conclusion</b>	<b>125</b>
<b>A – Python code for evaluation of diffraction pattern</b>	<b>131</b>

# Chapter 1

## List of publications

1. **U. Ludacka**, M. R. A. Monazam, C. Rentenberger, M. Friedrich, U. Stefanelli, J. C. Meyer and J. Kotakoski. In-situ control of graphene ripples and strain in the electron microscope. *npj 2D Materials and Applications*. 25. 1-6 (2018). DOI: 10.1038/s41699-018-0069-z
2. T. Susi , J. Madsen, **U. Ludacka**, J. J. Mortensen, T. J. Pennycook, Z. Lee, J. Kotakoski, U. Kaiser and J. C. Meyer. Efficient first principles simulation of electron scattering factors for transmission electron microscopy. *Ultramicroscopy*. 197. 16–22 (2018). DOI: 10.1016/j.ultramic.2018.11.002
3. R. Kozubek, M. Tripathi, M. Ghorbani-Asl, S. Kretschmer, L. Madauß, E. Pollmann, M. O’Brien, N. McEvoy, **U. Ludacka**, T. Susi, G. S. Duesberg, R. A. Wilhelm, A. V. Krasheninnikov, J. Kotakoski, and M. Schleberger. Perforating freestanding molybdenum disulfide mono-layers with highly charged ions. *The Journal of Physical Chemistry (JPC) Letters*. 10. 904–910 (2019). DOI: 10.1021/acs.jpcllett.8b03666
4. M. R. A. Monazam, **U. Ludacka**, H.-P. Komsa, J. Kotakoski. Substitutional Si impurities in monolayer hexagonal boron nitride. *Applied Physics Letters*. 115. 071604 (2019). DOI: 10.1063/1.5112375

5. M. Sojkova, K. Vegso, N. Mrkyvkova, J. Hagara, P. Hutar, A. Rosova, M. Caplovicova, **U. Ludacka**, V. Skákalová, E. Majkova, P. Siffalovic, M. Hulman. Tuning the orientation of few-layer MoS<sub>2</sub> films using one-zone sulfurization. *ACS Applied Materials & Interfaces*. (2019) – submitted
6. **U. Ludacka**, D. Scheinecker, M. R. A. Monazam, C. Rentenberger and J. Kotakoski. Measuring and comparing intrinsic corrugations of 2D and their van der Waals heterostructures in an electron microscope – in preparation

## Chapter 2

# Introduction

"We strongly hope that the irradiated specimen resembles the pristine the same way a grilled chicken is supposed to resemble rather a healthy one than a carbonized one." – Otto Scherzer

2D materials show promise for a large range of future applications. They also provide an exciting opportunity for the microscopist, because their inherent thinness exposes all atoms for imaging. In this thesis, three generations of electron microscopes are used for investigating these fascinating but delicate materials:

- a Phillips CM200, an instrument from the year 1995, sometimes in combination with an even older specimen holder (from the mid 1970's)
- a FEI Titan 80-300(S)TEM from the year 2006, a powerful instrument, equipped with a monochromator, image corrector and a post-specimen energy filter as well as high angle annular dark field (HAADF) detector and charge-coupled device (CCD) cameras.
- and the most recent microscope, a Nion UltraSTEM 100, a dedicated STEM equipped with HAADF and medium angle annular dark field (MAADF) detectors.

These instruments enable viewing the specimen over a wide range of magnifications, going up to  $50\,000\,000\times$ . In addition to real space imaging, the

crystalline structure and morphology of low-dimensional materials can also be observed in the reciprocal space. For a vast range of applications this is the preferred method, as deviations from an ideal structure are more easy to quantify. In this regard, 2D materials exhibit an exceptional characteristic: the number of scattering events of the incoming electrons can in good approximation be assumed as one, and therefore scattering intensities can be easily interpreted. Because of this, for materials consisting of only one atomic layer but different elements, the chemical composition manifests in the diffraction pattern.

The glimpse into the reciprocal space also allows for the observation of the three-dimensional shape of 2D materials. Applying strain via a straining holder and investigating the change in interatomic distances reveals that even with rather low-tech equipment deep insight is possible.

This material group is linked by restrictive dimensional properties, but their intrinsic properties, such as atomic bonding, electrical and mechanical behavior differ strongly. Similar as bulk materials, 2D materials come as insulators, conductors and semi-conductors.

Graphene and hBN have a similar crystal structure and are both one atomic layer thick. Apart from the structure, their material properties are rather contrary. Graphene shows semi-metal and hBN insulating behavior. MoS<sub>2</sub> on the other hand is a bit of an outlier, as it is three atom layers thick.

# Chapter 3

## Materials & methods

### 3.1 Materials

2D materials are promising candidates for drastically minimizing the size of structural components of many mechanical and electronic applications. Their important characteristic is the high aspect ratio: the lateral dimension of these materials can be up to millimeters, compared to a thickness of one or few atoms, they can be seen as infinitesimally thin. Depending on the observed size scale, this idealized view can sufficiently describe the material for many of applications. In terms of nomenclature, a material that is as thin as its smallest repeating structural unit, is often referred to as a 2D material. This work is focused on investigating these materials, their out-of-plane shape and atomic structure. To investigate 2D materials, transmitting techniques such as TEM are extremely powerful, as they are thin enough to be easily shone through by an electron beam.

Any real 2D material is either grown on or transferred onto a supporting structure for experiments. On a substrate the sample is fully supported. These substrates can be other 2D materials or conventional bulk materials. However, substrates can interfere with the materials' properties. This can be avoided by creating freestanding structures that are only partially supported using perforated substrates. For TEM, perforated structures of amorphous carbon,

gold or SiN are typically used. The freestanding areas of 2D materials are less restricted in their out-of-plane direction but have strong boundary conditions where they are supported by another material [1].

Before the discovery of graphene, attempts were made to describe the hypothetical properties of such materials and whether they can exist or not [2]. In early predictions for superconducting materials by Peierls and Landau in 1935 and 1937, a model with 2D layers of normal and superconducting phases were used [3, 4]. In the thermodynamically preferred state, these layers repeatedly branch out in their out-of-plane direction, thus minimizing their surface energy [3, 4, 5]. Since 2007 [6, 7] it is known that 2D materials exist in quasi-flat arrangement on substrates and as freestanding structures.

In the following sections the most studied 2D materials, graphene, MoS<sub>2</sub>, hBN and their heterostructures will be introduced. The natural occurrence of these materials is often in form of layered materials, such as graphite, containing a number of graphene layers. While writing with a graphite pen or a piece of graphite itself, graphene is most likely produced, although likely not in an experimentally useful form [8]. In its natural habitat, MoS<sub>2</sub> is also a graphite-like crystal. In form of a 2D material on substrate it has been of experimental research interest since the 1960's [9]. 'White graphene', as hBN is sometimes called, comes in a number of crystalline forms. The most stable of the BN polymorphs is the hexagonal form which, similar to graphite and MoS<sub>2</sub>, has a layered structure.

### The crystallography of a 2D material

The variety of different crystal structures in 2D materials is significantly lower compared to bulk materials. Lacking the third dimension, the possible structures are reduced to five possible crystal lattices. These Bravais lattices are sets of discrete points, defined by the primitive vectors  $\vec{a}_1$  and  $\vec{a}_2$  and generated by discrete transformations. An arbitrary point  $\vec{\mathbf{R}}$  in the lattice is described by the relation

$$\vec{\mathbf{R}} = n_1\vec{a}_1 + n_2\vec{a}_2, \quad (3.1)$$

where  $n_1$  and  $n_2$  are integers. The five possible Bravais lattices belong to four crystal families: oblique, which belongs to the monoclinic crystal family, rectangular and centered rectangular which are both of the orthorhombic family, hexagonal of the hexagonal family and square of the tetragonal family [10]. For all 2D materials investigated in this study, their pristine structure exhibits a hexagonal structure in the two planar dimensions.

### **Applications of 2D materials**

Starting from applications in microelectronic devices [11], over sensor material [12] and as well some rather curious inventions like graphene-enhanced condoms [13], 2D materials raise interest in various disciplines. One aspect that makes graphene and MoS<sub>2</sub> extraordinarily attractive is their high Earth abundance [14, 15]. Especially graphene as a carbon allotrope can be easily mined. This is advantageous as graphene-based flexible electronic devices are of high interest for displays, light-emitting diodes, solar cells and field effect transistors [16]. Since graphene can be easily tailored on a small scale, it is applicable for nanoscale devices. For example in the field of quantum optics, as the size of the interfering particles grows larger, the grating size needs to shrink. Therefore, gratings made of graphene done by a focused ion beam can provide a solution [17].

There are attempts for using 2D materials as semi- or impermeable membranes for filtration purposes. Both graphene and MoS<sub>2</sub> show promising properties in this regard. The durability of such thin membranes is a drawback though. Bunch *et al.* investigated whether graphene can support pressure differences larger than atmospheric pressure [18]. A pristine sheet of monolayer graphene might also act as an impermeable membrane for even small atomic gases such as helium [19, 20]. Nanopores fabricated via removing several atoms would be small enough to filter ions from a liquid [21]. Additionally, such nanopores in graphene membranes would increase the liquid flux through the pores as compared to other materials, because the flux speed scales with the membrane's thickness. In the field of tunable nanopores, MoS<sub>2</sub> would be

an even more promising candidate [22] for example in life sciences for deoxyribonucleic acid (DNA) sequencing purposes [23]. Furthermore, such pores have already successfully been tested for water desalination by Heiranian *et al.* in 2015 [21].

There are also several applications where monolayer hBN can play an important role. One of them, like MoS<sub>2</sub>, is a solid mechanical lubricant for nanoscale devices, such as nanoelectromechanical or microelectromechanical systems [5]. These devices are in a size range where friction and adhesion become dominating. Such effects can lead to a massive degradation in the materials' performance [24]. As the characteristics of 2D materials can be influenced by the adjacent structures, so called van der Waals (vdW) heterostructures provide a wide field of applications for hBN. It is a suitable material for these heterostructures, especially with graphene as they have similar lattice parameters and both are in their pristine form free of dangling bonds [25]. Moreover, it has been observed that hBN as a substrate drastically decreases the intrinsic corrugations of graphene, which otherwise tends to conform to the structure of the underlying substrates [26, 27].

As mono- and few-layered MoS<sub>2</sub> and hBN are non-conductive, both having electronic band-gaps, they may be used for photoluminescence devices. Tran *et al.* studied single photon emission from localized defects in hBN mono- as well as in multilayers [28]. In the case of MoS<sub>2</sub>, the size of the band-gap can be tailored via layer thickness. It also affects the photoluminescence leading to a more intense effect for decreased thickness [15, 29, 30]. The size of the band-gap and therefore the electronic properties of monolayer MoS<sub>2</sub> are also strain-dependent, which has been shown by several authors [31, 32, 33, 34].

### 3.1.1 Graphene

Graphene, an allotrope of carbon, is the epitome of a 2D material and can be described entirely as a surface [35]. As the basic structural unit of graphite it is almost omnipresent. Nonetheless, in form of a freestanding material it was not believed to exist until its discovery in 2004 [6]. As this was the starting

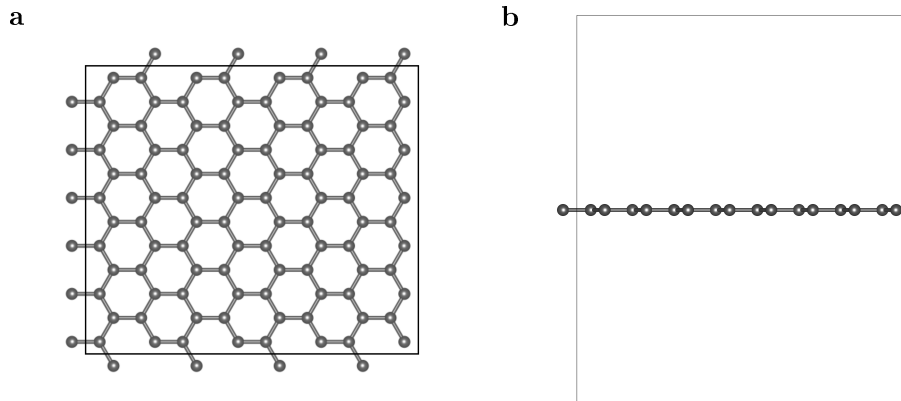


Figure 3.1: **Graphene lattice.** (a) Top view and (b) side view.

point for a new category of materials, Geim and Novoselov were awarded the Nobel Prize in Physics in 2010. However, in an adsorbed form, deposited on metallic surfaces graphene has been known to exist for at least 40 years [36].

### The graphene lattice

Carbon has atomic number six and four electrons in its outermost shell. Graphene is an arrangement of carbon atoms and a member of the space group  $p6/mmm$ . The notation  $p$  stands for plane group, combining point group symmetry and in-plane translation. The point group notation  $6$  describes the hexagonal lattice and  $m$  the mirror planes [37]. In the honeycomb structure of graphene, each carbon atom has three nearest neighbors. The atoms form strong covalent  $\sigma$  bonds within the plane. The one remaining electron per atom contributes as a  $\pi$  electron to the electronic properties of graphene. The carbon atoms are arranged in a regular hexagonal structure as depicted in figure 3.1 (a). Even though each single carbon atom is indistinguishable from the others, to build up the hexagonal lattice, a two-atomic base is needed, where each atom belongs to a different sublattice. The distance between two neighboring atoms is 0.142 nm. The Wigner-Seitz primitive cell of the graphene lattice, formed by the reciprocal lattice vectors  $\mathbf{b}_1$  and  $\mathbf{b}_2$  and is indicated by the two differently shaded triangles in figure 3.2 (a). The reciprocal lattice and the construction of the first Brillouin zone (BZ) are shown in figure 3.2 (b) as the blue shaded

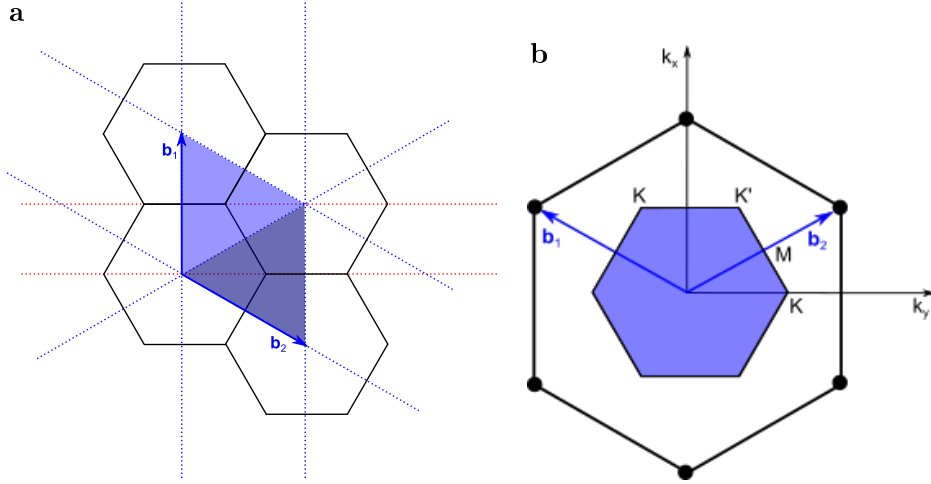


Figure 3.2: **Lattice structure of graphene.** (a) Construction of the Wigner-Seitz primitive cell. (b) Reciprocal space lattice of graphene with the first BZ.

area. A reciprocal representation of the lattice shows the same symmetries as the real space lattice.

Valence and conduction band in graphene are in direct contact, which results in the lack of a band-gap and a (semi-) metallic behavior [38]. At the point where the two bands of the dispersion relation meet, the electrons behave like massless Dirac particles [39]. They are fermions or spin 1/2 particles, and are described by the 2D Dirac equation, rather than the Schrödinger equation. This results in a delocalization and therefore an exceptional high electron mobility [40].

### Real graphene—deviations from the ideal 2D crystal

In real crystals defects are inevitable. Creating a single defect costs a certain amount of energy, described by the change in enthalpy  $\Delta H$ . On the other side, forming one increases the entropy  $S$ , at a temperature  $T$ . In a system in equilibrium these two processes compensate each other and there is no change in the overall free energy

$$\Delta G = \Delta H - T\Delta S. \quad (3.2)$$

For any crystal at a temperature  $T > 0$  K a finite concentration of defects exists [41]. In reality, their concentration strongly depends on the synthesis process [42]. Highly oriented graphite (HOPG) e.g. (see section 3.2) provides graphene with a low defect concentration.

In the idealized case graphene is assumed to be an infinitely extended perfect crystal. In reality it can contain different point and extended defects. For example, the growth can start at many different locations simultaneously. After some time, grains of different orientation meet and a grain boundary forms. The structure along the grain boundary is in graphene often formed by a pentagon-heptagon structure [43].

### **Out-of-plane corrugations**

Often graphene is depicted as a flat material, even if it is freestanding. But the deviation from a flat structure might actually enable the existence of 2D materials [44]. Indeed, Landau and Peierl showed that a divergent contribution of thermal fluctuations in low-dimensional crystal lattices should lead to displacement of atoms that are in the range of interatomic distances at any finite temperature [45, 2, 4]. If graphene is suspended, this can cause strain in the material that can lead to an aligned ripple pattern. In unstrained graphene intrinsic ripples are randomly orientated. Via specifically designed substrates, strain can be applied in a controlled manner, as was shown by Elinski *et al.* [46].

### **Properties of graphene**

Graphene can be described with some superlatives, especially regarding its electrical and mechanical properties. However, as a 2D material it is basically its own surface, its properties strongly depend on the substrate, local electronic environment and mechanical deformations [35, 47, 48]. Graphene exhibits a thermal conductivity in the order of 5000 W/mK [49], high (theoretical) electron mobility at room temperature of 250 000 cm<sup>2</sup>/(Vs) and a

sheet resistivity of  $10^{-6} \text{ } \Omega\text{cm}$ , which is less than the resistivity of silver [49]. While the early measurements in 2005 by Novoselov *et al.* gave a value of merely  $15\,000 \text{ cm}^2/(\text{Vs})$  for both electrons and holes in mechanically exfoliated graphene [39], in 2011 Tanabe *et al.* measured a carrier mobility value of  $45\,000 \text{ cm}^2/(\text{Vs})$  for epitaxially grown graphene on SiC(0001) [50].

With nanoindentation, using an atomic force microscope (AFM), mechanical properties of graphene could be measured, leading to a value for the Young's modulus of  $E = 1.0 \pm 0.1 \text{ TPa}$ . As the Young's modulus is defined for bulk materials via  $E = \sigma/\varepsilon$ , with  $\sigma$  the uniaxial stress and  $\varepsilon$  the uniaxial strain, an effective thickness of  $0.335 \text{ nm}$  (interlayer distance of graphene) had to be assumed [49].

### 3.1.2 Hexagonal boron nitride (hBN)

Boron-nitride (BN) has, like carbon, a long list of different applications, and it exists in various crystalline forms. Parallels to the carbon allotropes can be drawn as BN exists in layered, cubic and tubular structures [51]. One of them, hBN, has a similar structure as graphite. Its single layer is sometimes referred to as white graphene. Single- and few-layer flakes of hBN on Ni(111), Pd(111), and Pt(111) substrates were already found in 1995 [52]. The first atomically thin freestanding hBN was synthesized by Han *et al.* in 2005 [38]. Further investigations followed by Han *et al.* in 2008 [53].

#### The hBN lattice

The lattice of hBN has a two-atomic basis, with one boron and one nitrogen atom, and is a member of the space group  $\text{p}6_3/\text{mmc}$ . The point group notation  $6_3$  describes the hexagonal lattice with alternating atom types, m is for the mirror planes and, c a glide plane [37]. The lattice is shown in figure 3.3 (a).

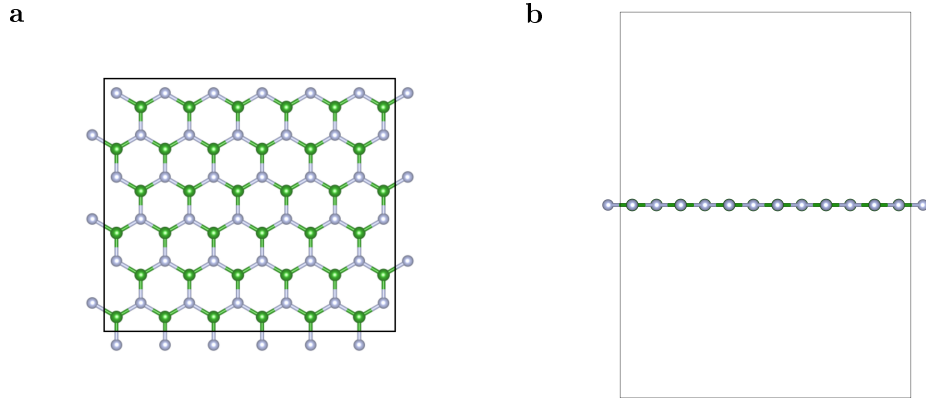


Figure 3.3: **hBN lattice**. Boron in gray and nitrogen in green. (a) Top view and (b) side view.

In the in-plane direction hBN has strong, partially ionic, covalent  $sp^2$  bonds. It is an insulator with a bandgap of about 5.9 eV [25, 54]. Defects in hBN have been described by many authors [43, 55, 56, 57, 58, 59], and carbon and oxygen impurities were shown by Krivanek *et al.* [60]. It has been predicted by Liu *et al.* that a large number of defects in the lattice lead to buckling in hBN, as can be observed in graphene [43]. Similar to graphene it is expected to be smooth but corrugated when freestanding without dangling bonds and charge traps [61]. Due to the ionic nature of the bonding, bonds between atoms of the same type increase the formation energy of defects [59].

### Properties of hBN

A monolayer of hBN has a high elastic modulus of between 0.5 – 0.6 TPa and a thermal conductivity of 390 WmK [62]. Similar to graphene, the values of thermal conductivity measured for monolayers highly exceed those of the bulk material [35]. It exhibits thermal and chemical stability up to 2950°C [51, 63].

### 3.1.3 Molybdenum disulfide ( $\text{MoS}_2$ )

$\text{MoS}_2$  is one of about 40 layered transition metal dichalcogenides (TMDs) [5]. TMDs are a typically semi-conducting sub-group of 2D materials of the type  $\text{MX}_2$ . M denotes a transition metal atom (Mo, W, ...) and  $\text{X}_2$  a pair of chalcogens.

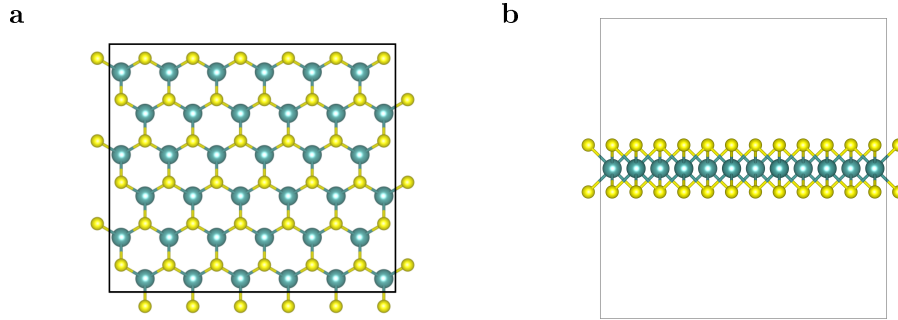


Figure 3.4: **MoS<sub>2</sub> lattice.** Molybdenum atoms are depicted in blue and sulfur atoms in yellow. (a) In top view the lattice has hexagonal shape. (b) In side view the lattice shows its three-dimensional character.

gen atoms (S, Se, or Te). The research of MoS<sub>2</sub> dates back to the 1960s, when chemically exfoliated nanosheets of TMDs were investigated. After the successful extraction of freestanding single layer graphene, the research of nanoscale TMDs experienced an upsurge [9]. First reports of successful CVD synthesis of monolayer MoS<sub>2</sub> were reported by Najmaei *et al.* in 2013 [64]. According to Wu *et al.* [65], however, the production of high quality monolayer MoS<sub>2</sub> is still a daunting process.

In top view, MoS<sub>2</sub> exhibits a hexagonal symmetry and is therefore a member of the hexagonal space group p6mmc [37]. However, the individual MoS<sub>2</sub> units of the primitive unit cell themselves exhibit trigonal prismatic symmetry ( $D_{3h}$ ) [37]. What distinguishes MoS<sub>2</sub> from the aforementioned 2D materials is its thickness of three atoms. Thus, it is sometimes called a pseudo-2D material [66]. The atomic structure of MoS<sub>2</sub>, where each Mo atom of is surrounded by three pairs of S atoms is shown in figure 3.4.

The bandgap of MoS<sub>2</sub> is directly related to the number of layers. The indirect bandgap of the bulk material is  $\sim 1$  eV [66]. The position of the indirect band-gap depends on the number of MoS<sub>2</sub> layers on top of each other. It shifts with decreasing layer thickness towards a direct band-gap. The energy difference between the bulk band-gap to the monolayer band-gap is about 0.6 eV [15, 12, 67]. This bandgap transition is caused by effects of quantum confinement and resulting in hybridization between the  $p_z$ -orbitals of the sulfur

atoms and the  $d$ -orbitals of the molybdenum atoms [12, 15, 14]. For crystal thicknesses below 100 nm these effects of quantum confinement were predicted by Neville already in 1976 [68]. The band-gap transition manifests also in enhanced photoluminescence in monolayered MoS<sub>2</sub> as compared to bulk MoS<sub>2</sub> [66].

Zhou *et al.* were the first to study and describe intrinsic structural defects in CVD-grown MoS<sub>2</sub>. Point defects such as vacancies, antisite defects and adatoms, but as well grain boundaries and edges have been reported [69, 65]. Zhang *et al.* distinguished six different point defects in CVD grown MoS<sub>2</sub>: monosulfur vacancies, disulfur vacancies and antisite defects where a molybdenum atom substitutes a S<sub>2</sub> column, or a S<sub>2</sub> column substitutes a molybdenum atom. Similar to defects in graphene, there exists a variety of different ring compositions within the lattice, such as 5|7, 4|4, 4|6, 4|8 and 6|8 rings [65].

An important characteristic for the quality of a monolayer of MoS<sub>2</sub> is the grain size, as mechanical properties, like stiffness and strength scale with the grainsize [65]. Due to their prevalence in CVD-grown samples, their influences on the material's properties have been investigated in detail. In MoS<sub>2</sub> they strongly affect the optical properties.

It can be expected that, similar to graphene, the combination of structural defects and thermal influence induce corrugations to a freestanding monolayer of MoS<sub>2</sub>. These corrugations might slightly alter the electronic properties [65]. Substrate-induced corrugations in single layer MoS<sub>2</sub> on a substrate were reported by Kim *et al.* [70].

## **Properties of MoS<sub>2</sub>**

Monolayer MoS<sub>2</sub> is a semiconductor with a bandgap which can be tuned in various ways without changing the chemistry of the material. One of these approaches is strain engineering. Where possible gap openings in graphene start at high strains of about 20%, much less strain is needed in MoS<sub>2</sub>. Various types of strain engineerings have been demonstrated. According to Feng *et al.*, MoS<sub>2</sub> exhibits an isotropic in-plane elasticity and the bandgap depends only on

the 2D hydrostatic strain invariant to the linear order [33]. The carrier mobility of mechanically exfoliated MoS<sub>2</sub> was found to be between 200 – 500 cm<sup>2</sup>/(Vs) at elevated temperatures and 0.5 – 3 cm<sup>2</sup>/(Vs). It behaves like a heavily doped semiconductor with an activation energy of > 0.6 eV [38].

### 3.1.4 Van der Waals heterostructures

Van der Waals heterostructures are stackings of different materials held together by van der Waals forces. These forces include the interaction of electrostatic dipoles (Debye forces) and London dispersion forces [71]. The associated interlayer forces range between 40 and 70 meV [35] and are thus much smaller than covalent bonding energies of 200 – 600 meV [35]. They are nevertheless sufficiently strong to keep the layers of the vertical stack together [72].

#### The lattice mismatch & moiré pattern

The orientation of the partaking materials influences the electronic properties of the resulting vdW heterostructure. In stackings of two graphene layers, a lattice twist angle of 1.05° leads to superconductivity, according to Lian *et al.* [73]. The influence of the lattice mismatch in form of a twist angle could also be observed in other vdW heterostructures. As Aziza *et al.* described, in a vertical vdW heterostructure of MoS<sub>2</sub> and graphene, the twist angle can be used to intentionally alter the electronic properties of MoS<sub>2</sub>, whereas those of graphene remain unaltered [74].

Moiré patterns are observed whenever two or more lattices with a mismatch with respect to each other are placed on top of each other. If the lattice orientations are close, the moiré effect results in a striped pattern with a small period (see figure 3.5). For larger mismatch angles (see the diffraction pattern for graphene on hBN figure 3.5 (c)) the moiré effect results in a striped pattern with a large period as shown in figure 3.5 (d), for hBN on graphene.

Looking at the diffraction pattern of vdW heterostructures of graphene and MoS<sub>2</sub> in figure 3.5 (e) and (f), two different lattice spacings can be observed

easily. However, in the corresponding high resolution electron microscopy (HRTEM) image, graphene cannot be seen, although it can be revealed by the fast fourier transformation (FFT) of the area (inset in figure 3.5 (g)). This is because graphene with its carbon atoms is such a weak scatterer compared to  $\text{MoS}_2$  that its presence remains hidden in slight brightness variations.

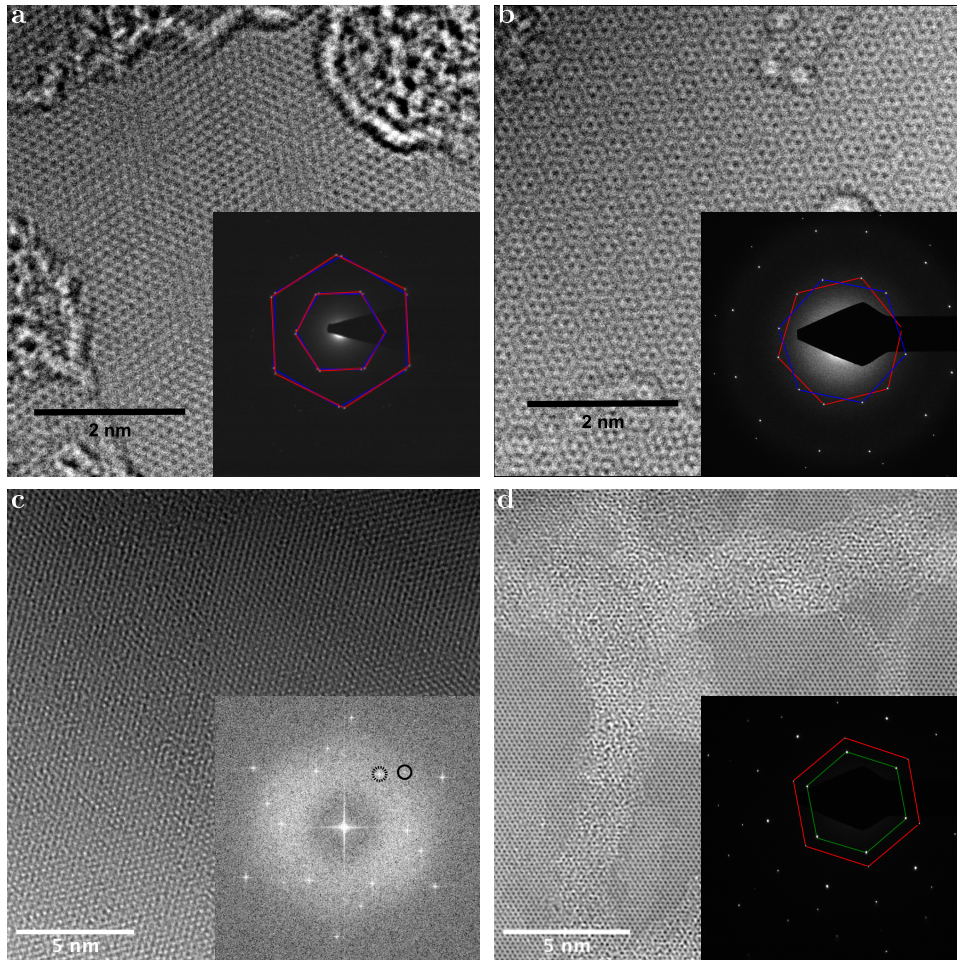


Figure 3.5: **Moiré patterns of different lattice mismatches of a graphene hBN heterostructure.** (a) Moiré pattern of a heterostructure of graphene and hBN with a small lattice orientation mismatch and (inset) the according diffraction pattern (red - graphene, blue - hBN). (b) Moiré pattern of a heterostructure of graphene and hBN with a larger lattice orientation mismatch and (inset) the according diffraction pattern (red - graphene, blue - hBN). (c) HRTEM image of a heterostructure of graphene and  $\text{MoS}_2$ . (inset) Diffractogram of (c). (d) Energy filtered HRTEM image of a heterostructure of graphene and  $\text{MoS}_2$  (inset) the according diffraction pattern (red - graphene, green -  $\text{MoS}_2$ ).

Due to their different electronic properties, heterostructures between graphene and hBN or MoS<sub>2</sub> can open a variety of new applications. The misorientation of the two stacked crystal lattices can alter the electronic structure by introducing superlattice minibands or even a small band gap in the band structure of graphene [75, 76]. In the case of closely aligned graphene-hBN vdW heterostructures, a band-gap in graphene can appear. This happens due to the local breaking of the carbon superlattice symmetry [77, 78, 79, 80]. The point was however opposed by Xue *et al.*, who argued against a hBN-induced band-gap opening in graphene, even locally [81]. Angle-resolved photoemission spectroscopy measurements conducted by Diaz *et al.* in 2015 did not reveal significant charge transfer doping due to a possible change in the Dirac cone [82]. During investigations in 2013 by Yang *et al.* of graphene on hBN, an extra set of Dirac points induced by the moiré pattern was established [83].

### **Properties of vdW heterostructures**

The electron mobility of electrons in graphene in a vdW heterostructure on top of hBN is at least 10 000 cm<sup>2</sup>/(VS) [78] which is lower than the average experimental values for pristine graphene (section 3.1.1) and much below the theoretically predicted value. In contrast, Dean *et al.* conducted electronic transport measurements and obtained a carrier mobility of 60 000 cm<sup>2</sup>/(VS), concluding that hBN serves as the perfect substrate for graphene-based electronics [61]. According to Wang *et al.* the presence of hBN in such a heterostructure significantly reduces charge density inhomogenities, compared to SiO<sub>2</sub> as a substrate material [5].

In conclusion, graphene and hBN are to each other perfect substrates due their smooth, dangling bond-free surfaces and their complementary electronic properties [81]. Unfortunately the fabrication of monolayer hBN with sufficiently high quality is still a work in progress, which drastically limits the potential applications [5]. It would be ideal to be able to align the two lattices with respect to each other with desired lattice mismatch angles. Unfortunately this remains an unsolved issue [5].

According to Jin *et al.* there is no influence to the electronic properties when graphene is transferred onto a monolayer of MoS<sub>2</sub>. Graphene behaves in this compound as pristine graphene independent of the lattice mismatch angle, and the Dirac point of graphene is situated within the bandgap of MoS<sub>2</sub>. When growing MoS<sub>2</sub> on graphene, MoS<sub>2</sub> tends to align with the graphene lattice [84].

### Sample preparation

CVD growth of each material separately and subsequent transfer on top of each other, is an efficient method to prepare heterostructure samples of 2D materials [5]. Another possibility is to directly grow the materials on top of each other. However, in case of MoS<sub>2</sub>, growth on a (mono- and multilayered) graphene substrate, wrinkles and different types of defects can lead to unwanted side effects, such as the growth of adlayers of MoS<sub>2</sub> [5]. As 2D materials and their vdW heterostructures are the thinnest imaginable materials, contamination in form of hydro-carbon compounds can interfere with subsequent measurements. Unfortunately they are an omnipresent nuisance as they tend to be inevitable during preparation processes. For graphene-based structures, hydrocarbon contamination tends to accumulate into pockets of submicron size with a round base shape [85]. Heating the materials to up to 300°C before creating the heterostructure helps to reduce the size of the pockets. Their properties depend on the elastic properties of the partaking materials and are independent of the trapped contamination [85, 86, 87]. It is possible that in the direct vicinity of the bulged material, local stresses appear [86].

### Applications

2D materials are prone to external influences such as Coulomb interactions with adlayers or substrates. These screening effects directly affect for example the bandgap of MoS<sub>2</sub>. However, electrostatic screening effects are sufficiently weak in a vdW heterostructure between single-layer graphene and MoS<sub>2</sub> such that the bandgap of MoS<sub>2</sub> is not significantly altered. Due to this renormal-

ization effect MoS<sub>2</sub> is a promising candidate for optoelectronic devices [88]. Heterostructures between graphene and hBN and those between graphene and TMDs are of interest for applications for field effect transistor (FET)s, performance optoelectronics and photovoltaic devices [89, 90, 91]. Nevertheless, the microscopic mechanisms how graphene acts and adapts to its substrate, be it on a bulk substrate or another 2D material, have still not been conclusively studied [92].

### 3.1.5 Corrugations in 2D materias

The lack of the third dimension causes 2D materials to often exhibit different properties than the corresponding bulk form. Similar to a linen sheet, such thin structures are susceptible to out of plane distortions, which adds a certain three-dimensionality to the structure. Corrugations are also caused by lattice defects, as suggested already in 1993 by Carraro *et al.* for general 2D membranes [93].

The non-flatness of 2D materials is a controversial topic. In principle the non-flatness of suspended 2D materials can be measured by scanning probe techniques. However, these mechanical probing techniques are problematic for investigating freestanding 2D materials, because the interaction with the probe inevitably leads to the deformation of the membrane, even in so-called non-contact modes. Therefore, only a method with negligible interaction between the probe and the specimen allows unperturbed *in-situ* investigation of corrugations in 2D materials.

### Previous studies on corrugations of 2D materials

In 2007 ripples in freestanding graphene were computationally predicted to be randomly distributed by Fasolino *et al.* [94]. However, also on substrates graphene tends to adapt to the underlying surface [26]. In 2007 Meyer *et al.* estimated the range of intrinsic ripples for suspended graphene sheets to be several nanometers. They used TEM as a method of contactless investigation

and compared the mean inclination of monolayered graphene membranes to bilayered graphene. In 2011 Brivio *et al.* used this method to investigate corrugations of monolayered MoS<sub>2</sub> [95]. Corrugations add one degree of freedom to the atomically thin system and can lead to otherwise unexpected scatter of data in measurements. For simplicity they are often omitted in theoretical studies [96, 97]. However, they may stabilize these otherwise fragile structures, especially in their freestanding form [98]. Geringer *et al.* observed that the lateral wavelength of corrugations in monolayer graphene deposited onto SiO<sub>2</sub> substrate have a wavelength of 10 – 25 nm with an amplitude of about 1 nm [99]. Similar results were measured by Warner *et al.* in 2013 with an amplitude of 0.5 – 2 nm [98].

As mentioned in the sections 3.1.1 and 3.1.2, lattice defects are, if present, an additional cause for out-of-plane buckling. It might be tempting to assume that an increasing number of defects leads inevitable to higher buckling of the material, but in fact an increase of defect concentration reduces it due to strain release between neighboring dislocations. Additionally, the buckling itself leads to a massive strain release [43]. Strain is another major cause for rippling of 2D membranes. Either in localized form due to defects, or on a larger range due to external stress [100]. The role of the latter type of strain is going to be discussed in detail in section 4.5.

### **Corrugations in other 2D materials than graphene**

Studies on corrugations of 2D materials other than graphene are rather rare, possibly due to lack of suitable samples. For example, good quality single layered crystals of hBN are much rarer than those of graphene, that is meanwhile produced in industrial quantities. As mentioned before for MoS<sub>2</sub> a study similar to Meyer *et al.* [7] has been conducted [95].

### Out-of-plane corrugation in vdW heterostructures

It can be assumed that if two materials are brought in contact their mechanical properties and even the atomic structure is altered. According to literature, the intrinsic corrugations of monolayer graphene are suppressed in heterostructures [99, 101, 102, 103, 81, 26, 27]. Yang *et al.* reported that graphene exhibits a corrugated structure on hBN. It was further shown that the interaction between the two layers is weak, resulting in low internal frictional forces [83].

## 3.2 Sample preparation

As low-dimensional materials tend to be quite delicate, sample preparation is particularly challenging. Properly prepared samples can save time and nerves. Because 2D material have a high surface-to-bulk ratio, cleanliness of the samples is extremely important. To avoid contamination, there are three general rules:

1. Clean tools: Beakers, tweezers and other tools need to be carefully cleaned. It can be recommended that beakers are cleaned with the same liquids that are later filled into these beakers.
2. Clean liquids: All used liquids should be taken fresh from clean sources. It is also often advantageous to filter freshly prepared solutions (e.g. iron(3)chloride ( $\text{Fe}_3\text{Cl}$ ) solution).
3. Proper rinsing: All freshly prepared specimen should be rinsed carefully and properly to avoid residues of any type.  $\text{Fe}_3\text{Cl}$  for example can lead to needle-like structures on the sample.

All specimen investigated in this thesis were made freestanding on perforated films, and most of them were made from CVD-grown samples. To compare possible differences originating from preparation processes, additional specimen were produced by exfoliation. In the case of graphene the source material

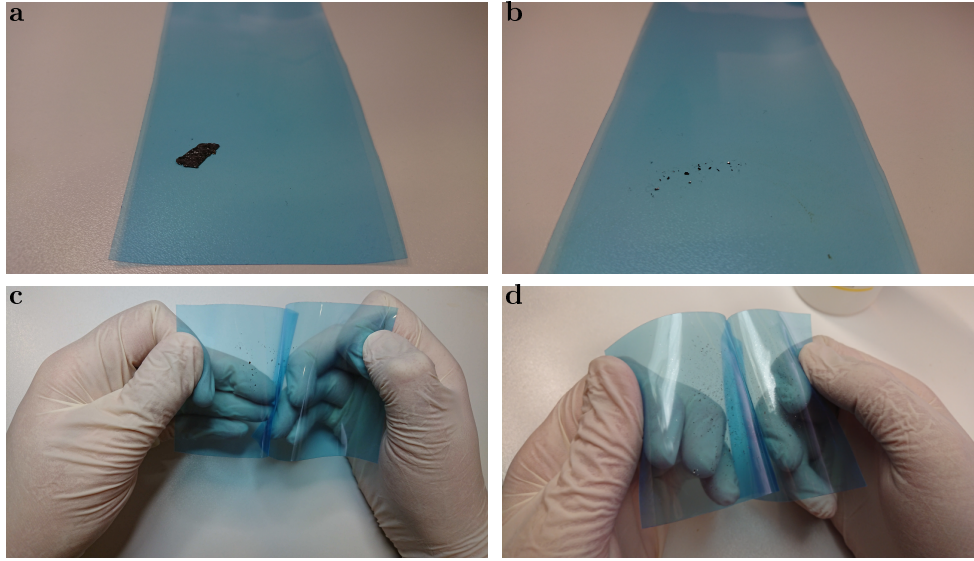


Figure 3.6: **Scotch tape method.** (a) Adhesive tape with a piece of HOPG on top of the sticky side. (b) After removing HOPG, small crystallites remain on the adhesive tape. (c) At the start of the exfoliation process two parts of the tape are attached and subsequently detached. Crystallites between the two sides of tape are torn apart. This process is repeated at slightly different positions. (d) After repeating this process several times the sticky side is covered with small pieces of thinned-out graphite crystals.

is highly oriented pyrolytic graphite (HOPG). Similar crystals are available for the preparation of different 2D materials.

### Mechanical Exfoliation

The best known method for exfoliation is the so called "Scotch tape" method. To produce the 2D specimen, a crystal is placed on the adhesive tape. When the tapes are detached, parts of the crystal stick on each side. This process can be applied until there are only thin parts of the material left, and the material is distributed over the two pieces of tape, as shown in figure 3.6.

One piece of tape is gently pressed onto a cleaned  $1 \times 1 \text{ cm}^2$  Si chip with a silicon oxide (SiO) layer of a known thickness. After pressing and detaching the Si chip from the adhesive sheet, it will be investigated under a visible light microscope. Here the thickness of the SiO layer is crucial, as it helps to distin-

guish layers with depicted thickness. A thickness of 300 nm has been proven as providing the highest contrast between the monolayer and the Si substrate. This contrast difference is only  $\leq 10\%$ , depending on the wavelength [104]. As one layer of 2D material has a defined absorption and the absorption depends linearly on the number of layers, multilayers can be identified by a defined contrast difference.

Unlike its sibling graphene, hBN is relatively hard to find through the oculars of a visible light microscope due to its weak light absorption. The contrast on regularly used substrates is extremely weak. Combined with difficult CVD synthesis procedures, studies with monolayer hBN remain rare [105]. Despite challenges, hBN specimen can be produced through mechanical exfoliation [106]. It has been observed by Xu *et al.* that mechanically exfoliated hBN sheets appear to have fewer defects than those produced by chemical methods [107].

### **Chemical vapor deposition (CVD)**

CVD growth of 2D materials provides larger quantities of 2D material than the mechanical exfoliation technique. A drawback of this method is that the growth typically starts from several crystallization seeds simultaneously. From these seeds monolayers with arbitrary orientations emerge. This can lead to monolayered, but polycrystalline material. Despite difficulties, CVD processes are used for synthesizing monolayer hBN flakes [108]. But the resulting monolayers of hBN are often highly polycrystalline and sometimes contain multilayer regions [108]. Similar challenges occur during CVD growth processes of monolayered MoS<sub>2</sub> [109].

### **Suspended 2D materials**

All specimen investigated here were suspended onto commercially available TEM grids (Quantifoil<sup>®</sup>). For the following experiments those were metal (typically gold) grids covered by holey amorphous carbon film. The diameter

of the grid was 3 mm and the thickness of the carbon film about 12 nm. The transfer process for exfoliated and CVD grown samples onto these grids are similar. Exfoliated samples are typically smaller than CVD grown ones. For the transfer of a flake from a substrate, a TEM grid is placed onto the substrate, so that the flake is in a suitable position. Subsequently, a droplet of isopropanol was used to eliminate the air gap between the holey carbon foil and the flake. The  $\text{SiO}_x$  layer was then etched in a potassium hydroxide solution. Finally, several rounds of washing in water and isopropanol were done.

All hBN samples were grown on Cu foil, whereas the  $\text{MoS}_2$  specimen were grown on  $\text{SiO}_x$ . Similar as for the exfoliated samples, the air gap between the carbon film and the sample was eliminated using a drop of isopropanol. In case of Cu foil as support, it was etched in a  $\text{Fe}_3\text{Cl}$  solution. Depending on the concentration, this step could take up to 12 h. Then the sample was rinsed several times in deionized water to wash away the  $\text{Fe}_3\text{Cl}$  residues. This step was followed by rinsing the grid in isopropanol.

### **Preparation of vdW heterostructures**

As the commercially available ready-to-use CVD grown graphene specimen on TEM grids are of suitably high quality, they were used in most graphene experiments and also to prepare the vdW heterostructures. The production of these samples is similar to the transfer process described using empty TEM grids.

### **Customized sample carrier**

To apply strain on a specimen, a TEM stretching holder is needed. By this purpose TEM grids were glued to Al platelets with vacuum-compatible epoxy glue and mounted as shown in figure 3.7. The preparation process is discussed in detail in section 4.5.

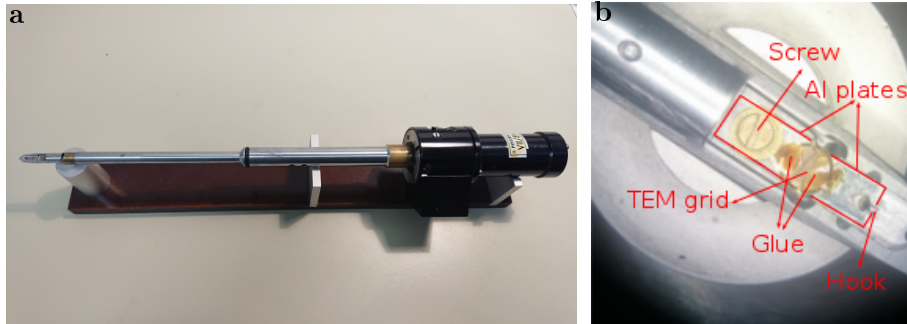


Figure 3.7: **TEM straining holder.** (a) The holder in top view, including straining unit at the tip, the O-ring seal (middle) and the motor-drive unit in the back. The motor-drive is connected to and controlled with the  $\beta$ -tilt at the microscope. (b) The straining unit adapted to strain TEM grids.

### 3.3 Electron microscopy

*The main source of this chapter is the book by David B. Williams and C. Barry Carter: "Transmission Electron Microscopy: A Textbook for Materials Science" [110].*

In electron microscopy the fact that a particle can be equally described as a wave leads to using electrons in a similar manner as visible light, to generate a magnified image of a specimen. The resolution of visible light microscopes is limited by the wavelength of light. Crystallography often uses X-ray diffraction methods, as the wavelengths are in the range of the investigated distances. However, diffraction methods are limited to observations in the reciprocal space. Furthermore, for X-ray scattering only interactions with electrons in the atomic shell of a specimen are relevant and interactions with nuclei can be often neglected [111]. Hence, using electrons as probing particles leads to additional insights as these interact both with the electrons in the atomic shells and the Coulomb potential of the atomic nuclei. Due to the short wavelength of electrons (pm range), the information and resolution limit can be extended beyond that of visible light, which spectrum ranges between 400 to 700 nm.

## The Electron Energy Resolution

To use electrons as probing particles they have to be accelerated in an electric field. The electron velocities  $v$  are directly related to the used high tension  $U$ . Fractions of the kinetic energy  $E$  of the electrons can be transferred to the specimen through elastic and inelastic scattering. Nuclei in the compound of the irradiated material can be irreversibly removed from this compound, if kinetic energy transferred elastically to a target atom surpasses the material specific so-called displacement threshold. The resulting deterioration of the sample is called knock-on damage. Because 2D materials are their own surfaces, and surface atoms in bulk materials have lower bonding energies, the displacement thresholds in 2D materials tends to be lower than those of bulk materials.

The wavelength  $\lambda$  of relativistic electrons is

$$\lambda = \sqrt{\frac{h^2 c^2}{eV[2m_e c^2 + eV]}}, \quad (3.3)$$

where  $h$  is the Planck,  $c$  the speed of light,  $e$  the elementary charge,  $V$  the acceleration voltage and  $m_e$  the electron mass. Common acceleration voltages range between 200 and 300 kV, which lead to damage in most 2D materials. Therefore a low acceleration voltage, ranging between 30–120 kV is mandatory to minimize knock-on damage [112, 113, 114].

In an electron microscope the acceleration voltage defines the wavelength of the electrons. In the relativistic case the de Brogli wavelength is

$$\lambda = \frac{hc\sqrt{1 - v^2/c^2}}{V}, \quad (3.4)$$

where  $v$  is the electron velocity. This relation is a reasonable approximation up to 100 kV. Table 3.1 lists properties of imaging electrons for the used acceleration voltages.

Table 3.1: Electron properties for regularly used accelerating voltages.

Acceleration voltage (kV)	Relativistic wavelength (pm)	Mass ( $\times m_0$ )	Velocity ( $\times 10^8$ m/s)
80	4.1757	1.1565	1.5061
100	3.7014	1.1956	1.6434
200	2.5079	1.3913	2.0844

### The electron gun

In the beginning of electron microscopy the electron source was a tungsten filament, like one used in an ordinary light bulb. Similar to the photon emission from a light bulb, electrons are emitted with a variety of energies ("colors"). Such a "white" electron beam reduces significantly the resolution due to chromatic aberration of the lenses, especially in the strongest one, the objective lens. The focal lengths of electrons with different wavelengths differ, causing a blurring of the focal point in the back focal plane of the lens. Therefore, the aim is a monochromatic electron beam.

An improvement was presented by a filament of lanthanum hexaboride ( $\text{LaB}_6$ ). The newest generation are field emission guns (FEG) which are sharp pointed electron emitters. In this type of electron source the temperature is kept at about  $44^\circ\text{C}$  for the standard field emission gun (FEG) and at about  $24^\circ\text{C}$  for so called cold FEG. All these electron sources act as cathodes in the electron beam generating unit referred to as electron gun. The cathode is surrounded by a Wehnelt cylinder or Wehnelt grid, set to a negative electric potential, that acts as the first anode (figure 3.8). This extraction potential extracts electrons from the electron gun. A Wehnelt cylinder is a cylindrical control electrode to regulate the brightness of an electron beam. A second anode, often referred to as accelerator, accelerates the electrons to the applied high tension. If the microscope is equipped with a monochromator, it is placed between the first and the second anode potential.

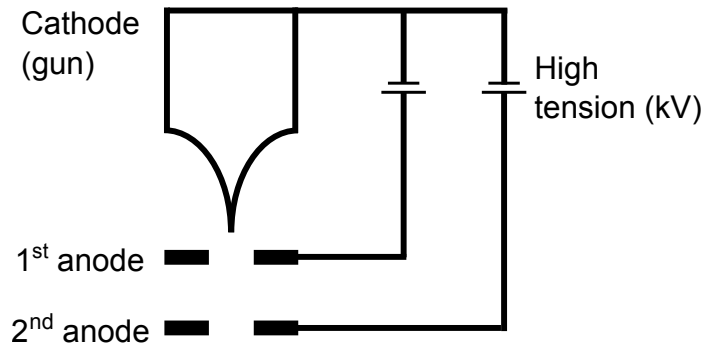


Figure 3.8: **Electron gun.** The electron gun acts as cathode. The first anode (extractor) extracts electrons from the cathode. Those are then accelerated to the target high tension (between 60 and 300 kV) in the second anode.

### Monochromator

To decrease the energy spread of the electron source, microscopes can be equipped with a monochromator. A commonly used simple design is the single Wien filter as shown in figure 3.9. Although every additional optical element introduces aberrations, those introduced by the Wien filter are less pronounced as compared to other designs [115]. This design also has the least beam current reducing effect [115]. In this type of monochromator the electrostatic potentials at extraction anode, gun lens and monochromator work as an einzel lens. Such system containing three electrostatic potentials acting as a focusing lens and can be operated in two different modes: decelerating and accelerating mode. In both modes the crossover of the electron beam is controlled only by the gun lens potential. In the Titan 80-300 (S)TEM used here, the extractor voltage, the first electrostatic lens at the anode plate, is usually at a constant value (for all following experiments at 4.5 kV). In decelerating mode the gun lens is operated in a potential range around 800 V and monochromator potential is set to 3.0 kV. In accelerating mode the potential at the gun lens is operated a range around 4.9 kV.

The working principle of a Wien filter is a combination of an electric and a magnetic quadrupole. The magnetic and the electric fields can be arranged such that in every point within the filter the field lines of both fields are or-

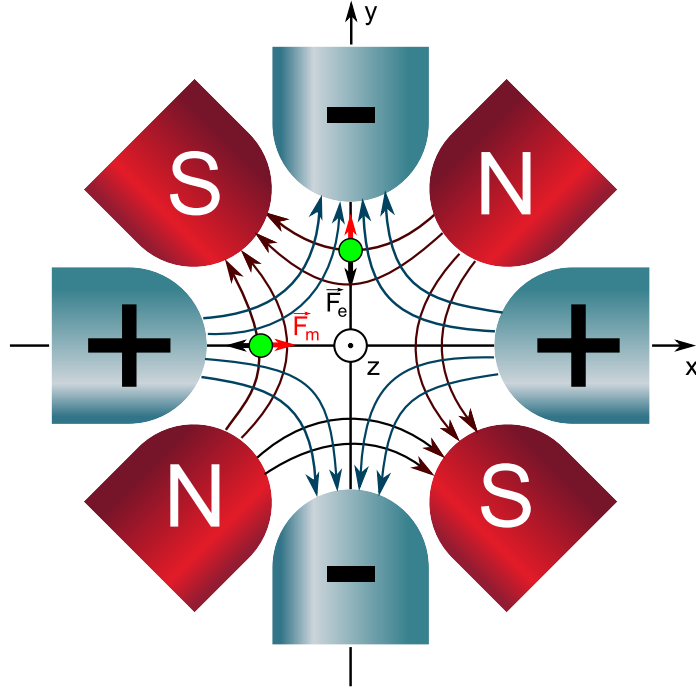


Figure 3.9: **Single Wien filter monochromator.** Arrangement of the electric (plus, minus) and magnetic (south, north) poles with the according field lines. Two electrons (green) with the resulting forces ( $\vec{F}_m$  and  $\vec{F}_e$ ) are shown. Electrons with a velocity smaller than  $v_0$  have trajectories towards the positive electrostatic potential ( $+V$ ), whereas those with a higher velocity towards the negative ( $-V$ ). Therefore the monochromated beam is of elongated shape and dispersed in its energy. The amount of energy dispersion is given by the length of the monochromator.

thogonal with respect to each other. The incoming electrons experience the superposition of the electrostatic field  $\vec{E}$  as the force  $\vec{F}_E = e\vec{E}$  and the Lorentz force  $\vec{F}_L = e\vec{v} \times \vec{B}$ . The velocity  $\vec{v}$  of the electrons is determined by the acceleration voltage. As the source has a thermal energy spread, the velocities of the extracted electrons are distributed. Only electrons in the narrow velocity range close to  $|\vec{v}_e| = |\vec{E}|/|\vec{B}|$  can travel through the monochromator system.

### Electromagnetic lenses

Analogously to optical lenses for photons, magnetic lenses are used to manipulate the electrons' trajectories. In contrast to optical lenses, magnetic ones

are limited to focusing. Fortunately electrons tend to diverge on their own. Secondly, according to [110]: "*...the best electromagnetic lens [is] the equivalent of using the bottom of a well known softdrink bottle as a magnifying glass. Another common description is that if the lenses in your own eyes were as good as our best electromagnetic lens, then you'd be legally blind.*" In the microscopes used for this work, the majority of lenses are electromagnetic lenses. Electrostatic lenses are found in the gun assembly whereas magnetic lenses of fixed magnetic field are usually found in simple electron microscopes. Electromagnetic lenses can be divided into round lenses and multipole lenses. The main image or probe forming lenses are of the first type whereas those for correcting aberrations are of multipole type. Frequently used multipole lenses are quadrupole lenses (such as previously described for the monochromator), hexapole and octopole lenses.

### **3.3.1 Electron–matter interactions**

#### **Scattering processes**

The basis of image formation in all electron microscopes are elastic and inelastic scattering processes. An electron hitting the specimen can be either not scattered at all, scattered once, several ( $> 2 \leq 20$ ) times or multiple ( $> 20$ ) times. With decreasing specimen thickness the number of scattering and re-scattering processes decreases. In 2D materials the probability of single scattering is the highest.

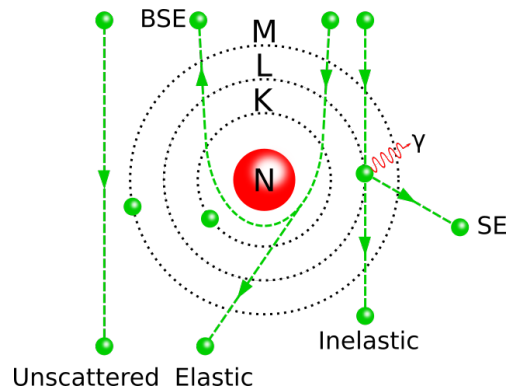


Figure 3.10: **Possible scattering processes for electrons.** Unscattered electrons pass the material unaffected, whereas backscattered electrons (BSE) experience scattering in reverse direction. Elastically scattered electrons can contribute to a variety of signals in a TEM, similar to inelastically scattered ones. Together with unscattered, elastically and inelastically scattered electrons contribute to the main TEM signal. Secondary electrons (SE) are usually not directly detected in TEM. X-rays ( $\gamma$ ) produced during these processes can be used for elemental analysis (EDX). K, L and M are the electron shells.

The possible scattering events are sketched in figure 3.10. For the sake of completeness the backscattered electrons as well as the secondary electron process are also shown. In TEM "unscattered electrons" are often referred to as "transmitted electrons", but this can lead to misconceptions, since in TEM all detected electrons are transmitted.

Inelastic scattering occurs as an interaction of the incoming electrons with the electrons of the specimen. The incoming electrons lose the energy equal to the equivalent necessary to lift a shell electron to a higher energetic state. As they fall back into their initial state, an X-ray is emitted, that can be detected in spectroscopic measurements. Also the electrons suffering from inelastic losses can be used in EELS or energy filtered TEM (EFTEM). The angular distribution of inelastically scattered electrons is  $\leq 10$  mrad and they are usually used for bright field (BF) imaging (sec. 3.3.2), as a part of the direct beam.

In assumption of a sufficiently temporal and coherent electron beam of wavelength  $\lambda$ , the conditions for positive interference of the electron partial

waves, scattered by the lattice planes of distance  $d_{hkl}$ , is described by Bragg's law

$$n\lambda = 2d_{hkl} \sin \theta_B, \quad (3.5)$$

where  $n \in \mathbb{N}$  and  $\theta_B$  the angle under which the Bragg condition is fulfilled. Electrons scattered under these conditions can be observed in an angular range between 10 to 50 mrad. They are used for dark field (DF) imaging in TEM or via an annular dark field (ADF) detector in STEM.

Elastic scattering (Rutherford scattering) is the scattering of an electron with a nucleus in the specimen. If the electron interacts with only the nucleus, the (unrelativistic) unscreened, differential Rutherford scattering cross section is

$$\frac{d\sigma}{d\omega} = \left( \frac{Z\alpha\hbar c}{4E_k(\sin \theta/\sigma)^2} \right)^2, \quad (3.6)$$

where  $\sigma$  is the differential cross section,  $\alpha$  the fine structure constant,  $E_k$  the non-relativistic kinetic energy and  $\theta$  the scattering angle. As the incoming electrons interact also with the atomic shell, the scattering cross section is altered due to these screening effects. The resulting screened Rutherford scattering cross section is

$$\sigma(\beta) = \frac{\left[ Z\lambda \left( \frac{a_0}{Z^{0.33}} \right) \left( 1 + \frac{E_0}{m_0c^2} \right) \right]^2}{\pi(a_0)^2 \left( 1 + \left( \frac{\beta}{\theta_0} \right) \right)^2}. \quad (3.7)$$

Here  $Z$  is the atomic number,  $\lambda$  the wavelength,  $\beta$  the semi-convergence angle,  $a_0$  the Bohr radius,  $\theta_0$  the screening angle and  $m_0$  the rest mass of the electron. The scattering cross section for Rutherford processes depends strongly on the atomic number  $Z$  of the nuclei. Electrons undergoing these processes can be found in an angular range  $> 50$  mrad and are usually detected via a HAADF detector in STEM. A big advantage of this type of image formation is the so called  $Z$ -contrast, as elements can be directly identified according to their brightness in the image [116].

### **Knock-on damage**

Due to the discussed developments in the field of electron microscopy (sec. 3.3) the image quality has drastically improved at low acceleration voltages down to 30 – 60 kV. These drastically reduce the sputtering of lattice atoms due to elastic scattering (called knock-on damage) and therefore increase the dose that can be used for imaging delicate samples [117].

### **Radiolysis**

Low accelerating voltages increase the ionizing effect of the electron beam on the specimen. This effect occurs especially in non-conducting specimens. The electron irradiation causes removal of shell electrons, leaving ionized atoms in the lattice. These ions in the lattice weaken interatomic chemical bonds. This leads subsequently to a loss of atoms. In non-conductive specimens a charge equilibrium is more difficult to restore than in conductors [118]. Irradiation with an electron beam can also induce other process within a material, such as crystallization of non-crystalline materials, which can be often observed *in situ* [119].

### **Chemical etching**

One obstacle for electron microscopy with atomically thin materials is the often dense surface coverage by hydrocarbons, which lead then to different unwanted effects [85, 7]. One rather obvious is that thick coverage (in nm range) of non-electron transparent material on top of the specimen results in a lack of visibility. As graphene and hBN contain only light atoms, this is a more serious problem for those than for MoS<sub>2</sub>, containing comparatively heavy atoms. Secondly it can cause severe damage on specimens due to chemical reactions between beam, adsorbates and the specimens' material, called chemical etching. According to recent research, chemical etching is mainly promoted in non-ultra high vacuum (UHV) conditions [120], as unfortunately present in most standard TEM instruments.

### **3.3.2 Transmission electron microscopy (TEM)**

In TEM, an electron beam is shone through a specimen. Therefore, the specimen has to be thin enough so that electrons can transmit through it. Usually TEM specimens need to be specially prepared or thinned from bulk materials so that these requirements are fulfilled. In case of atomically thin monolayers, such treatments are not necessary.

The electron beam in a TEM is produced in such a electron gun assembly described in section 3.3. In a conventional TEM construction the gun is located at the top of the microscope in contrast to a dedicated STEM instrument, as will be discussed in section 3.3.2. After the gun, a sophisticated arrangement of magnetic lenses, the goniometer (middle part) with the specimen entry and an observation system at the bottom follows.

TEM has two basic operating types: imaging and diffraction. Each needs different settings of the whole lens system. The lens system can in general be divided in three parts: the condenser, the objective and the projection system, that will be discussed below. Weakening or strengthening the condenser lenses C2 and/or C3 regulates the illumination of the specimen. The current of the coils in these lenses regulates the strength of the magnetic field. A strong coil current causes a strong magnetic field in the lens and therefore reduces its focal length. A weakening of the coil current and hence the magnetic field leads to an increase in the focal length.

#### **The condenser system and its apertures**

The condenser system is used to form the beam. After the gun and the accelerator, the electron beam is converged to the crossover at the C1 lens. The condenser system varies between two to four lenses (C1 - C3 and in some cases as well a minicondenser lens) depending on which parameters the beam has to fulfill. When all condenser lenses are activated, the semi-convergence angle can be regulated more precisely. Depending on the semi-convergence angle, the incoming beam can be chosen as spreading, parallel or converging beam.

The size of the illuminated area for a condensing beam can be adapted via the condenser apertures. The brightness is regulated by the excitation of the C1 lens (referred to as the spotsize). A weakly excited C1 lens gives a bright beam with a low demagnification of the source, whereas a highly excited C1 lens gives a beam with less brightness but high demagnification. A strengthened C2/C3 lens combination leads to a highly convergent beam, whereas a weakened C2/C3 lens combination leads to a more parallel beam.

The C1 aperture is the first aperture of the condenser system and located below the electron gun. This important aperture regulates the amount of non-paraxial rays contributing to the total beam. The choice of this aperture is always a trade-off. Usually the beam-limiting aperture is the C2 aperture, located after the C2 lens. A small C2 aperture cuts non-paraxial beams, which reduces spherical aberrations. Spherical aberration is an important lens aberration, as the focal points of paraxial rays differ from those of non-paraxial rays. This aberration is the main resolution limiting aberration for conventional TEM. Narrow beam-limiting apertures reduce drastically the electron dose at the sample, which is an advantage for beam sensitive samples, but it leads to lower brightness on the screen.

### **The objective system and its apertures**

In modern instruments the specimen is placed between the pole pieces<sup>1</sup> of the objective lens to guarantee a homogeneous magnetic field at the specimen. Some TEM devices come with a mixed condenser-objective system. In such a case the upper polepiece is a part of the condenser system. The position of the objective lens, including parts of the pre-specimen field is shown in figure 3.11 in parallel illumination. The specimen is placed into the pre-field of the lower objective lens. The post field of the objective lens focuses the scattered beams in the lenses' back focal plane (bfp), that is located approximately 1 mm below the specimen. Here the diffraction pattern is formed, as electrons from distinct scattering directions have a crossover. Diffraction pattern contains all angular

---

<sup>1</sup>The plus and minus poles of the magnetic lenses are called polepiece or -pieces

information of a specimen. A detailed description of how a diffraction pattern is created is given in section 3.3.2. Below the bfp, in the image plane, an image of the specimen is formed. Depending on which apertures are inserted, and the settings of the projector system (section 3.3.2), an image or a diffraction pattern can be seen at the screen.

As the post field of the objective lens is usually the strongest magnetic field in the column, the aberration contributions of this lens are as well the strongest. Aberrations and how to correct them will be discussed in detail in section 3.3.2.

As the area between the pole pieces contains the specimen it is in most conventional instruments a connection to the outer world. Conventional TEMs are often equipped with O-ring sealed goniometer side entries. Due to this design, the vacuum level of conventional devices is limited to pressures  $\geq 10^{-7}$  mbar. In the goniometer are mechanisms to rotate, tilt, heat, cool, and many more depending on the available specimen holders. All these mentioned activities can cause the sample to de-gas and cause undesired interaction with the electron beam in the strong field of the objective lens. To avoid such side effects a cooling trap is mounted around the specimen area to attract and trap undesired particles. This is to reduce chemical etching from the residual vacuum [120].

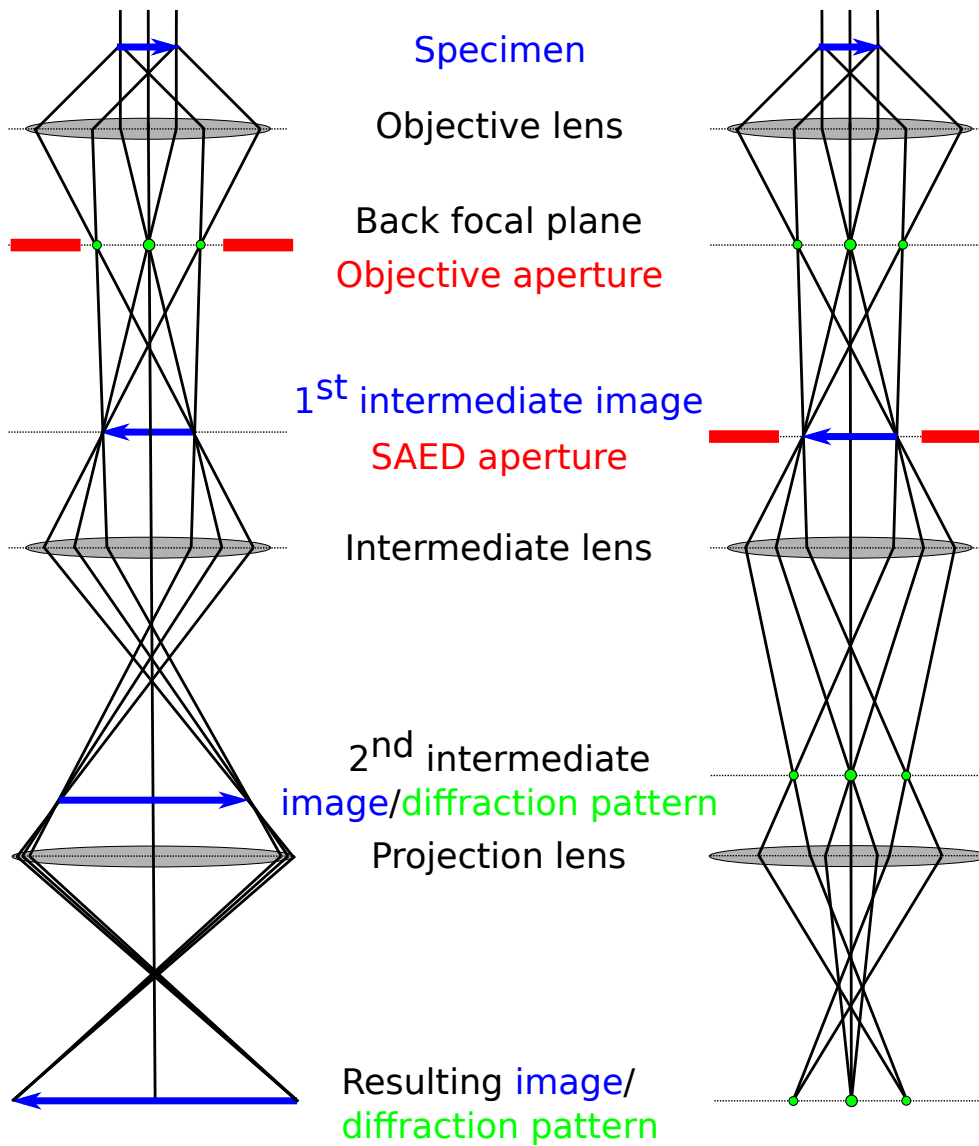


Figure 3.11: **Post-specimen ray diagram of TEM.** (left) Imaging and (right) diffraction mode share similar ray-paths until the first intermediate lens. In the imaging ray-path the position of the objective aperture in the bfp of the objective lens is shown. In the diffraction ray path the position of the SA aperture is shown. Based on reference [110].

Two imaging apertures are located between the sample and the projector system: the objective or contrast aperture and the SA aperture. The objective aperture is located in the bfp and the SA aperture in the image plane of the objective lens.

### **The projector system**

The image mode providing different magnifications and diffraction mode providing different camera lengths is controlled by the projector system. The projector starts with the (first) intermediate lens, shown in figure 3.11 and includes further lenses until the final image is formed. In many modern devices with additional lens systems (e.g. energy filter or image corrector) these lens systems are more complicated to guarantee high resolution images or diffraction patterns.

In simplified terms, it can be said that to create a diffraction pattern, the projector system must be weakened. The focal length increases until the front focal plane (ffp) of the (first) intermediate lens is the same plane as the bfp of the objective lens. Therefore, the projector system picks the diffraction pattern from the bfp of the objective lens. The magnification of the diffraction pattern on the viewing screen (or a camera) is controlled by the subsequent lenses and is referred to as camera length.

When the projector system is strengthened, its focal length decreases until the ffp of the (first) intermediate lens lies in the image plane of the objective lens. Therefore, an image of the specimen gets picked from the image plane and magnified as the user wishes. In many conventional TEM systems three magnification ranges are available. In the low magnification (LM) regime the objective lens is (almost) deactivated, therefore the magnification can be reduced until a factor of a few tens. In the selected area (SA) regime the objective lens is excited and ranges between a few thousand to several hundred thousand, whereas the high magnification (Mh) range starts at a magnification factor of about 800 000.

## The application of SA and objective aperture

Each position in the specimen creates scattered and unscattered electron beams. Scattered electrons undergo phase shifts, whereas unscattered do not. A beam formed by the latter is referred to as direct beam. In imaging mode the direct beam and the scattered beams are focused in one point, for each ray path. The sum of these ray paths form an image in the observation plane. These ray paths are shown in figure 3.11 (b) for two selected initial beams. If the sample is positioned at eucentric height, the resulting image contrast is generated by the intensity loss due to local differences in sample thickness, i.e. the amplitude contrast. A specimen in gaussian focus has minimum contrast. If the specimen is a thin object or a weak phase object, the observed intensity  $I(\mathbf{r})$  in the observation plane can be described as

$$I(\mathbf{r}) = |\psi(\mathbf{r})|^2, \quad (3.8)$$

where  $\psi(\mathbf{r})$  is the wave function of electrons in the image plane, described by

$$\psi(\mathbf{r}) = \psi_{exit}(\mathbf{r}) \star CTF(\mathbf{r}), \quad (3.9)$$

a convolution of the exit wave  $\psi_{exit}$  and the contrast-transfer function  $CTF(\mathbf{r})$  of the objective lens. Here the objective aperture comes into play. Located in bfp of the objective lens, it can cut rays in a certain diameter, reducing the images' information, hence increasing the contrast. In the bfp of the objective lens the diffraction pattern is formed by an electron wave function of the form

$$\psi_{bfp}(\mathbf{k}) = \mathcal{F}|\psi_{exit}(\mathbf{r})| = \psi_{exit}(\mathbf{k}). \quad (3.10)$$

The resulting diffraction pattern is the Fourier transformation  $\mathcal{F}$  of the, from the specimen exiting, wave function  $\psi_{exit}(\mathbf{r})$ , where the variable  $\mathbf{k}$  denotes the spatial frequencies and indicates that the diffraction pattern is in the reciprocal space. Therefore, the intensity distribution of the diffraction pattern can be

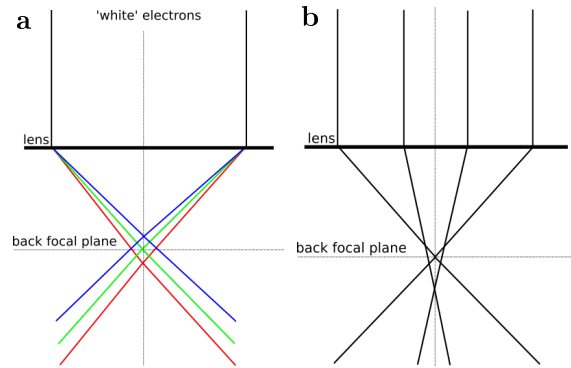


Figure 3.12: **Information - and resolution - limiting lens aberrations.** (a) Due to chromatic aberration electrons of different energies are focused at different focal lengths around the bfp of the lens. (b) Due to spherical aberration incoming off-axial electron are scattered more strongly compared to paraxial electrons.

described by

$$I(\mathbf{k}) = |\psi(\mathbf{k})|^2. \quad (3.11)$$

Inserting the objective aperture removes higher spatial frequencies, and hence works as a low pass filter. On the observation plane, in diffraction mode the objective aperture can be centered around the direct beam cutting out diffracted beams. Switching back to image mode, the image only contains information of the direct beam and no information of the angular beams. Such images are called bright field (BF) images in contrast to dark field (DF) images, which contain no information of the direct beam.

The SA aperture shown in figure 3.11, located in the image plane of the objective lens selects areas of given sizes from the specimen to form a diffraction pattern.

### Lens aberrations and how to correct them

Electron lenses are prone to aberrations. Unlike their glass counterparts for visible light, it is not possible to correct them via polishing or coatings. Instead one needs to influence the electron trajectories via additional electromagnetic multipole lenses.

The main resolution limiting aberration in conventional TEM and STEM is spherical aberration  $C_S$ . In case of  $C_S$ , abaxial rays have different focal lengths than paraxial rays. For  $C_S$ -corrected instruments the resolution limiting aberration is chromatic aberration  $C_C$ . It causes electrons of different wavelengths to be focused at different focal distances (see figure 3.12). The first potential source of an energy spread is at the gun and can be diminished by a spatially and temporally coherent gun, a monochromator or a combination of both. The second source of an energy spread is the specimen itself. Inelastic scattering causes an energy loss in the transmitted electrons. This leads to different focal lengths for different wavelengths and hence to smeared out areas instead of sharp beam crossovers. Some devices offer additional  $C_C$  correction.

$C_S$  corrected systems also correct for other lens aberrations described by the lens aberration function [121]

$$\xi(\alpha, \phi) = \frac{\lambda}{4}C_S\alpha^4 + \frac{Z}{2}\alpha^2 + \frac{A_2}{2}\alpha^2 \cos 2(\phi - \phi_2) + \frac{B}{2}\alpha^3 \cos 2(\phi - \phi_B) + \frac{A_3}{3}\alpha^3 \cos(3\phi - \phi_3) \dots \quad (3.12)$$

Here  $\alpha$  denotes the scattering angle,  $Z$  the defocus (the deviation of specimen height to the disk of least confusion),  $A_2$  and  $A_3$  the two-fold and three-fold astigmatism,  $B$  coma,  $\phi_2$ ,  $\phi_B$  and  $\phi_3$  the initial phases of the corresponding aberrations. Starting with coma the correction is an elaborate task. First of all, aberrations seldom come alone and they influence each other. High resolution devices have complicated and sophisticated arrangements of multipole lens systems and algorithms to deal with aberrations of higher orders.

### **The image corrector**

In addition to a monochromator the Titan 80-300 (S)TEM is equipped with an image corrector. The image corrector can be used after a primary alignment of the electrons in the TEM column to guarantee the best results. These primary or direct alignments contain: setting the eucentric height, correction of condenser and monochromator astigmatism and adjustments of the beam

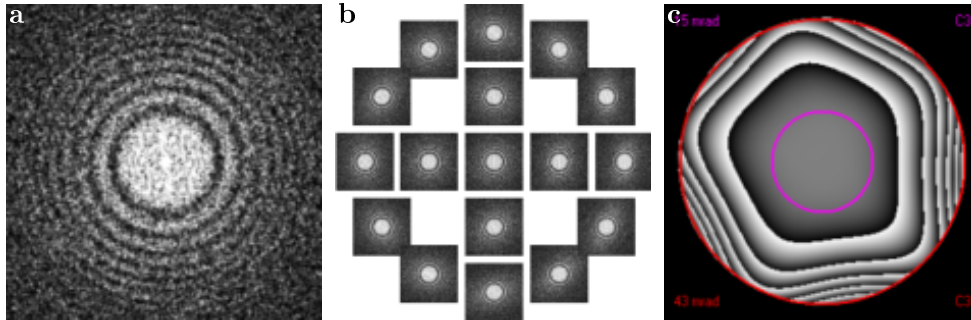


Figure 3.13: **Image correction via Zemlin tableau.** (a) Diffraction pattern showing CTF at  $-440$  nm defocus for  $80$  kV and (b) the corresponding Zemlin (tilt) tableau with a maximum beam tilt angle of  $18$  mrd. (c) The calculated phase diagram for the tableau in (a) shows the phase shift induced by the lens aberrations. For  $C_S = 0$  the phase diagram looks slightly different than in the current case for negative  $C_S$  imaging. Here  $C_S = -17 \mu\text{m}$ .

pivot points and the voltage center. The image corrector algorithm uses a diffraction pattern of an image of a thin and amorphous specimen region taken at a certain magnification. Depending on the defocus the 2D contrast transfer function (CTF) exhibits different zero crossings. Depending on the present aberrations the form of the 2D CTF diverges from an ideal circular symmetry as shown in figure 3.13 (a). Diffraction patterns at different beam tilts are taken to obtain the Zemlin tableau (figure 3.13 (b)). The quality of estimating the aberrations depends on the number of diffraction patterns at different beam tilts and the image quality of the diffraction patterns. The tilt angle determines which order of aberrations can be taken into account. For  $80$  kV acceleration voltage, Zemlin tableaux with up to  $15$  mrad beam tilt only take second order aberrations into account whereas for  $18$  mrad or higher beam tilt also third order aberrations can be corrected.

### Cameras and detectors

TEMs are usually equipped with different screens, detectors and spectrometers. The most common one, and historically the oldest, is the fluorescence screen. It is an electron reactive material emitting visible light as soon as elec-

trons hit the fluorescent coating. A standard equipment in older devices was a camera with an image plate, which is today replaced by a CCD camera. With newer generations of TEMs there comes a selection of different BF and DF detectors. BF detectors are located in the path of the direct beam. DF detectors are located in a ring around the BF area, collecting only electrons scattered in certain angles. Due to their ring shape, they are referred to as ADF detectors ("A" for annular). As the electrons are scattered by the nuclei at very high angles they lose coherency. These scattering processes are described as Rutherford scattering and can be differentiated from Bragg processes where electrons are described by their wave properties. DF detectors are mostly used for STEM image acquisition.

### **EELS and EFTEM**

Electron energy loss spectroscopy (EELS) was developed in the 1940's by James Hillier and R.F. Baker [122], but gained more importance in the 1990s with advances in microscopy and vacuum technologies. The centerpiece of an EELS spectrometer is the energy filter. Due to inelastic scattering events, some electrons lose small fractions of their initial energy. The energy losses depend on which inelastic processes take place. These inelastic scattering events are caused by phonon and plasmon excitations, inner shell ionizations, inter- and intra-band transitions and Cherenkov radiation. As energy loss by inner shell ionizations (core loss) are material-dependent, these losses help identifying the elemental composition of a specimen. In a post-specimen energy filter the exiting electrons are sorted by their energies in the lens system of the energy filter. Especially in thin samples, the majority of electrons is elastically scattered and the most prominent peak is the zero loss peak (ZLP) at 0 eV energy loss. It is followed by the low loss region ( $< 100$  eV) dominated by the plasmon peak. The height of the latter scales with increasing specimen thickness. After that the high loss regions ( $> 100$  eV) can be found. These regions represent the core losses and are mainly used for elemental identification.

Another application of the energy filter is energy filtered imaging or diffrac-

tion. Within the filter, energy selection slits are used to select certain areas of the spectrum for imaging or diffraction. For zero-loss filtered images or diffraction patterns, the energy selection slit is placed such that only elastically scattered electrons can enter the energy filter. This yields a higher signal to noise ratio. For diffraction inelastic scattering events with rather low loss lead to spreading of the diffraction spots. The energy selection slit can be placed over any area of the spectrum to get image or diffraction information of plasmon oscillations, or at elemental energy edges.

### **Specimen holders**

The versatility of TEM can be enhanced with special sample holders. Starting from the simple single tilt holder, they consist of a part protruding from the side entry, the O-ring seal and the area where the specimen is clamped on. In the experiments in this thesis a single tilt, a straining holder and heating holder were used. To apply mechanical strain onto a TEM sample (as discussed in section 4.5), the straining holder allows a stepwise increase of external strain. It has a stepper motor drive with an accuracy of  $0.05 \mu\text{m}$ . The specimen is fixed by two hooks, one of which is attached to the external motor drive. During other experiments, heating of the sample is necessary (as for example in section 4.6). This can be done with a heating holder. Through wire connection to an external controlling module, the temperatures can be controlled up to  $1400^\circ\text{C}$ . Starting from  $450^\circ\text{C}$ , additional water cooling is necessary.

### **Instruments used in this work**

The TEM devices used in this work are a Phillips CM200 from 1997 and a Titan 80-300 (S)TEM with  $C_S$  corrector from 2006. Both microscopes have been aligned for 200 and 80 kV. The CM200 is equipped with a  $\text{LaB}_6$  crystal whereas the Titan has a standard Schottky FEG (sFEG) with higher brilliance and smaller energy spread. The  $\text{LaB}_6$  crystal is referred to as a thermionic source with the energy spread of 1 eV [110], whereas in an sFEG the electron

beam is produced via field emission.

### **Electron diffraction**

In section 3.3.2, the principle settings of the diffraction mode were introduced. The diffraction pattern itself is generated in the back focal plane of the objective lens, which is usually the strongest electromagnetic lens in the microscope. The bfp of the objective lens is typically 1 mm below the sample. Therefore all observed diffraction effects are far field effects. Near field effects happen within a distance within one wavelength and the transition zone from near to far field is as well about a wavelength. All transmitted electrons diffracted by the same angle are focused in the back focal plane of the objective lens in one specific point. Depending on which effects should be achieved in a diffraction pattern, the illumination of the specimen area is important. As diffraction pattern can in good approximation be seen as Bragg reflexes of lattice planes, coherency of the incoming electrons is necessary. To get sharp and distinct diffraction spots, parallel beam illumination is crucial. Parallel beam condition can be achieved by weakening the C2 lens in two condenser mode or by setting the semi-convergence angle to zero in three condenser mode.

The incoming electrons can be described as a plane wave

$$\Psi_{in}(\mathbf{r}) = A_0 \exp[i\mathbf{r}\varphi_0], \quad (3.13)$$

where  $A_0$  is the amplitude and  $\varphi_0$  the initial phase of the direct beam. After sample interaction, scattered and un-scattered (or direct) beams can be distinguished. Therefore, the from the specimen exiting wave function is of the form

$$\Psi_{exit}(\mathbf{r}) = A_n \exp[i(\varphi_0 + \varphi_n)]. \quad (3.14)$$

The amplitude  $A_n$  describe the amplitude changes due to interaction of each partial wave with the periodic potential of the specimen and  $\varphi_n$  the phase change of each scattered partial wave. In the bfp of the objective lens, the par-

tial beams belonging to certain Bragg reflexes are brought to focus at distinct points. Each reflex originating from periodical and oriented structures, the lattice planes, has a distinct position in the pattern. The diffraction pattern therefore contains all information about all orientations of lattices within the illuminated area of the specimen. This process can be described by a Fourier transformation of the exiting wave as  $\Psi_{exit}(\mathbf{r})$

$$\Psi_{bfp}(\mathbf{k}) = \mathcal{F}|\Psi_{exit}(\mathbf{r})| = \Psi_{exit}(\mathbf{k}). \quad (3.15)$$

$\Psi_{exit}(\mathbf{k})$  is the representation of  $\Psi_{exit}(\mathbf{r})$  in reciprocal space. The intensity distribution  $I_d(q)$  in the reciprocal space, the diffraction pattern, is therefore of the form

$$I_{diff}(\mathbf{k}) = |\Psi_{exit}(\mathbf{k})|^2. \quad (3.16)$$

The diffraction pattern, unlike the image in the image plane further below (as described previously) contains all the phase information of the specimen.

However, the diffraction pattern does not contain all possible reciprocal lattice points. The allowed reflexes are specified by the Ewald construction. The electron beam, in Fourier space described by the vector  $\mathbf{k}$ , can be described by a plane wave. The Ewald construction defines the wave front at a certain distance from the source, determined by the electron energy. The wave front has a circular shape. For a bulk crystal the allowed reflexes are those where the Ewald sphere hits reciprocal lattice points. In figure 3.14 an allowed reflex is indicated by the vector  $\mathbf{k}_0$ . Unlike in this simplified sketch, in reality the reciprocal lattice points are not discrete points, but, depending on the real space lattice take various shapes. This is explained in more detail for 2D materials in section 3.4.

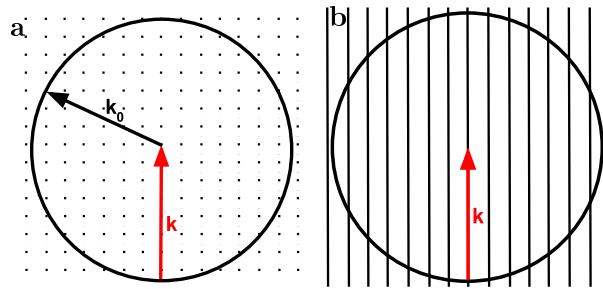


Figure 3.14: **Ewald sphere.** (a) Of a bulk material. The spots represent the reciprocal lattice points,  $\mathbf{k}_0$  the incoming and  $\mathbf{k}$  the scattered electron beam, in reciprocal space. The radius of the sphere is determined by the electron wavelength. (b) Ewald sphere cutting through relrods of a 2D material.

There are several techniques for acquiring a diffraction pattern, the most common of which is the SA diffraction. Here, only electrons diffracted from a specific area create the diffraction pattern. There are usually different sizes of SA available. With smaller aperture sizes, smaller areas can be investigated, with the drawback of increasing edge effects. This is because electrons hitting the edges of the aperture experience additional scattering event, leading to a blurring of diffraction spots. Additionally, in selected area electron diffraction (SAED) electrons scattered from areas outside the selected area can partake in forming the diffraction patterns. To avoid these effects, aperture-free parallel electron diffraction is possible if the device is equipped with an additional C3 lens. In such microprobe settings the size of the actually illuminated parallel area can be determined by condenser apertures, magnification and excitation of the combined C2 and C3 lenses. A further advantage of aperture-free electron diffraction is that the area of diffraction is limited by the beam itself.

### Dark-field imaging

DF images contain information from certain scattering directions, excluding the information of the direct beam. DF images can be seen as the negative to BF images, as illustrated by figure 3.15 (a) and (b). The inset in figure 3.15 (c) shows a SA diffraction pattern of the area marked in (a) and (b).

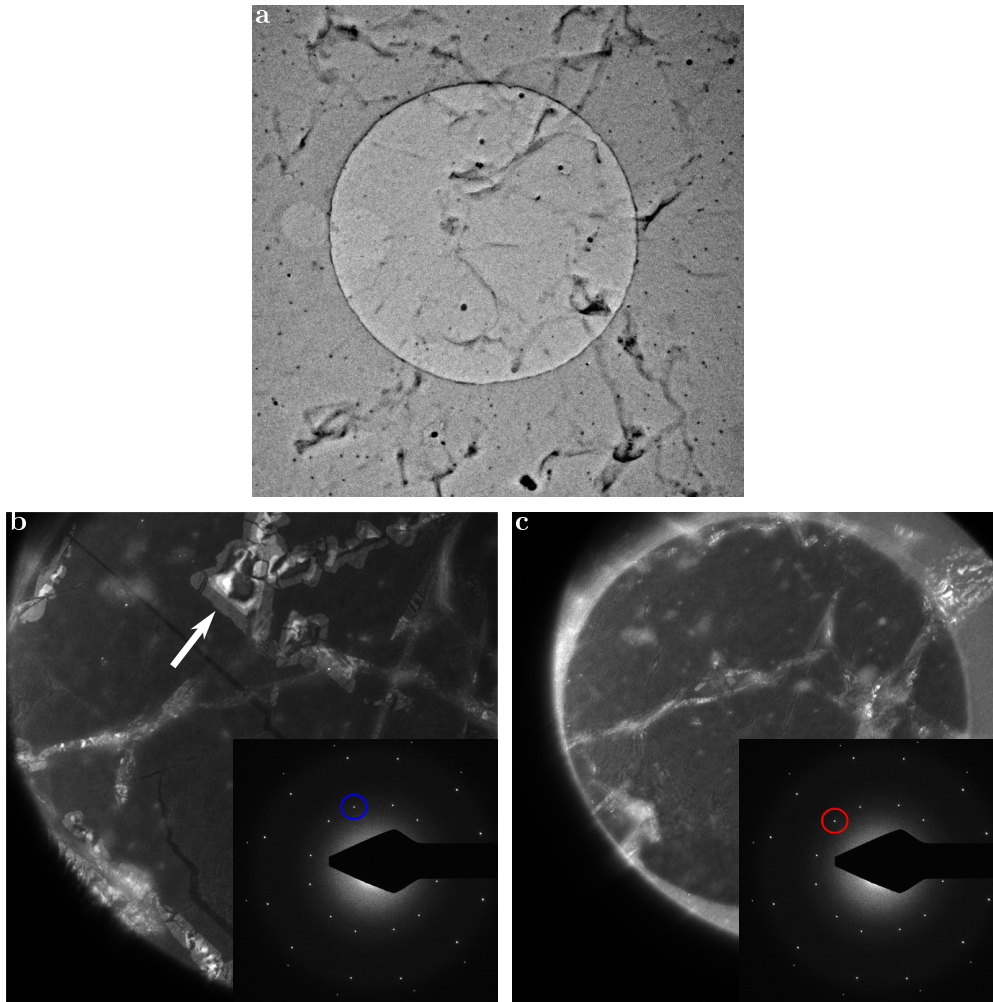


Figure 3.15: **BF and DF.** (a) A BF image of a graphene-hBN vdW heterostructure. The gray features are pockets of trapped contamination. (b) DF image of the hBN layer. The blue circled diffraction spot of the diffraction pattern (inset) was chosen to produce the DF image. This layer shows a typical feature in hBN membranes, a triangular, pyramidal section of hBN multilayers (arrow). The layer also shows cracks, which might originate from the transfer process. (c) DF image of the graphene membrane. The inset shows the corresponding diffraction pattern with the specific diffraction spot highlighted (red circle). The membrane is intact, but shows thickness contrast due to trapped contamination.

The objective aperture can be used to select the direct beam to enhance the contrast of a BF image. If this aperture is placed over a selected diffraction spot and the projector settings are changed to image mode, a DF image can be seen, where all areas with the selected orientation are bright. This is shown in figure 3.15 (c). TEM-DF imaging is therefore a useful tool to investigate polycrystalline or layered samples.

There exist two ways to obtain a DF image from a certain diffraction spot. However, they do not give equal results. In a properly aligned TEM, the gun, the beam and the apertures are aligned within the optical axis. The first method is shifting the objective aperture away from the direct beam, on top of the diffracted beam. This however would cause a deviation from the optical axis and hence reduce the quality of the already weak DF image. This can be avoided by the second method, via tilting the electron beam with deflector coils. These coils tilt the beam such that the diffracted beam replaces the direct beam in the center of the optical axis. This procedure helps to increase the quality of DF images.

As shown by Ping *et al.* [123], DF imaging is, apart from diffraction pattern, a tool to distinguish between layer thicknesses in vdW heterostructures. Diffraction spots vary in intensity depending on the number of layers. Selecting a certain diffraction spot results in a DF image of corresponding brightness contrast, of which the number of layers can be estimated [123]. In case of a polycrystalline specimen, crystal orientations can be assigned to positions on the specimen. Even though DF imaging can give insights into the specimen properties, there are some obvious drawbacks. The main is the massive reduction in electron intensity hitting the screen or detector. Also the adjustment can be tedious and is rather error-prone.

### **Scanning TEM (STEM)**

With recent developments of aberration correcting technologies in a synergy with the field emission gun, scanning transmission electron microscopy (STEM) has recently gained popularity. In contrast to TEM, in STEM an electron probe

is formed by the magnetic lenses of the condenser and objective system. The probe is then scanned by scanning coils over the desired field of view (FOV). To achieve the best results, dedicated STEM devices (dedicated scanning transmission electron microscope (DSTEM)) have a rather different setup than a conventional TEM. These instruments tend to have the gun at the bottom to improve mechanical stability. They also lack a projector system and contain instead post-specimen lenses to reduce the length of the column. Working with a DSTEM, one usually uses a DF detector with a specific angular range (MAADF for medium angles and HAADF for high angles). In case of atomic resolution it is, in contrast to a TEM, possible to distinguish between different elements directly due to the scattering contrast. Lighter atoms appear darker, whereas heavier atoms appear brighter due to Rutherford scattering, as mentioned in section 3.3.2. In the angular range of a MAADF (10–50 mrad), Bragg scattering contributes to the image formation, whereas in the HAADF regime ( $\geq 50$  mrad) the contribution is purely (screened) Rutherford scattering. For light atoms, such as in carbon structures or hBN, the preferred detector is a MAADF due to the better signal. For materials containing heavier elements, such as MoS<sub>2</sub>, HAADF is a better choice.

### **Probe correction**

To form a proper Ångström-sized probe, lens aberrations need to be minimized. Similar to TEM, the resolution limiting aberration is  $C_s$ . The probe can suffer also from all the other aberrations similar to an image in TEM. A tool for aberration correction in STEM is the Ronchigram. It is named after Vasco Ronchi, who invented the test in 1923 [124]. Its original purpose was to qualify and subsequently ratify surface qualities in optics, especially for astronomical use, and actually bases on the Foucault knife-edge test. It has been adapted for aberration-corrected STEM devices, such as the Nion UltraSTEM 100 [125].

The Ronchigram is a defocused image of the electron beam, close to the specimen surface, recorded by a CCD device. In the gaussian focus, the image on the CCD is, in the ideal case, a magnified image of an infinitely small spot

(the electron probe). In this case, for an ideal probe, the Ronchigram should show a homogeneous gray image. The Ronchigram is limited by an aperture (virtual objective aperture (VOA)), that limits the influences of aberrations of off-axial regions, as they would reduce the spatial coherence. To correct aberrations via ronchigrams, an amorphous area on the specimen is set to underfocus via the stage drives. Here the original idea of the ronchi-test can be seen. The CCD camera takes five images, each at a different close-by positions (at  $(0,0)$ ,  $(x,0)$ ,  $(-x,0)$ ,  $(0,y)$  and  $(0,-y)$ ). The algorithm compares changes in the features in the image to those at the position  $(0,0)$ . In the non-aberrated case, the features would be simply shifted, whereas in the aberrated case they are also distorted. The algorithm calculates the aberration function, from which the necessary changes can be estimated, and the corrector correspondingly adjusted. This is an iterative process that should converge within a few iterations of measuring the ronchigrams and subsequently changing the aberration corrector.

The Nion UltraSTEM 100 in Vienna is equipped with four detectors: a CCD camera in direct beam direction, a HAADF and a MAADF detector and an EELS camera. EELS offers the possibility to identify the atomic composition of small areas down to individual atoms [114]. It can also provide information regarding chemical bonding and electronic structure [126]. Comparing TEM with STEM, the latter offers the advantage that multiple spectroscopy signals and images can be acquired simultaneously. This allows the direct correlation between the image and the spectroscopic information for every location within the FOV [126, 117, 127, 128, 129, 130].

There are several advantages with using an an aberration-corrected STEM. One is a much simpler image interpretation as compared to TEM. Due to the scanning mode the actual irradiation time with the electron beam can be drastically reduced. Even beam sensitive materials such as hBN and MoS<sub>2</sub> can be imaged at atomic resolution. Another advantage of the small probe is targeted manipulation of specimen areas. With the help of the scanning coils, the probe can be parked on a desired sample position, so that a small area is

exposed to a high electron dose for a specified period of time. Such experiments can create and image dynamical structural changes within the specimen.

### **3.4 2D materials in the electron microscope**

In early days, the only way to increase resolution in HRTEM was to increase acceleration voltage to decrease the wavelength of the electrons. But for investigating delicate structures, such as 2D materials, high electron energies lead to fast destruction of the specimen. However, developments in image correcting techniques have recently made HRTEM imaging at low acceleration voltages possible. Unfortunately at lower the accelerating voltages radiation damage due to inelastic scattering becomes an issue for non-conductive specimen.

Knock-on damage is caused by the collision of the beam electrons with the nucleus of the target atom [131]. This type of elastic beam damage is most significant at high electron energies. Ionization damage or radiolysis happens when the incoming electrons remove electrons from the sample. In case of non-conducting materials, such as hBN or MoS<sub>2</sub> this is a cause of significant damage. For graphene neither radiolysis nor charging are relevant due to its high conductivity. Chemical etching leads to damage in an indirect way. Etching processes can be observed under non-UHV conditions. In such conditions the incoming electrons produce free radicals by hitting residual molecules in the microscope vacuum [120]. These can cause etching of the material. The effect of chemical etching is less pronounced for chemically inert materials, such as hBN.

#### **Weak phase object approximation**

Especially in atomic monolayers, unlike in a bulk material, the incoming electrons only experience a maximum of one scattering event. In samples built of several atomic layers, the incoming beam is scattered and the scattered beams are re-scattered themselves. For weak phase object the interaction between diffracted beams is negligible.

## 2D materials in reciprocal space

The reciprocal space is a powerful tool to tease out structural properties of materials. Electron scattering processes are mathematically described by a Fourier transformation from the real space into reciprocal space. Assuming the lattice in real space is described by 2D Bravais lattice, every point in the lattice can be addressed by a vector

$$\mathbf{R}_n = n_1 \mathbf{a}_1 + n_2 \mathbf{a}_2 + n_3 \mathbf{a}_3, \quad \text{where } n_1, n_2, n_3 \in \mathbb{Z} \quad \text{and} \quad \mathbf{a}_3 = 0, \quad (3.17)$$

with  $\mathbf{a}_1$ ,  $\mathbf{a}_2$  being the lattice vectors. The reciprocal lattice vectors  $\mathbf{b}_1$ ,  $\mathbf{b}_2$ ,  $\mathbf{b}_3$  are then determined by

$$\mathbf{b}_1 = \frac{\mathbf{a}_2 \times \mathbf{a}_3}{\mathbf{a}_1 \cdot (\mathbf{a}_2 \times \mathbf{a}_3)}, \quad (3.18)$$

$$\mathbf{b}_2 = \frac{\mathbf{a}_3 \times \mathbf{a}_1}{\mathbf{a}_2 \cdot (\mathbf{a}_3 \times \mathbf{a}_1)} \quad \text{and} \quad (3.19)$$

$$\mathbf{b}_3 = \frac{\mathbf{a}_1 \times \mathbf{a}_2}{\mathbf{a}_3 \cdot (\mathbf{a}_1 \times \mathbf{a}_2)} = \infty \cdot \hat{\mathbf{a}}_3. \quad (3.20)$$

The representation of a 2D material in reciprocal space is therefore given by the relation

$$\mathbf{G}_m = m_1 \mathbf{b}_1 + m_2 \mathbf{b}_2 + m_3 \cdot \infty \cdot \hat{\mathbf{b}}_3, \quad \text{where } m_1, m_2 \in \mathbb{Z}. \quad (3.21)$$

The length scales in reciprocal space are given in reciprocal units,  $[\text{length}]^{-1}$ . As the extent into the third dimension in real space  $\mathbf{a}_3 = 0$ , the reciprocal representation of a 2D material exhibits an infinite extension in the out-of-plane direction in reciprocal space, called relrods. Figure 3.16 (a) shows a sketch of relrods for a 2D material. As a real 2D material has a finite thickness, the relrods are in reality not infinitely long. The size scales with the specimen thickness, as shown schematically in figure 3.16 (b). The thicker the specimen, the shorter the relrods. As they are always in direction of the plane-normal, their orientation with respect to the orientation of the incident electron beam contains information about the out of plane shape of the studied material. The

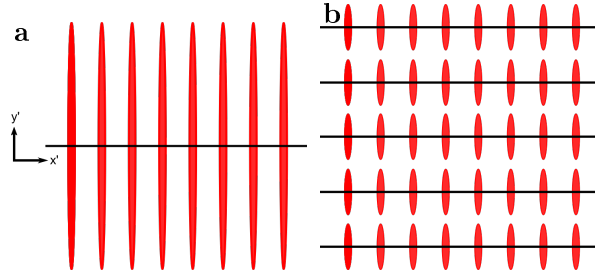


Figure 3.16: **Relrod representation of thin materials.** (a) Relrods of an atomically thin material extend far in the orthogonal direction of the 2D membrane; (b) for thicker samples the extent of the relrods in direction orthogonal to the membranes' extent decrease with increasing number of layers. Both sketches do not represent true interatomic distances.

analysis of the relrod orientation will play a major role in the sections 4.4.1 and 4.5 about investigating corrugations in 2D materials.

### Diffraction pattern of 2D materials

Electrons are scattered at the periodically arranged electrostatic potential of the unit cell. The energy distribution, describing the Coulomb potential of the scatterers have a maximum at the atomic positions. The spots seen in a diffraction pattern can be described by elastic diffraction fulfilling the Bragg condition

$$\mathbf{G} = \Delta\mathbf{k}, \quad \Delta\mathbf{k} = \mathbf{k} - \mathbf{k}'. \quad (3.22)$$

Here  $\mathbf{G}$  denotes all possible scattering vectors defined by a vector of incidence  $\mathbf{k}$  and a scattered vector  $\mathbf{k}'$ . The two vectors  $\mathbf{k}$  and  $\mathbf{k}'$  are related by the scattering angle  $\theta$ . The length of the scattering vector  $\mathbf{G}$  is

$$|\mathbf{G}| = |\mathbf{k}|\theta \quad \text{for small angles } \theta. \quad (3.23)$$

As scattering angles in TEM are usually in the range of some milliradians, a small angle approximation is valid. The allowed spots described by all vectors  $\mathbf{G}$  are defined by all allowed Bragg scattering events in the 2D lattice. To illustrate the origin of the diffraction spots, an arbitrary hexagonal lattice is

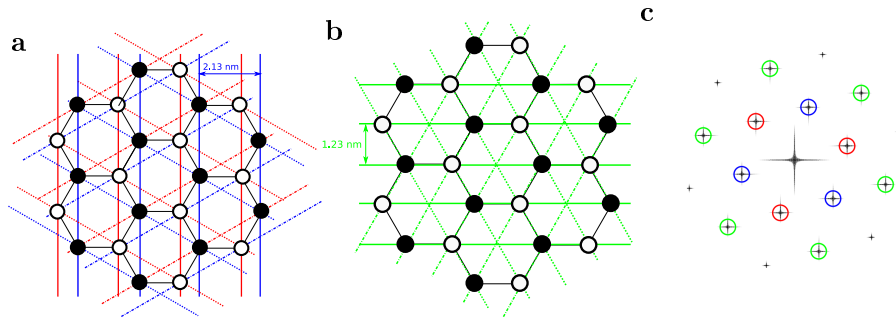


Figure 3.17: **Lattice planes and corresponding diffraction spots.** (a) First order diffraction spots correspond to blue and red indicated lattice planes, in zig-zag direction, in different orientations. Lattice planes with the same line structure generate one diffraction spot. Atoms sitting on different sublattices are drawn by filled and unfilled dots. (b) Second order diffraction spots correspond to green indicated lattice planes, in armchair direction, in different orientations. Lattice planes with the same line structure generate one diffraction spot. (c) Simulated diffraction pattern of graphene with marked diffraction spots.

shown in figure 3.17 (a). The lattice shows a two atomic base, one atom indicated by a smooth edge the other by a dotted edge.

The lattice planes in zig-zag (a) and armchair (b) direction and according diffraction spots (c) are shown in figure 3.17. First order diffraction spots of a hexagonal, 2D lattice are produced by Bragg reflexes originating from lattice planes in zig-zag direction, with a distance of 2.13 nm (in graphene). This is indicated by the blue and red marked lattice planes in figure 3.17 (a). The red and the blue marked lattice planes go through atoms of one of the two basis atoms of the sublattices. All lattice planes in armchair direction, with distance of 1.32 nm, go through both basis atoms. In the case of graphene the basis atoms are two identical carbon atoms. In the case of hBN, and up to a certain degree for MoS<sub>2</sub> these are different atoms with different scattering properties which results in different intensities in the diffraction pattern. A quantitative study of the influence of different elements to the intensity of single diffraction spot is presented in section 4.3.

In case of stackings of several layers of 2D materials, the number of layers can also be determined from the intensity distributions of certain diffraction

spots. For graphene, mono- and multilayers can be distinguished by using the intensity ratio of the (100) to the (110) diffraction spots. Similar intensity relations can also be found also for other 2D materials [35].

### **Contamination**

A reoccurring obstacle while investigating 2D materials using transmission techniques is contamination. In its different variations it is a well known topic in microscopy. Most of it is caused by sample preparation, especially if polymers are used for easier transfers between carrier materials. Another source is storage in non-UHV environments. Defects in the lattice further facilitate the accumulation of contamination. As the local binding energies differ from the pristine areas, grain boundaries and defective areas in general often attract hydro-carbon contamination. Contamination hinders high resolution imaging in a TEM, as the underlying lattice cannot be resolved. As most of the contamination contains carbon, this is especially an issue with 2D materials of light element, such as graphene or hBN. Contamination also causes problems for electron diffraction. As contamination can reach thicknesses of several atomic layers, the probability of inelastic scattering events increases. The energy spread of electrons additionally scattered at contamination is higher. This leads to a continuous background in the diffraction patterns and decreases the signal-to-noise ratio. To avoid this, a post-specimen energy filter can be used to get a higher signal to noise ratio for the diffraction spots.

### **Making corrugations visible**

TEM offers the possibility of contactless investigation of the out-of-plane corrugations of the observed 2D membrane. However, quantitative measurements of intrinsic corrugations in the image mode of a TEM are not exact and would be tedious to carry out. In case of a perfectly aligned specimen, a shift in the x-y-axis leads to changes in focus due to corrugations. A measurement of the height change of the focus could thus give the change in the amplitude

of the present corrugation. Unfortunately the exact and un-tilted alignment of a specimen would cause high uncertainties. Furthermore, as ripples induce local tilts, they are visible in HRTEM as lattice compressions. For the smaller corrugations with a smaller magnitude, this method is not applicable [98, 96].

In the section introducing the diffraction mode (section 3.3.2) and 2D materials in TEM (section 3.4), the representation of 2D materials in reciprocal space were shown to be poles (or relrods) in direction of the surfaces' normal (figure 3.18 (a)). The Ewald sphere formed by the incoming electrons intersects the array relrods. At typical accelerating voltages, the sphere can be assumed to be a flat plane. The diffraction pattern shows a superposition of all present surface normals as shown in figure 3.18 (b). This superposition forms cones in reciprocal space. If the specimen is tilted, a different cross section between the Ewald sphere and the superimposed relrods can be observed in the viewing plane. The diffraction patterns taken from untilted specimen ( $0^\circ$  tilt) are identical for non-corrugated and corrugated specimens. If the specimen is in eucentric height, the Ewald sphere intersects the relrods at their crossover (figure 3.18 (b)).

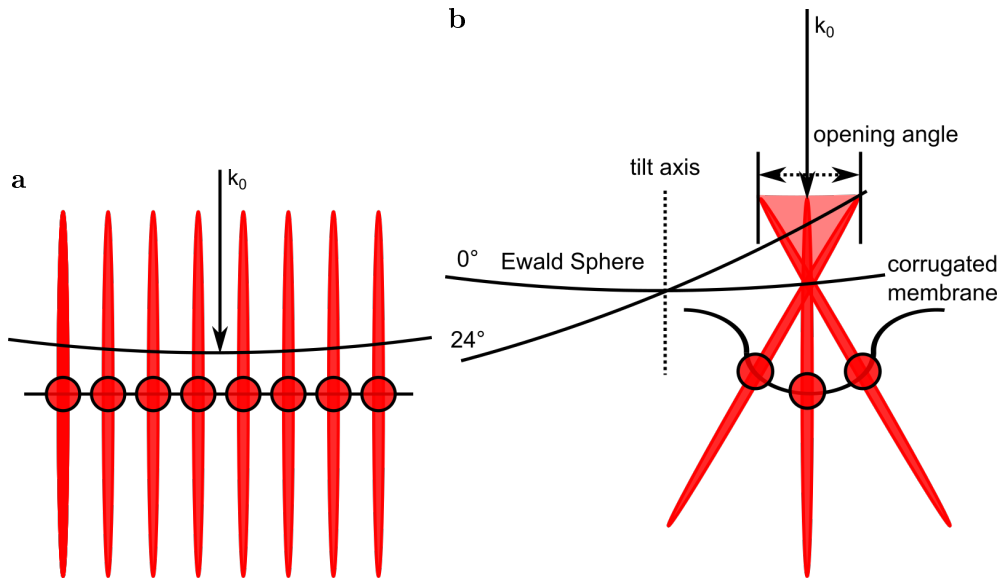


Figure 3.18: **Relrods and Ewald sphere** (a) The representation of a flat 2D material in reciprocal space are relrods orthogonal to the specimen surface. The Ewald sphere at an accelerating voltage of 80 kV or higher can be assumed to be almost a plane surface. (b) The relrods of a corrugated 2D material are orthogonal to the local curvature. For simplicity only three superposing relrods are drawn.

For non-corrugated specimens and at  $0^\circ$  tilt, the diffraction pattern exhibits sharp, distinct diffraction spots, with equal distance to the center. Increasing the specimen tilt shows still sharp spots, but as the Ewald sphere hits the poles at different heights, the diffraction spots outside the tilting axis move in direction orthogonal to the tilting axis. The diffraction pattern for each set of Bragg reflexes becomes elliptical.

For corrugated specimens at  $0^\circ$  tilt the Ewald sphere cuts similarly through the cross-over points of the cones in reciprocal space. Increasing the specimen tilt for those specimens, the Ewald sphere cuts through the cones at different angles. As in the non-corrugated case, the diffraction spots start to form an elliptical diffraction pattern with increasing specimen tilt. Above all this the diffraction spots themselves change shape: they broaden with increasing tilt angle. The spots furthest away from the tilt axis experience the strongest broadening.



## Chapter 4

# Results

### 4.1 Substitutional Si impurities in monolayer hexagonal boron nitride

The presented results were published in and referred to in the list of publications in section 1.

Imaging monolayered hBN in an electron microscope triggers, apart from knock-on processes, ionization damage due to its electronic characteristics. For continuous irradiation with energetic electrons, initial defects tend to grow into triangular shaped pores [55]. During STEM investigation of the sample non-radiation related Si impurities were observed. Therefore, it can be concluded that these impurity atoms were created during the CVD growth [128] as described in section 3.2. Such findings are rather common in CVD grown graphene and can be explained by the fact that during most preparation processes, Si containing materials are involved, for example glass tubes in typical CVD furnaces.

#### **STEM imaging**

The STEM images presented in this section were taken in a Nion Ultra-STEM 100 with a MAADF detector. As the observed material is only one

atom thick, and the scattering still dominated by Rutherford scattering, the image contrast of the detector can be interpreted similarly as that gained via an HAADF detector. Therefore, atoms with a higher brightness can be related to atoms with higher atomic number. This allows the detection of Si atoms in the lattice and the subsequent statistical analysis. Also the exact lattice site can be directly determined. The energetically favored silicon substitution is on a boron vacancy [132].

In this study the analyzed area was  $2405 \text{ nm}^2$  and 67 silicon atoms could be identified. Examples from the analyzed images are shown in figure 4.1 with different FOVs. For the analysis only contamination-free areas were taken into account. At first an overview area, without lattice resolution was taken. Then the FOV was reduced until the hBN lattice became visible. As seen in figure 4.1 (a) a FOV of 32 nm is sufficient for counting silicon atoms. However, at this scale it is not possible to evaluate at which lattice site the impurity is located. Here a FOV of 16 or 8 nm is needed. Such small FOVs have the drawback that often adjustment of the focus were necessary, exposing the lattice to additional electron irradiation. Taking images of beam sensitive areas is a trade-off between resolution and influencing the lattice. As visible in figure 4.1 (f) pore creation already started after short exposures. Images with a smaller FOV were always taken after those with larger FOV.

Figure 4.1 (g) - (j) show the quantitative analysis of silicon impurities in hBN, where (i) shows a line profile of a close-up of the region of interest in (h) and is marked by arrows. Figure 4.1 (h) shows a simulated MAADF image of a silicon impurity in a boron site with a similar FOV, which is in good agreement with (b). According to Krivanek *et al.* the intensity between Si and B atoms imaged with a ADF detector is about  $(14/5)^{1.64} = 5.41$  [60]. The experimental data gives a ratio of 5.25, which is close to the predicted value. The Si atoms found in the lattice are not stable enough to allow EELS measurements that would provide further evidence of the identity of the impurity atoms. During continuous electron radiation the impurity switched lattice positions or disappeared.

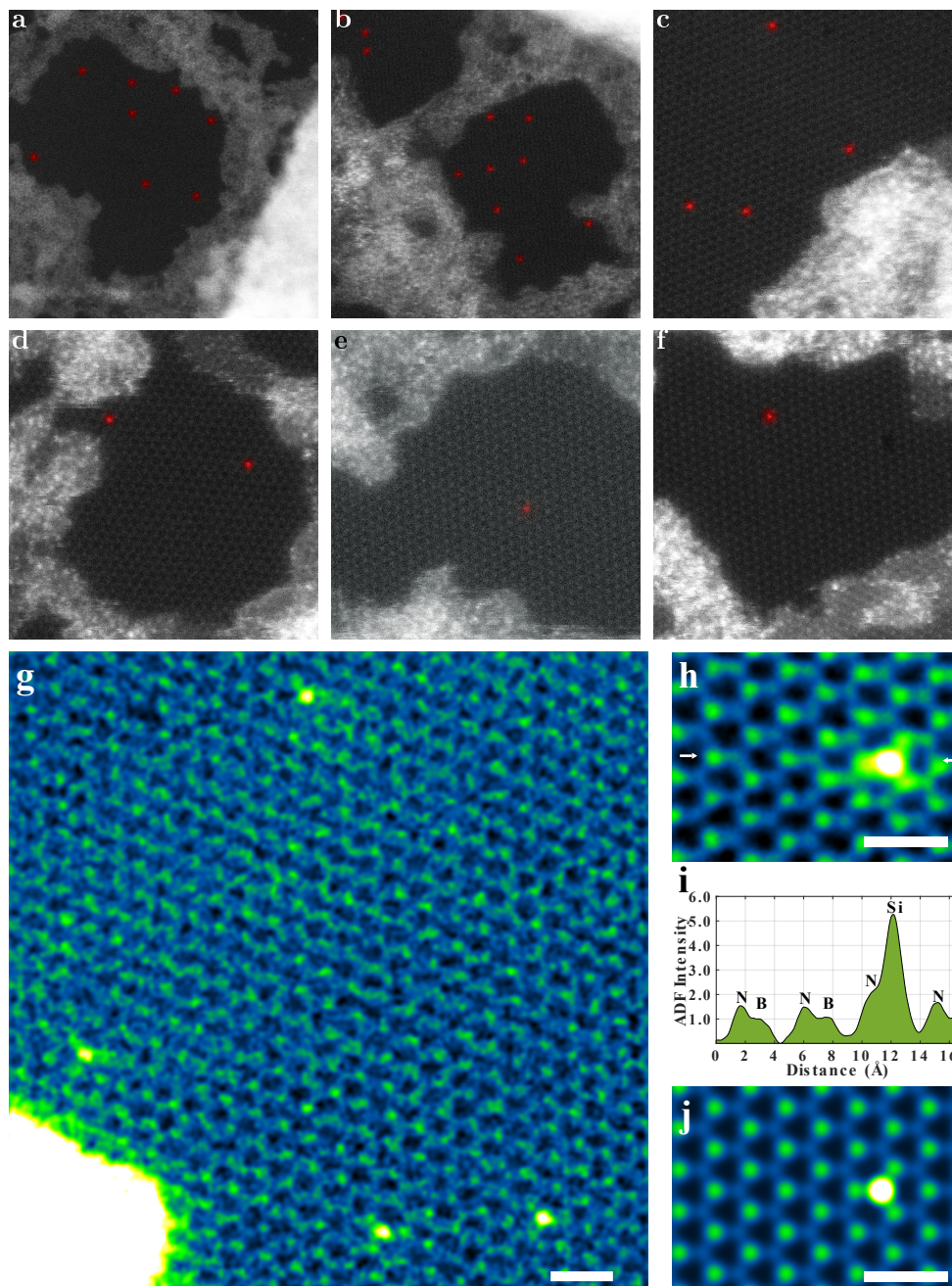


Figure 4.1: **STEM MAADF images of Si atoms in hBN.** (a) - (f) Experimental MAADF images of impurity sites. The red marked atoms indicate Si atoms. (g) Experimental MAADF image with multiple Si impurities and (h) a close-up. The arrows indicate the position where the line profile, shown in panel (i) was measured. (j) Simulated MAADF image. The scale bars in panels (a) - (f) are 2 nm and 0.5 nm in (g), (h) and (j).

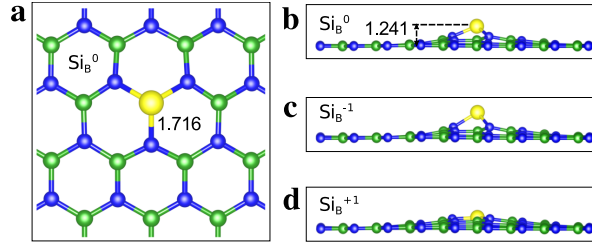


Figure 4.2: **Atomic structure of Si in boron vacancy.** (a) Top view of locally optimized Si impurity in a boron vacancy. (b) - (d) Side views on Si impurity at different charge states with resulting calculated elevations with respect to the hBN plane.

### Interpretation of ADF images using DFT calculations

To simulate MAADF images of Si impurities in the hBN lattice, the QSTEM package [133] was used and the parameters were set to correspond to the experimental setup. One of the resulting images is shown in figure 4.1 (j). The simulated result is in good correspondence with the experimental image in figure 4.1(h). In both, the experimental and simulated STEM - MAADF data the projected Si - N distance is about 1.55 Å.

Structural optimization and calculation of the energetics of different impurity atom configurations were carried out with density functional theory. In accordance to the experimental results, the more favorable substitutional site is indeed a boron vacancy. Figure 4.2 (a) shows again a top view on a locally optimized simulated impurity structure. The distance between N and Si was calculated to be 1.716 Å. In comparison, the B - N distance in a pristine structure is 1.45 Å. From these simulations it can be shown that a Si impurity induces non-flatness in the nearest neighbours, depending on the charge state of the Si atom. This buckling was calculated for three different charge states. In a neutral charge state (figure 4.2 (b)) the displacement orthogonal to the hBN plane is 1.241 Å. At a charge state of +1 it is 1.63 Å and 1.82 Å for a charge state of -1.

## 4.2 Analysis of K intercalated carbon nano-onions

In this study carbon nano-onions were investigated via dedicated STEM. The first set of specimen were pristine carbon nano-onions, the second set were carbon nano-onions with intercalated potassium. With atomic resolution STEM imaging and EELS the structural influences due to potassium intercalation were investigated.

The specimen were produced at the Friedrich-Alexander-Universität Erlangen-Nürnberg. As potassium is highly reactive, the sample powders were produced in a glove box in argon atmosphere. To prevent oxidative processes during the transport, the powders were vacuum sealed in glass vials. On site of the STEM the vials were broken in the local argon glove box and prepared further on TEM grids. Here a small fraction of powder was grounded between glass slides, then the TEM grid was carefully pressed between the two slides. The prepared TEM specimen were then mounted on the STEM specimen holder and under UHV conditions inserted into the microscope.

The specimen were imaged using both the MAADF and the HAADF detector. The first offers better contrast, but also includes channelling effects due to sample thickness. For the specimen containing intercalated potassium, only the HAADF detector was used, as brightness contrast due to channeling effects can give misleading results. With the probe corrector the probe diameter was reduced to 1.4 Å, which is of great advantage for point spectra and subsequent EELS spectrum imaging. An example of spectrum imaging is shown in figure 4.3 (c). Here every pixel of the  $256 \times 256$  pixel large array contains a spectrum of a certain energy loss range. Additionally an HAADF image was acquired. A selection of spectra is shown in figure 4.3 (d). Each spectrum had a dwell-time of 20  $\mu$ s. To smoothen the spectra, spectra of neighbouring pixels were averaged. Here areas of  $2 \times 2$  nm<sup>2</sup> were taken to average them. The most pronounced line (blue) is taken from the area with the highest brightness.

The shown spectrum differs from the others in two ways; it is higher in intensity and has a stronger pronounced peak at 306 eV energy loss.

Comparing EELS spectra of different carbon allotropes (amorphous, graphite, diamond) [134], except diamond, they have a sharp onset of the first edge at 284 eV. The following peak appears due to the transition from a  $\pi$ -bonding orbital to a  $\pi^*$ -bonding orbital and occurs in  $sp^2$  bonded materials. As diamond exhibits  $sp^3$  bonds,  $\pi^*$  transitions do not appear. At 291 eV energy loss, the onset of the second edge can be observed and is caused by transitions of a  $\sigma$ -orbital to a  $\sigma^*$ -orbital. This edge is present in EELS spectra of all carbon allotropes. Towards higher energy losses various fine-structures can be observed, depending on the material. Ionization processes in the third K-shell of a tetragonal diamond structure cause an additional peak at 306 eV energy loss [135]. From the collected spectra it might be possible that thicker, probably contaminated areas contain  $sp^3$  bonded structures.

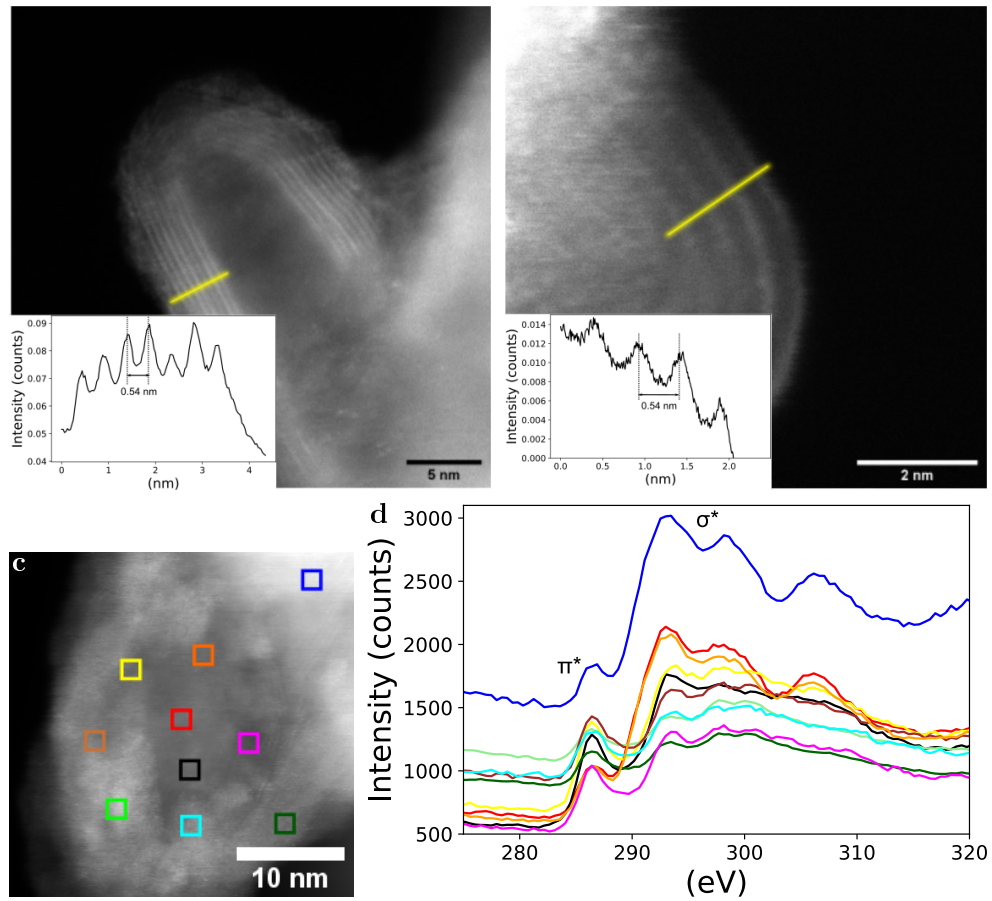


Figure 4.3: **ADF imaging and EELS of carbon nano-onion.** (a) Pristine carbon nano-onion. The yellow line marks the position of the line profile (inset). (b) Carbon nano-onion with intercalated potassium. The yellow line marks the position of the line profile (inset). (c) Spectrum image with  $256 \times 256$  pixels of a potassium-intercalated carbon-nano-onion. The colored squares mark positions where spectra were averaged. (d) The averaged spectra of the positions marked in (c).

## EELS of pristine carbon nano-onions

Pristine carbon nano-onions were prepared without contact to potassium. These specimen showed no sensitivity to air. Figure 4.4 (a) shows a typical MAADF STEM image. The presented onion has six shells and the innermost shell was not filled, what is indicated by the visible moiré pattern.

In figure 4.4 (b) two EELS spectra of two positions in the onion are shown. The turquoise spectrum was taken at the centre of the onion and the purple further away from the center. Both curves show similar behavior and show typical EELS spectra of pristine carbon nano-onions. Similar spectra could be observed on other positions of the pristine specimen.

The EELS spectra differ from those taken from areas where potassium was intercalated in carbon nano-onions. The spectra of the pristine specimen show less structure at energy losses between 290 - 310 eV.

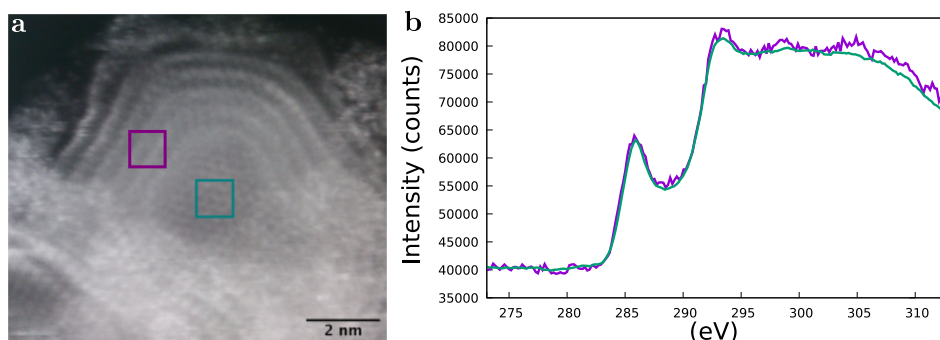


Figure 4.4: **Pristine carbon nano-onions.** (a) Pristine carbon-nano-onion with (b) corresponding EEL spectra. The turquoise spectrum was taken in the centre, the purple at the outer region of the onion.

## EELS spectrum images of potassium intercalated carbon nano-onions

Images taken from postassium-intercalated carbon nano-onions look different than their pristine counterparts. As could be seen in figure 4.3 (b) and (c) areas close to the centre of the onion do not show moiré patterns. The EELS spectra of these onions differ within single onions. To quantitatively analyze them, spectrum images at several positions were taken. To generate those, rasters of

either  $128 \times 128$  or  $256 \times 256$  were defined, with a dwell time of the STEM probe of  $20 \mu\text{s}$  at one position before continuing to the next scan position. A map of EELS spectra at every probe position, with an according HAADF image was produced. Due to the reduced image size, compared to previously taken STEM images ( $1024 \times 1024$  px), the resolution is much lower. As taking spectrum images is a compromise between resolution, acquisition time and specimen drift. The specimen presented in figure 4.5 showed remarkable stability during acquisition.

The first row in figure 4.5 (a,e,i,m) shows the according HAADF images at energy losses between 284 - 287 eV, the position of the carbon edge. The second row in figure 4.5 (b,f,j,n) shows the according HAADF images at energy losses between 294 - 297 eV. At these energy loss positions are the L edges of potassium ( $L_3 = 294$  eV,  $L_2 = 296$  eV).

Comparing HAADF images of single onions at different energy losses show different intensities in the images. It can be assumed that the onions have rather spherical symmetry, therefore the EELS signals inside the shells itself are similar for those regions (compare to figure 4.4).

The third column (figure 4.5 (c,g,k,o)) shows the intensity ratio of the spectrum images of the first and the second row. Black areas correspond to a ratio of one, and bright areas to higher contributions due to the potassium. Line profiles were taken along the indicated yellow line. All of them indicate higher intensities in spectrum images at energy losses corresponding to the  $L_{2,3}$  edges of potassium.

From these results the presence of potassium within the innermost shell of the intercalated carbon nano-onions can be concluded. From the noise in the data it can additionally be assumed that potassium is part of the contamination, outside of the onions. Both the contamination as well as the filling of the onions with potassium is a hindrance to HRSTEM imaging. Therefore, purely relying on contrast in HAADF imaging to show the presence of potassium was not possible.

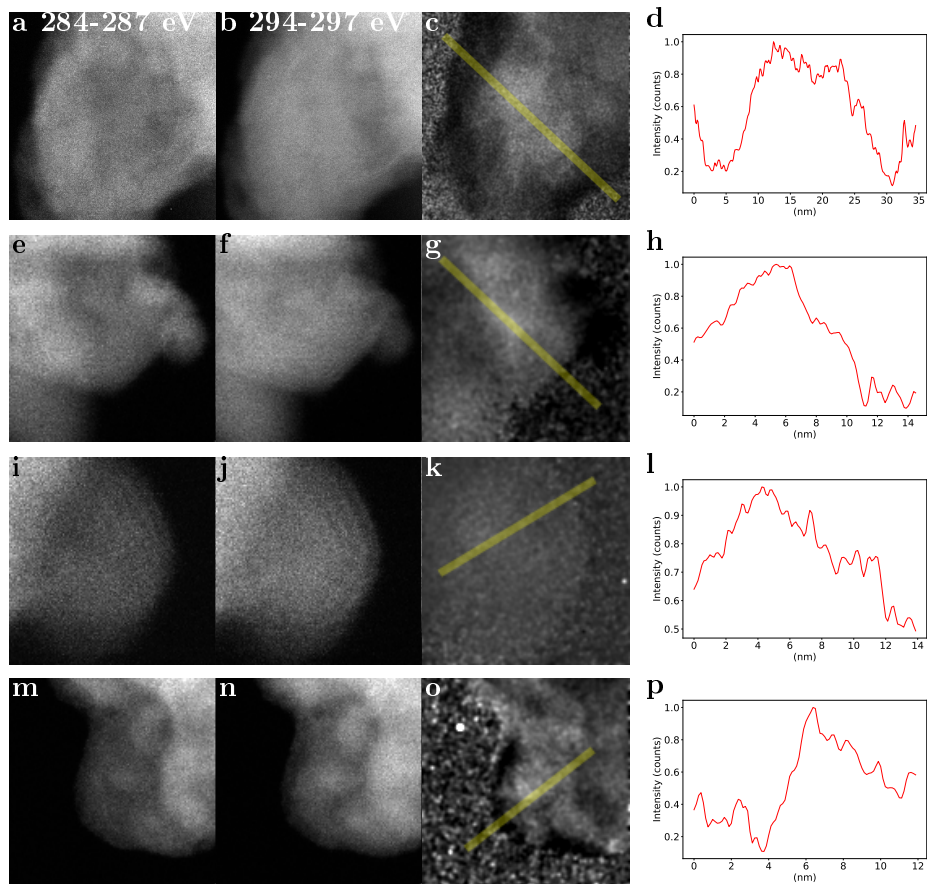


Figure 4.5: **Spectrum images of carbon nano-onions.** (a) Spectrum image at an energy loss of 284 - 287 eV, at a FOV of 32 nm. (b) Spectrum image at an energy loss of 294 - 297 eV. (c) Ratio image of (a) and (b). The dark areas correspond to a ratio of 1. (d) Line profile of the yellow marked line in (c). (e) Spectrum image at an energy loss of 284 - 287 eV, at a FOV of 16 nm. (f) Spectrum image at an energy loss of 294 - 297 eV. (g) Ratio image of (e) and (f). The dark areas correspond to a ratio of 1. (h) Line profile of the yellow marked line in (f). (i) Spectrum image at an energy loss of 284 - 287 eV, at a FOV of 16 nm. (j) Spectrum image at an energy loss of 294 - 297 eV. (k) Ratio image of (i) and (j). The dark areas correspond to a ratio of 1, where the intensities are equal in both images. (l) Line profile of the yellow marked line in (k). (m) Spectrum image at an energy loss of 284 - 287 eV, at a FOV of 16 nm. (n) Spectrum image at an energy loss of 294 - 297 eV. (o) Ratio image of (m) and (n). The dark areas correspond to a ratio of 1. (p) Line profile of the yellow marked line in (o).

### 4.3 Electron scattering factors in transmission electron microscopy

Results presented here were published in *Ultramicroscopy* [136] and referred to in the list of publications in section 1.

Diffraction patterns represent the symmetry and the orientation of a crystalline specimen in reciprocal space. They can also give insight to the composition of a specimen if the basis of the lattice contains more than one type of atoms. The underlying lattice symmetry can be found in the intensity ratios between neighboring diffraction spots within one order. Therefore, in graphene, a material with two carbon atoms in the unit cell, the ratio of the intensities between two neighboring spots of the same order is one. However, there are significant differences between the spot intensities from one set of lattice planes to another. In figure 4.6 (a) a diffraction pattern of graphene and in figure 4.6 (b) a typical diffraction patterns of monolayered hBN are shown. It has a hexagonal lattice similar to graphene but with alternating boron and nitrogen being nearest neighbors to each other. Boron has atomic number five and nitrogen has atomic number seven. Both the Rutherford scattering cross section as well as the atomic form factor  $f_a$  contain the atomic number. For pristine hBN the intensity distribution within a diffraction pattern is different to that of graphene. This is because the basis of hBN is built of atoms with different atomic form factors  $f_a$ . Uneven orders of Bragg reflexes contain diffraction information of lattice planes in zig-zag direction. Only atoms of one type of form factor contribute to the scattering intensity of opposing sets of Bragg reflexes, as can be seen in figure 4.6 (b). Even orders contain diffraction information of lattice planes with both form factors in one plane. The spots of the second order on the other hand exhibit all same intensity and the third order again show alternating intensity distribution.

Diffraction patterns from MoS<sub>2</sub> was analyzed in a similar manner. Both hBN and MoS<sub>2</sub> have a threefold symmetry, which can be seen as alternating

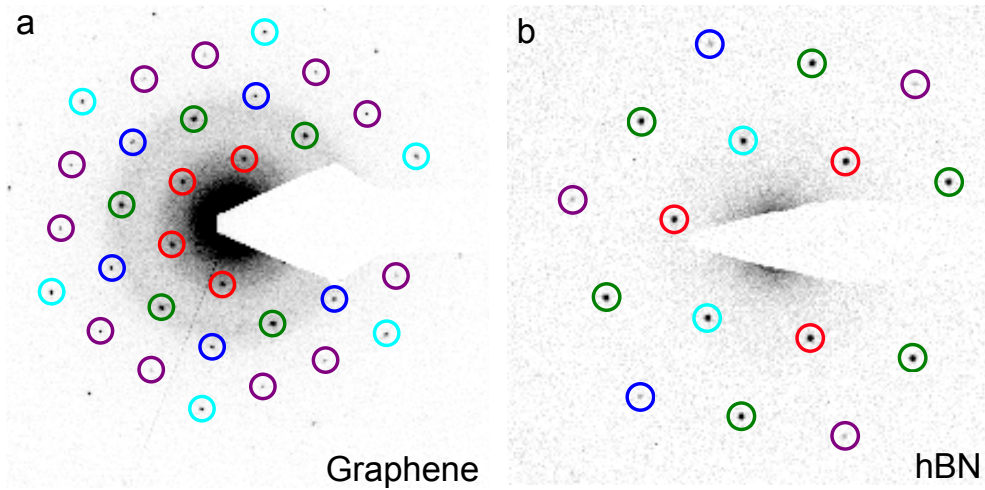


Figure 4.6: **Diffraction patterns.** (a) Diffraction patterns of graphene with marked diffraction spots. (b) Diffraction patterns of hBN with marked diffraction spots. The colored rings are used for table 4.1.

intensities. In this case the unit cell consists (in top-view) of two sulfur atoms, with an atomic number of 16, on top of each other and one molybdenum atom with an atomic number of 42. Therefore, the scattering is different from that of single-layered graphene or hBN.

To evaluate the diffraction patterns, an algorithm was used to analyze all experimental data. The algorithm (see appendix A) locates automatically the diffraction spots by finding the intensity maxima. A square of  $60 \times 60$  pixels<sup>2</sup>, shown in Figure 4.7, was used for the peak fitting algorithm. Within this square a circular area was used to calculate the intensity of the diffraction spot. The area between the inner red and the outer red circle around the diffraction spot was used for background subtraction. After background subtraction, the mean intensity within the inner circle was calculated.

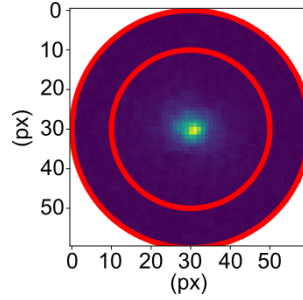


Figure 4.7: **Intensity determination of a single diffraction spot.** Cropped image around a diffraction spot located within the analyzed diffraction pattern. The mean pixel value of the area between the inner and outer red ring was used for background subtraction.

The diffraction patterns of graphene and  $\text{MoS}_2$  were taken with an aberration corrected Titan 80-300(S)TEM, whereas the diffraction patterns of hBN were recorded both with a Phillips CM200 and the Titan. The used accelerating voltage was 80 kV. The graphene samples were industrially produced (Graphenea) single layers, as prepared on TEM grids with an amorphous carbon foil (Quantifoil<sup>TM</sup>). Single-layered hBN and the single-layered  $\text{MoS}_2$  were synthesized by CVD and subsequently transferred onto TEM grids with an amorphous carbon foil (Quantifoil<sup>TM</sup>).

Using first principle simulation techniques, the intensity ratios for hBN and graphene were predicted for different orders of diffraction spots. In pristine graphene, as shown in table 4.1, the intensity ratio of diffraction spots within one family of Bragg reflexes is one. Also the ratio between the first and second order diffraction spots of Bragg reflexes, is one. For higher orders, the intensities within each set drastically drop but the intensities within each set are the same.

Table 4.1: **Electron diffraction pattern spot intensities**. Data from experiment and different simulations  $\bullet = 1$  (see figure 4.6 for the color code. See Ref. [136] for discussions on the simulations.

Graphene	● (green)	● (blue)	● (purple)	● (cyan)
Experiment	1.03	0.16	0.05	0.12
Wien2k	1.10	0.18	0.06	0.15
GPAW	1.11	0.18	0.06	0.15
IAM	0.89	0.14	0.05	0.12
DWF ratio	0.93	0.89	0.79	0.74
Wien2k×DWF	1.02	0.14	0.05	0.11
GPAW×DWF	1.03	0.14	0.05	0.11
IAM×DWF	0.83	0.12	0.04	0.09

hBN	● (cyan)	● (green)	● (blue)	● (purple)
Experiment	1.05	1.07	0.19	0.19
Wien2k	1.05	1.17	0.16	0.17
GAPW	1.06	1.16	0.16	0.17
IAM	1.07	0.95	0.13	0.13
DWF ratio	1	0.93	0.89	0.89
Wien2k×DWF	1.05	1.09	0.15	0.16
GPAW×DWF	1.06	1.08	0.15	0.16
IAM×DWF	1.07	0.88	0.11	0.11

## 4.4 Ripples in different 2D materials

The results of this study were published in *npj 2D Materials and Applications* and referred to in the list of publications in section 1.

The aim of this study was to investigate and compare the out-of-plane structures of graphene, hBN and MoS<sub>2</sub>. Specimen of hBN and MoS<sub>2</sub> were prepared from CVD grown samples. In the case of graphene the effect of two different common specimen production techniques on intrinsic corrugation was an additional research question. The investigated graphene specimen were commercially available as-prepared graphene on TEM grids (Graphenea) and mechanically exfoliated graphene. Also different vdW heterostructures from these 2D materials were prepared and investigated for their intrinsic corrugations. The studied combinations of 2D materials were: graphene-hBN, graphene-MoS<sub>2</sub> and graphene-graphene vertical stackings.

As discussed in section 3.4, diffraction techniques are suitable to quantitatively measure out-of-plane ripples in 2D materials. From the technical point of view the influences of different experimental set-ups have been compared. The first sets of experiments on graphene, hBN, MoS<sub>2</sub>, graphene-hBN and graphene-MoS<sub>2</sub> were conducted in the uncorrected TEM with a standard CCD camera. Later experiments were conducted in an image corrected TEM. As this instrument is equipped with a post-specimen energy filter, the influences of inelastic scattering on the experimental results could also be determined. For a quantitative analysis the experimental data was compared with simulated diffraction patterns.

### **Simulations of corrugated 2D materials**

Software packages to simulate diffraction patterns are valuable tools for understanding the underlying structure, as scattering behavior is directly related to physical deformations. In the following studies TEM simulations have been used to simulate diffraction patterns of certain 2D structures with corrugations with different wavelengths (characterized by  $\gamma_{Root\ Mean\ Square} - \gamma_{RMS}$ ), at different tilt angles. High values of  $\gamma_{RMS}$  correspond to highly corrugated structures. When tilting the specimen, the tilt-axis can be identified as the axis of least change. Diffraction spots within this axis remain unaffected by the tilt, both from their positioning and their cross-sectional form. For a flat specimen the size of the diffraction spot remains unchanged regardless of the tilt angle. For corrugated specimens the size of the diffraction spot away from the tilt axis increases linearly as a function of the tilt angle with a slope of  $\sigma$  that can be correlated to  $\gamma_{RMS}$ . Flatter 2D membranes have smaller values  $\sigma$  and therefore smaller  $\gamma_{RMS}$ .

In the experiments, the only direct measurement from the diffraction patterns is the slope  $\sigma$ , which needs to be translated into the corresponding  $\gamma_{RMS}$ . For this purpose, we calculated diffraction patterns with the Large-Scale Atomic/Molecular Massively Parallel Simulator (LAMMPS) [137, 138, 139] at different tilt-angles.

Such simulations were conducted for graphene, hBN and MoS<sub>2</sub> with the following parameters.

Corrugated graphene specimens were simulated using  $\sim 24,000$  carbon atoms. In order to simulate a corrugated graphene lattice, the model was strained and heated up for 5 ns to 6 K and cooled down for 8 ns to 0.1 K and partially relaxed at the end. Diffraction patterns were calculated for five different states of relaxed graphene. Although  $\sigma$  does depend on the distance between the diffraction spot and the origin of the reciprocal space, it has only a minor influence on the  $\sigma/\alpha$  relationship, which is used here to estimate  $\gamma_{RMS}$ . The interaction between carbon atoms were treated using the long-range bond-order potential for carbon (LCBOP) potential [140]. The inclination was estimated from the surface normals calculated for the atomic structure divided into triangles defined by each carbon atom and two of its neighbors. The resulting simulated diffraction pattern for graphene are shown in figures figure 4.8 (a) - (d). A diffraction pattern of an untilted, only slightly corrugated graphene structure is shown in figure 4.8 (a). Here the  $\gamma_{RMS} = 5^\circ$ . The streaks in  $x$  and  $y$  direction at each simulated diffraction spot are artefacts due to the present boundary conditions. The diffraction spots themselves are sharp spots. In figure 4.8 (b) the same structure is tilted by  $30^\circ$ . The diffraction pattern shows an elliptical arrangement of the simulated spots, which is an effect of the tilt.

Figure 4.8 (c) shows an un-tilted but more corrugated graphene diffraction pattern with  $\gamma_{RMS} = 7.8^\circ$ . In figure 4.8 (d) the same structure is tilted to  $30^\circ$ , where broadening of the diffraction spots can be observed.

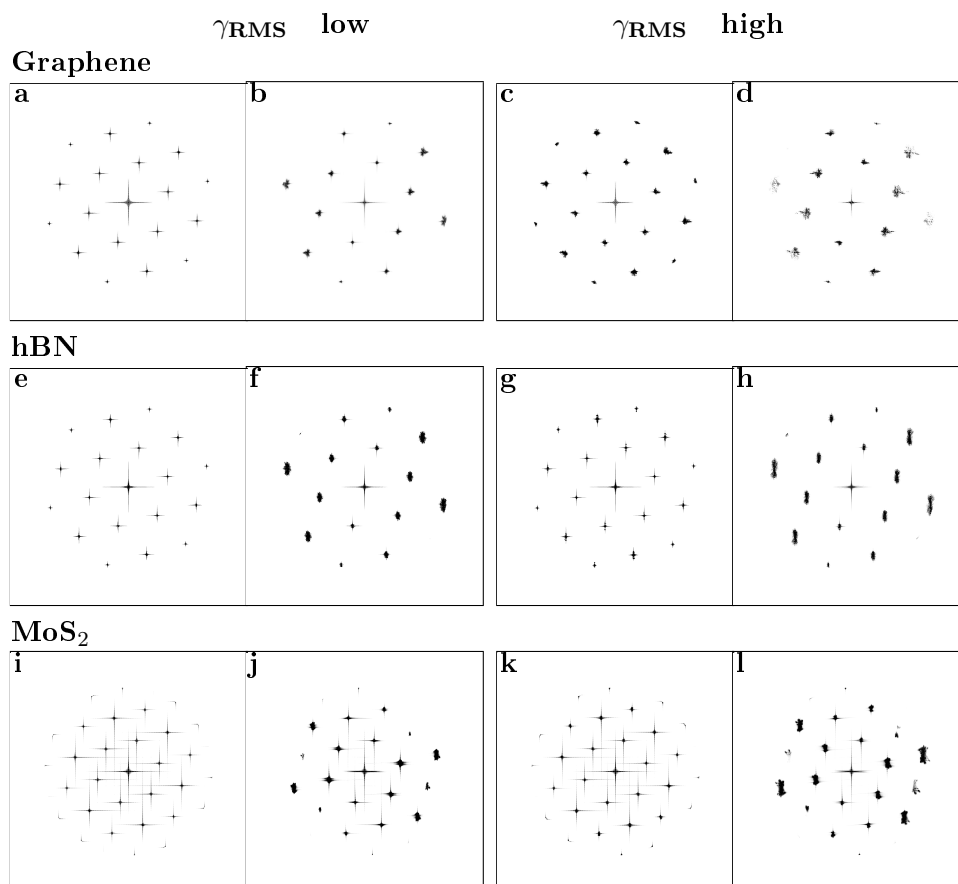


Figure 4.8: **Simulated diffraction patterns.** Reciprocal representation of graphene membrane with  $\gamma_{RMS} = 5$  at  $0^\circ$  specimen tilt (a) and at  $30^\circ$  specimen tilt (b). Representation of a graphene membrane with  $\gamma_{RMS} = 7.8$  at  $0^\circ$  tilt (c) and at  $30^\circ$  specimen tilt (d). (e) Representation of a hBN membrane with  $\gamma_{RMS} = 5$  at  $0^\circ$  tilt and at (f)  $30^\circ$  tilt. (g) Representation of a hBN membrane with  $\gamma_{RMS} = 7.8$  at  $0^\circ$  tilt and (h) at  $30^\circ$  tilt. (i) Representation of a MoS<sub>2</sub> membrane with  $\gamma_{RMS} = 3.75$  at  $0^\circ$  tilt and (j) at  $30^\circ$  tilt. (k) Representation of a MoS<sub>2</sub> membrane with  $\gamma_{RMS} = 7.2$  at  $0^\circ$  specimen tilt and (l) at  $30^\circ$  tilt (d).

Figure 4.8 (e) - (h) show simulated diffraction pattern of hBN with two different  $\gamma_{RMS}$  values. Figure 4.8 (e) shows the diffraction pattern of untilted hBN with  $\gamma_{RMS} = 4^\circ$ , whereas figure 4.8 (g) shows the structure at  $30^\circ$  tilt. Figure 4.8 (f) and (h) show hBN with a  $\gamma_{RMS} = 7.8^\circ$  at  $0^\circ$  (e) and  $30^\circ$  (f) specimen tilt. The simulations for hBN were conducted with the assumption of oriented ripples. Orientations of corrugations can be observed in real specimens as well and will be discussed in more detail in section 4.5. Figure 4.8 (i) - (l) show simulated diffraction patterns of MoS<sub>2</sub> with two different  $\gamma_{RMS}$  values. Figure 4.8 (i) shows the diffraction pattern of untilted MoS<sub>2</sub> with a  $\gamma_{RMS}$  value of 3.2. Figure 4.8 (k) shows a diffraction pattern of the structure at  $30^\circ$  tilt. In figures 4.8 (k) and (l), diffraction pattern of MoS<sub>2</sub> with  $\gamma_{RMS} = 7.2^\circ$  at  $0^\circ$  (i) and  $30^\circ$  (j) tilt angle are shown. Similar to the simulations for hBN, those for MoS<sub>2</sub> were as well conducted with the assumption of oriented ripples. For an untilted MoS<sub>2</sub> specimen the structure is hexagonal. At larger tilts (shown in figure 4.8 (l)) diffraction spots in direction orthogonal to the tilt axis have a slightly different shape, due the different lattice structure compared to the other shown materials.

### **Evaluation of diffraction patterns during a tilt series**

All evaluated diffraction patterns were obtained in an accurately aligned microscope and the specimen was positioned at eucentric height. Both the experimentally obtained as well as the simulated patterns for each material and the estimated  $\gamma_{RMS}$  values, were analyzed with two similar algorithms. The algorithms find the first order diffraction peaks via finding maximum values above a certain threshold. For non-energy-filtered diffraction pattern, especially at higher tilt angles, the data can be noisy and the algorithm has a higher risk of failure.

For an automated peak-finding routine, the image is blurred via Gaussian blur beforehand. To select only spots within one order of diffraction spots, a circular mask excludes all undesired parts of the patterns. Subsequently each of the experimentally obtained diffraction spots is then fitted by two 2D

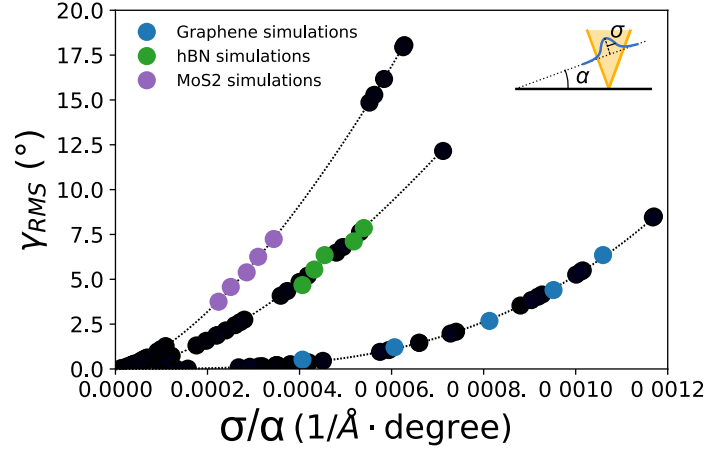


Figure 4.9: **Relationship between the diffraction spot size ( $\sigma$ ) and the sample tilt ( $\alpha$ ).** The blue markers are selected results of simulations of graphene, the green ones of hBN and purple MoS<sub>2</sub>. The dashed lines are fits to  $y(x) = kx^c$  for each material. The black marker represent experimental data.

Gaussian functions with widths  $\sigma_1$  and  $\sigma_2$ , which are then saved into a text-file. These two functions allow separation of the electron source-related broadening and the specimen response function [115]. The latter contains the information about the corrugations from the specimen.

For the simulated diffraction patterns only one 2D Gaussian function was used as the diffraction spots in the simulated patterns do not contain the contribution of the electron source. In the second algorithm, the peak broadening was plotted for each tilt series as a function of the tilt angle. The slopes of the linear fits were extracted and compared to slope values of simulated diffraction patterns. Here it could be observed that the relation between the slope value  $\sigma$  and the roughness  $\gamma_{RMS}$  is not linear. The results are shown in figure 4.9 for graphene, hBN and MoS<sub>2</sub>. From the relationship shown here  $\gamma_{RMS}$  corresponding to any experimental value can be observed.

### Experiments at uncorrected and corrected TEMs

As the roughness of 2D materials decreases with increasing layer number [7], the chosen experimental areas need to be carefully selected to guarantee proper

results. To guarantee best results only intact freestanding, monolayered membranes were chosen. The circular holes in the amorphous carbon support film needed to be fully covered by the material of interest.

Mono-layered areas in vicinity of multi-layered were also avoided, as they might influence the intrinsic corrugations. Ideally one should ensure the suitability of the selected areas with atomic resolution imaging, which also allows estimating the amount of contamination that may influence the results by altering the structure and increasing the number of inelastic scattering events, leading to a general broadening of diffraction spots. For energy filtered diffraction patterns, influences of contamination become less relevant. Nonetheless heavily contaminated areas were avoided as they might influence the roughness of the membrane. Clean, large monocrystalline areas were therefore preferred for this study.

Most of the investigations of the vdW heterostructures were conducted at the Titan 80-300 (S)TEM. A 150 nm SA aperture was used for taking the diffraction pattern. Figure 4.13 (a) shows the moiré structure of the two materials with similar lattice constants (bond length C-C graphene: 0.142 nm; bond length B-N hBN: 0.144 nm). In the vdW heterostructure of graphene and MoS<sub>2</sub>, the lattice mismatch is much larger (distance Mo-S: 0.3161 nm), as can be observed in the diffraction pattern. Due to the weaker scattering of graphene as compared to MoS<sub>2</sub>, its structure is not directly visible in real space images. However, the presence of graphene manifests itself as an intensity undulation in the image. By taking a FFT of the area also graphene can be revealed.

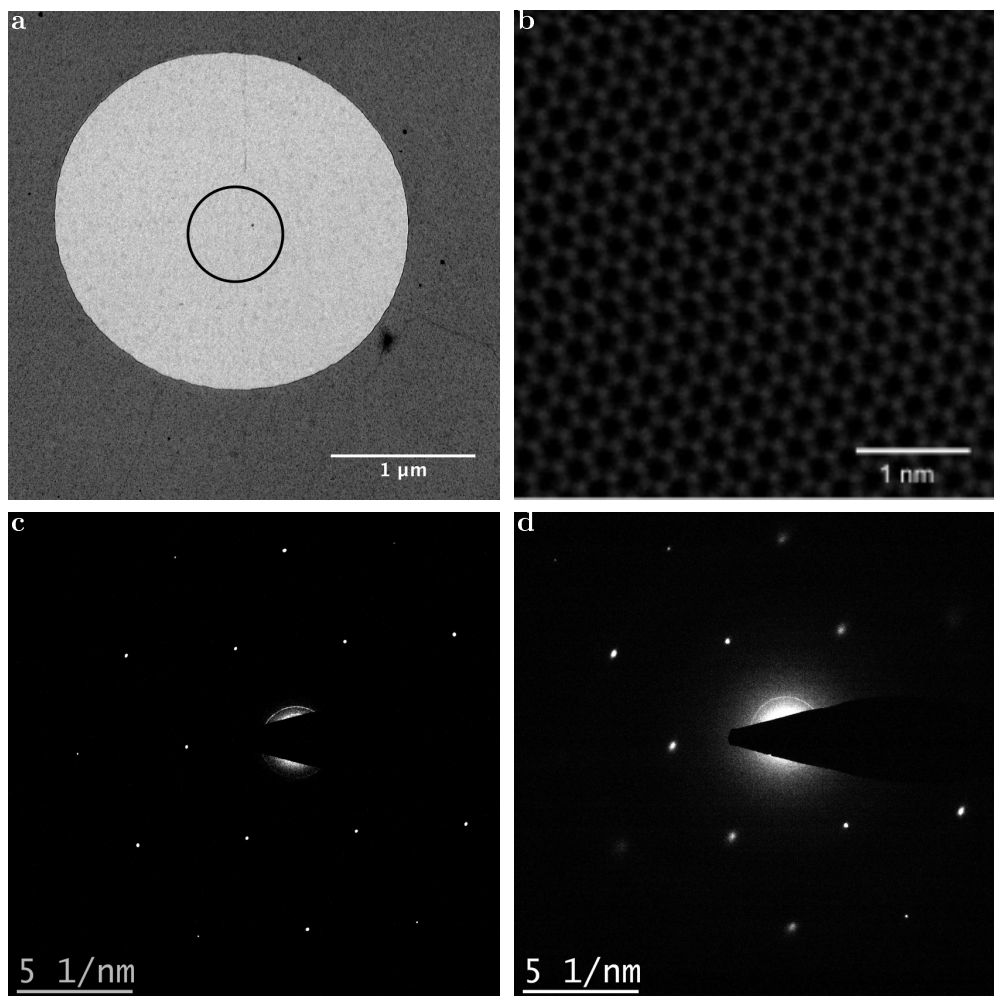


Figure 4.10: **Graphene.** (a) TEM image of graphene suspended on a holey amorphous carbon membrane. The black circle marks the area used for STEM imaging and tilt series. (b) Atomic resolution MAADF STEM image from within the marked area. Diffraction pattern of the marked area at (c) 0° and (d) 21° specimen tilt.

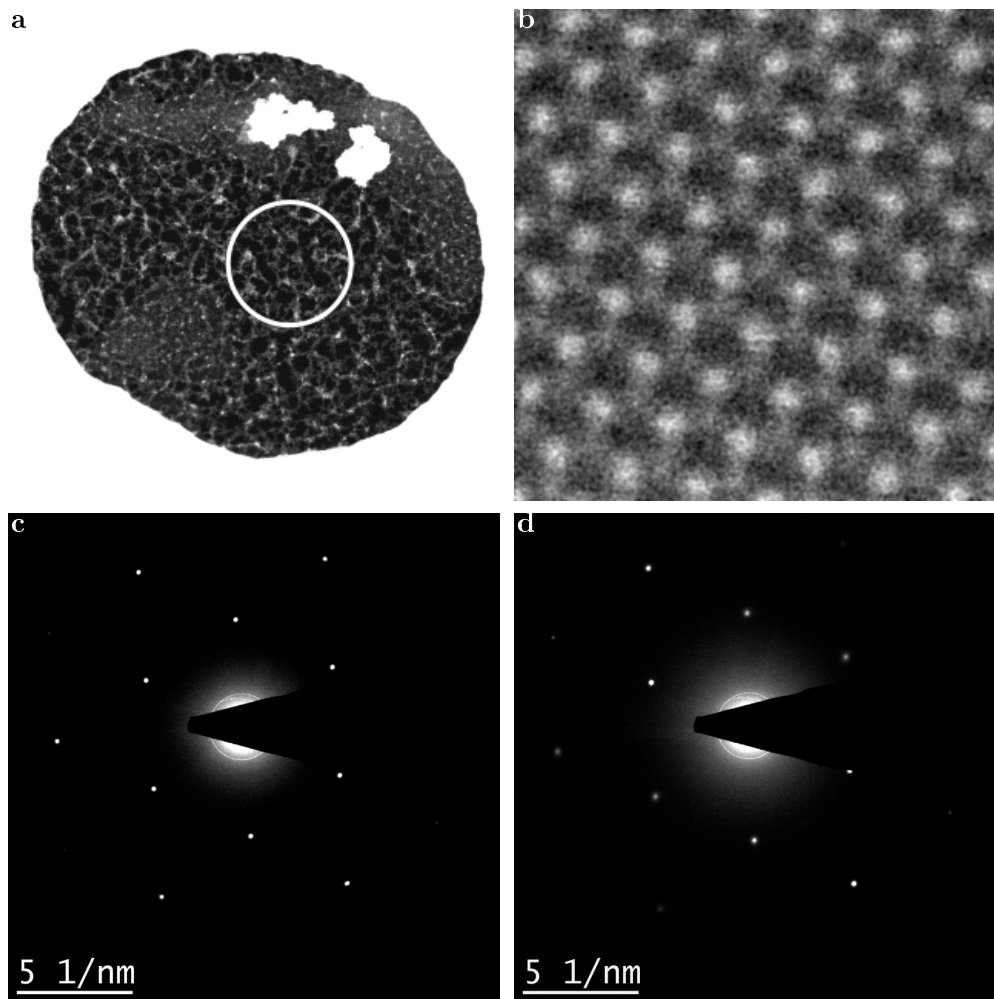


Figure 4.11: **hBN**. (a) MAADF STEM image of hBN suspended on a holey amorphous carbon membrane. The white circle marks the area used for STEM imaging and tilt series. (b) Atomic resolution MAADF STEM image from within the marked area. Diffraction pattern of the marked area at (c) 0° and (d) 21° specimen tilt.

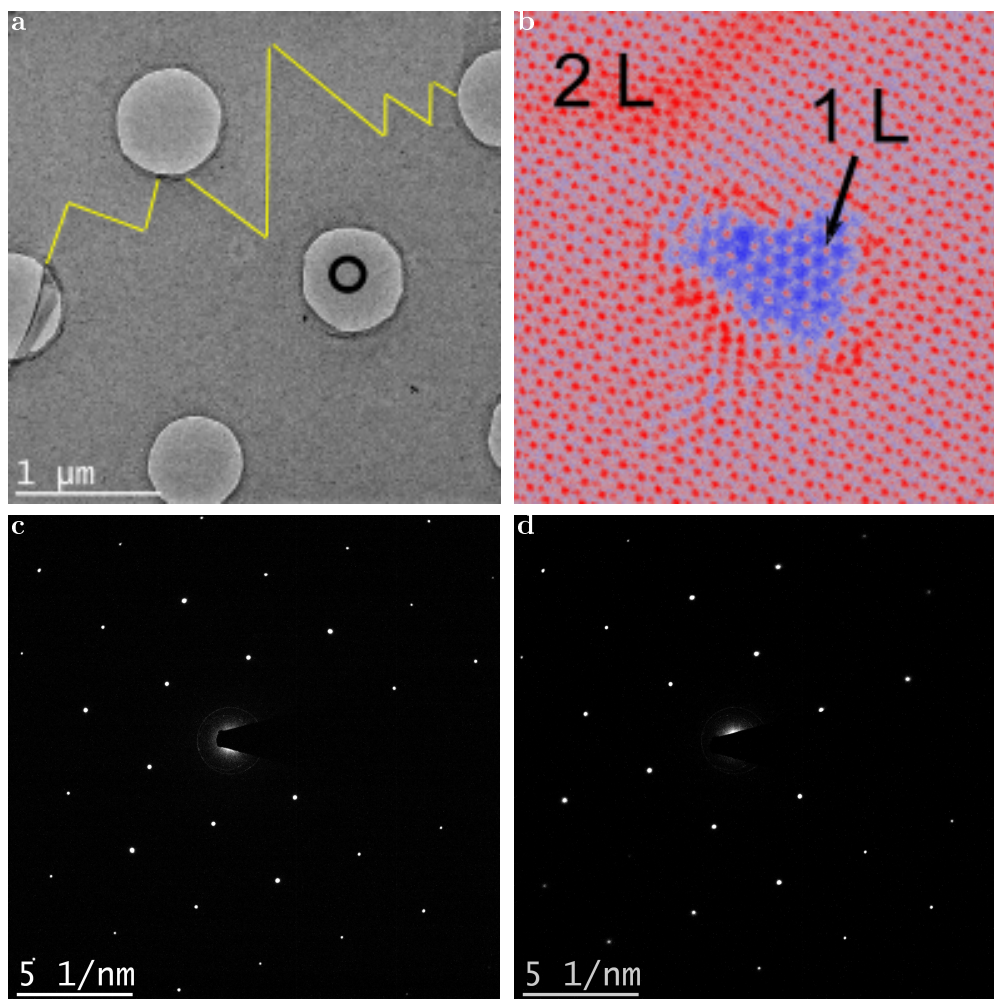


Figure 4.12: **MoS<sub>2</sub>**. TEM image of MoS<sub>2</sub> suspended on a holey amorphous carbon membrane. The black circle marks the area used for STEM imaging and tilt series. In this figure the edge of the MoS<sub>2</sub> membrane is marked with a yellow line. (b) Atomic resolution HAADF STEM image of a different region than that used for the tilt series to show the pronounced contrast difference between a bilayered (2L) and a monolayered (1L) MoS<sub>2</sub> membrane. Diffraction pattern of the in (a) marked area at (c) 0° and (d) 21° specimen tilt.

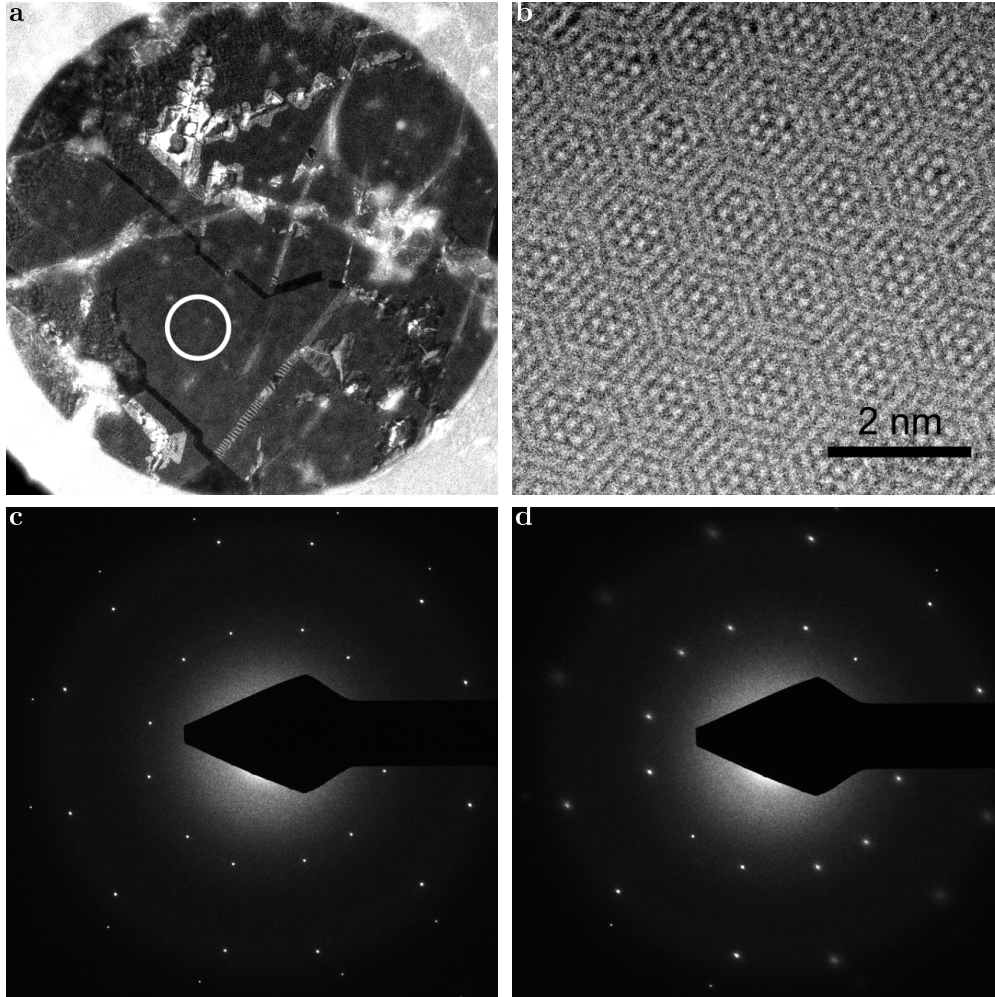


Figure 4.13: **Graphene-hBN vdW heterostructure.** DF TEM image of graphene-hBN vdW heterostructure. For this image a first order Bragg reflection of hBN was used. The white circle marks the area used for HRTEM imaging and tilt series. (b) HRTEM image from within the marked area with dark atom contrast. Diffraction pattern of the marked area at (c)  $0^\circ$  and (d)  $27^\circ$  specimen tilt.

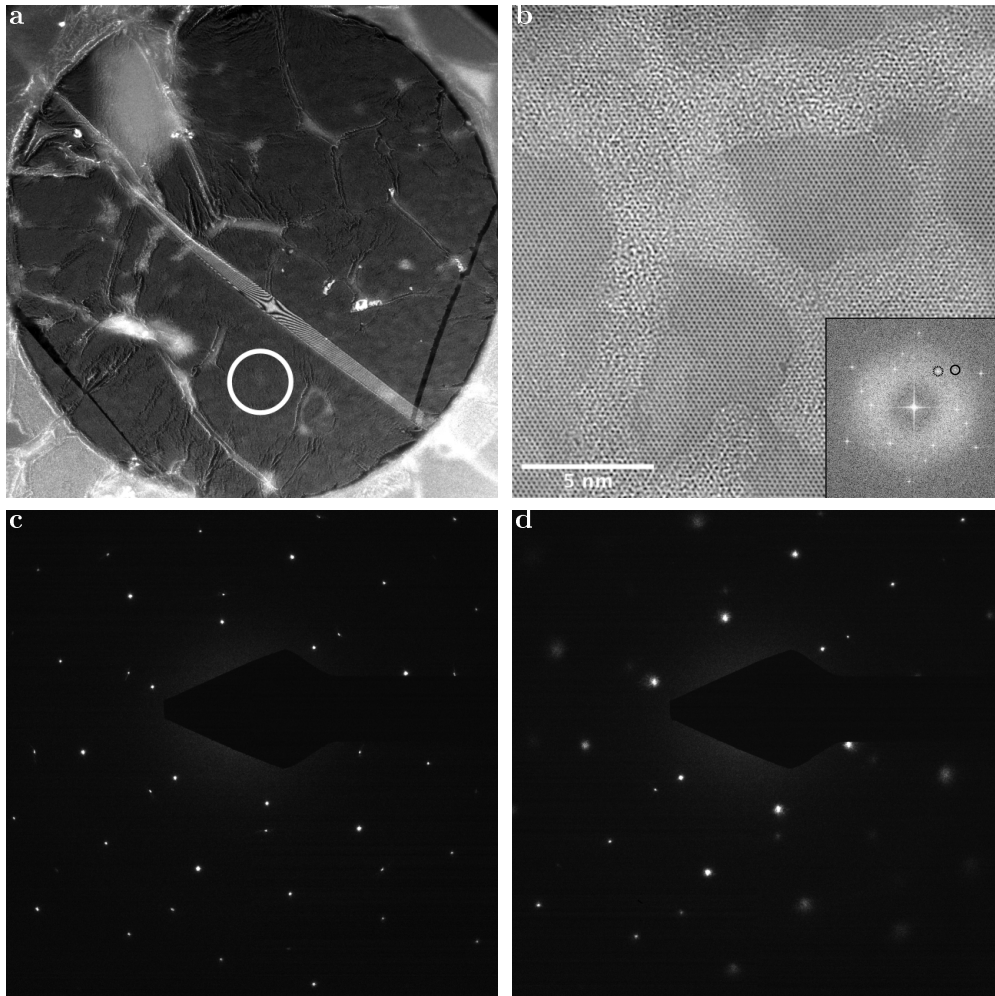


Figure 4.14: **Graphene-MoS<sub>2</sub> vdW heterostructure.** (a) DF TEM image of graphene and MoS<sub>2</sub> vdW heterostructure. For this image a first order Bragg reflex of MoS<sub>2</sub> was used. The white circle marks the area used for HRTEM imaging and tilt series. (b) HRTEM image of the marked area with dark atom contrast. The inset shows an FFT from within the area and indicates the presence of both, graphene and MoS<sub>2</sub>. Diffraction pattern of the marked area at (c) 0° and (d) 21° specimen tilt.

Because the aberration corrected Titan was installed only towards the end of this Ph.D. research, diffraction patterns were initially recorded with the Phillips CM200 TEM in a single tilt holder (section 3.3.2) and a (virtual) SA aperture of 300 nm (which is the smallest available size of SA aperture on that instrument). For experiments conducted on the uncorrected instrument the specimen were first investigated via STEM, to find suitable positions. Due to the size limitation of the SA aperture, a reasonably sized monocrystalline specimen area was needed where the SAED was placed. For commercially sold graphene specimens this is rather easy, as the crystallite sites are usually of sufficient size. For both MoS<sub>2</sub> and hBN the size of crystallites varies and were often too small for the selected area.

First a diffraction pattern was taken at zero specimen tilt. The tilt was incremented with 3° steps, at each of the incremental steps SAED patterns were taken until a tilt of 21°. This procedure was done for several specimens and positions on each of them.

### **Experimental results**

The behavior of the diffraction spots, orthogonal to the tilting axis, strongly differed from material to material. The spots oriented orthogonal to the tilting axis are those with the largest spreading in size. Representative examples of the tilt behavior of diffraction spots for the used materials are shown in figure 4.15 (a)-(e).

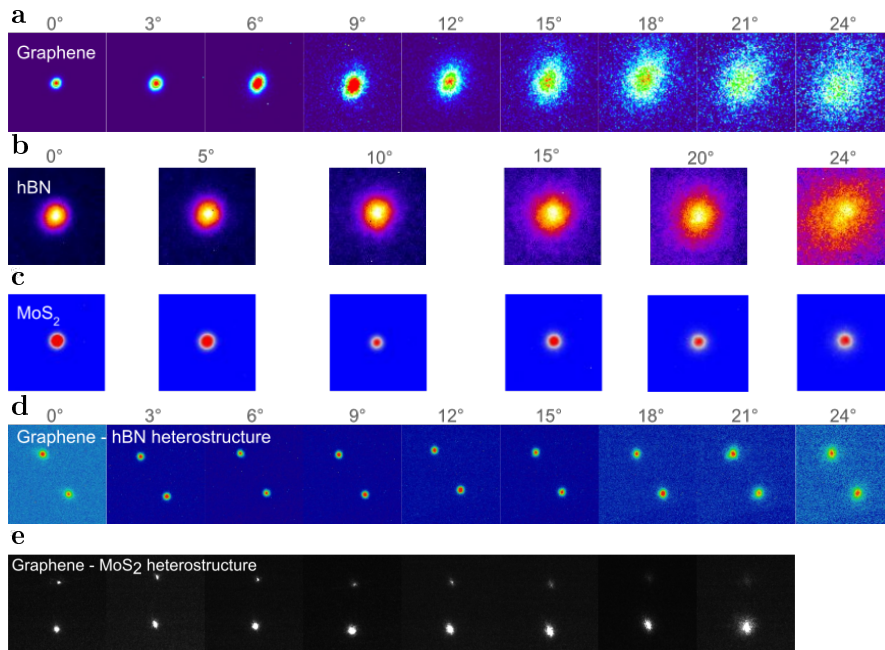


Figure 4.15: **Diffraction spots from tilting series.** Diffraction spots orthogonal to the tilt axis taken at 3 tilt angles from  $0^\circ$  to  $24^\circ$ : (a) graphene (b) hBN (c)  $\text{MoS}_2$  (d) graphene on hBN and (e) graphene on  $\text{MoS}_2$ .

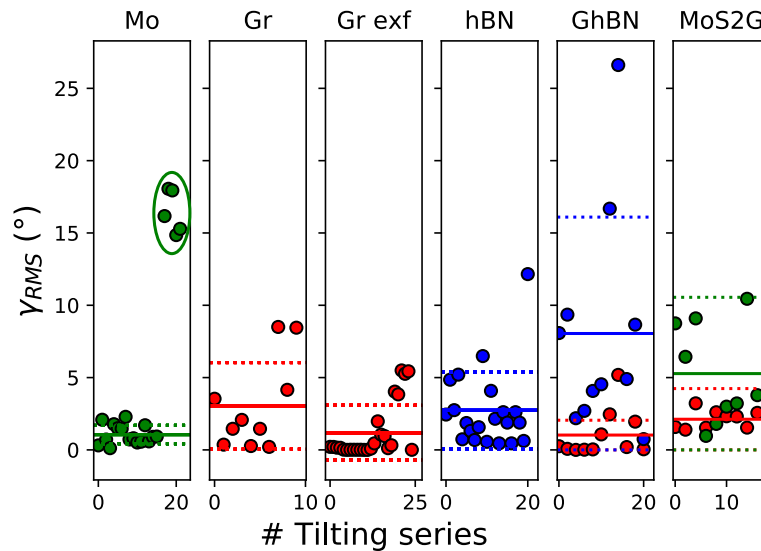


Figure 4.16: **Mean inclination of investigated materials.** On the  $x$ -axis the number of the dataset and on the  $y$ -axis the mean inclination of each dataset is shown (from left to right):  $\text{MoS}_2$ , graphene, hBN, graphene-hBN heterostructure and graphene- $\text{MoS}_2$  heterostructure. The solid lines shows the mean value and the dotted lines the standard deviation of each dataset.

As described above for simulated data, the slope of increasing diffraction spot size as a function of the tilt angle can be correlated with  $\gamma_{RMS}$ . The resulting data is presented in figure 4.16. The in figure 4.16 shown data leads to the following results: For the first dataset of MoS<sub>2</sub>, two very different measurements can be observed. The first 16 datapoints are from different CVD grown samples, and measured on different specimen areas. The samples were only investigated in electron microscopes without further treatment. The mean value of  $\gamma_{RMS}$  was measured to be  $1.96 \pm 0.7^\circ$ . The second dataset shows results from MoS<sub>2</sub> which was previously laser treated to remove contamination from the surface [141]. Unfortunately this treatment also thins out the carbon support film. Due to this thinning, the specimen is less stable and eventually starts vibrating while illuminated by the electron beam. This causes strongly diverging measurement and was as well observed in other 2D specimen. However, it was still surprising that the effects were that strong in the otherwise rather stiff material.

The datasets from graphene were split in two groups, CVD grown graphene and mechanically exfoliated. Specimen from CVD grown graphene were observed to cover large areas of the support film, whereas mechanically exfoliated graphene is often very limited in size. Nonetheless, it seems that larger flakes are more rippled than smaller ones. For CVD grown graphene a mean  $\gamma_{RMS}$  of  $3 \pm 3^\circ$  were measured and for exfoliated graphene  $1.2 \pm 1.9^\circ$ .

In the case of CVD grown hBN the results are similar to graphene with a  $\gamma_{RMS}$  of  $2.7 \pm 2.7^\circ$ . For vdW heterostructures graphene is for both structures comparably flat. In the case of graphene-hBN graphene has a  $\gamma_{RMS}$  of  $1.03 \pm 1^\circ$  and hBN  $\gamma_{RMS}$  of  $8.03 \pm 8.05^\circ$ . For a graphene-MoS<sub>2</sub> vdW heterostructure graphene shows a  $\gamma_{RMS}$  of  $2.2 \pm 1.02^\circ$  and MoS<sub>2</sub>  $\gamma_{RMS}$  of  $5.2 \pm 5.3^\circ$ . It is clear from the data that different materials are differently corrugated. For the vdW heterostructures we are able to say that the two materials very likely influence each other. For graphene on hBN it can be observed that graphene is, in most cases, flattened in comparison to freestanding graphene. Two of the datasets show strong outliers, especially for hBN. In

figure 4.17 these two datasets are compared to two more typical datasets. In figure 4.17 (a)–(d) diffraction patterns of all four datasets of untilted specimen are shown. They show slightly different lattice misorientation between graphene and hBN. Both the patterns in figure 4.17 (a) and in figure 4.17 (b) exhibit a misorientation of  $21^\circ$ , whereas that in figure 4.17 (c) is  $17^\circ$  and that in figure 4.17 (d) is  $26^\circ$ . For untilted specimen the mean widths of the first order diffraction spots of both graphene and hBN, shown in figures 4.17 (a,c,e,g) are in the same size range of  $0.3 \pm 0.05 \text{ \AA}^{-1}$ . The last tilt-angle of the series was  $24^\circ$ . The diffraction spots of the directions orthogonal to the tilt axis show a characteristic broadening. In case of a corrugated vdW heterostructure, shown in figure 4.17 (b) the broadest graphene spot has a width of  $1.5 \pm 0.2 \text{ \AA}^{-1}$  and hBN  $1.7 \pm 0.2 \text{ \AA}^{-1}$ . For the structure shown in figure 4.17 (d) the broadest graphene spot has a width of  $1.2 \pm 0.2 \text{ \AA}^{-1}$  and hBN  $1.4 \pm 0.2 \text{ \AA}^{-1}$ .

For the two vdW heterostructures exhibiting less corrugations (figure 4.17 (f)) the graphene spot with the largest broadening reaches  $0.8 \pm 0.1 \text{ \AA}^{-1}$  and is equal to that of hBN. The other rather flat heterostructure exhibits  $0.4 \pm 0.1 \text{ \AA}^{-1}$  for graphene and  $0.5 \pm 0.1 \text{ \AA}^{-1}$  for hBN.

The mean inclinations of graphene of the four series are  $2.5 \pm 0.3^\circ$  (figure 4.17 (a,b)),  $5.2 \pm 0.5^\circ$  (figure 4.17 (c,d)),  $0.2 \pm 0.03^\circ$  (figure 4.17 (e,f)) and  $0.05 \pm 0.005^\circ$  (figure 4.17 (g,h)) those of hBN are  $17 \pm 2^\circ$  (figure 4.17 (a,b)),  $26 \pm 3^\circ$  (figure 4.17 (c,d)),  $5.0 \pm 0.5^\circ$  (figure 4.17 (e,f)) and  $0.8 \pm 0.09^\circ$  (figure 4.17 (g,h)). Especially the tilt series of the specimen from figure 4.17 (a) and figure 4.17 (b) has a remarkably large number for the mean inclination of hBN. A possible explanation of this behavior is that corrugations can be influenced by the specimen preparation. During the transfer process, as described in section 3.2, hBN was attached onto CVD grown graphene already on TEM grids. It is possible that in this step more contamination has been trapped between those layers, leading to increased bulging of the hBN layer. Graphene on  $\text{MoS}_2$  exhibits a higher variation in corrugations compared to graphene on hBN. In this vdW heterostructure, graphene tends to be more corrugated than in a graphene-hBN vdW heterostructure. In some specimen,

however graphene is rather flat.

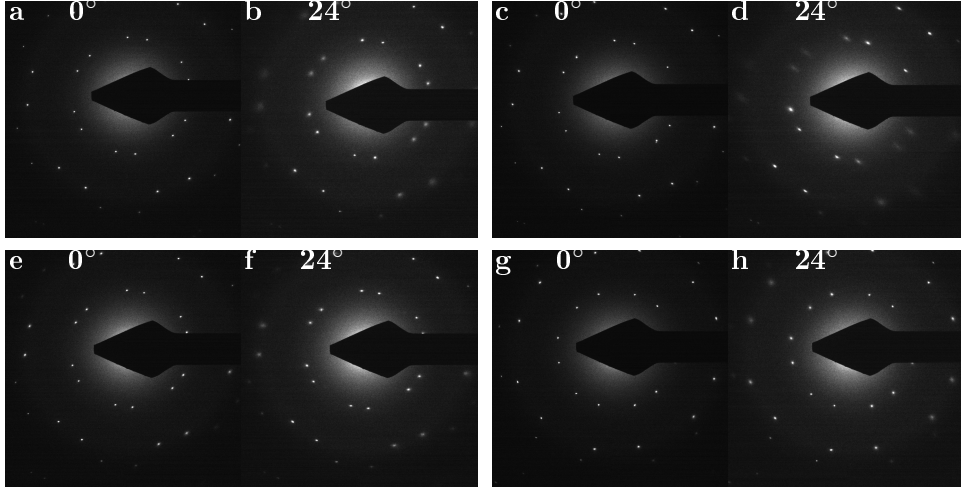


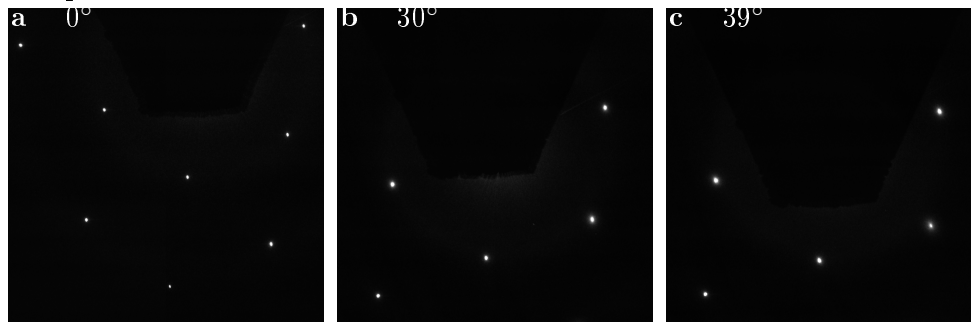
Figure 4.17: **Diffraction pattern of graphene-hBN vdW heterostructures with different mean inclinations.** (a,c) The initial diffraction patterns of graphene-hBN vdW heterostructures exhibiting high mean inclinations. (b,d) Diffraction patterns of graphene-hBN vdW heterostructures exhibiting high mean inclinations at  $24^\circ$  tilt. (e,g) Initial diffraction patterns of a graphene-hBN vdW heterostructures exhibiting lower mean inclinations. (f,h) Diffraction patterns of graphene-hBN vdW heterostructures exhibiting low mean inclinations at  $24^\circ$  tilt.

#### 4.4.1 Energy filtered analysis of diffraction patterns

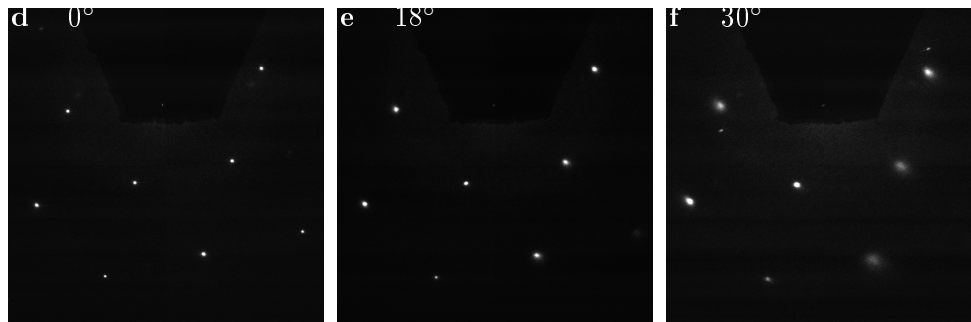
To exclude influence of inelastic scattering, zero loss filtered diffraction patterns of all structures were taken. Different material thicknesses and different amount of contamination on the specimen lead to different contributions of inelastic scattering in the whole range of spatial frequencies. As the inelastically scattered background differs between specimen it can obscure the results. The later experiments used a Titan 80-300(S)TEM equipped with a Gatan Tridiem 866 energy filter (GIF). For all experiments using this instruments, the GIF was tuned before every experiment and an energy selective slit of 10 eV was applied. As a result, the amount of specimen tilt could be drastically increased before the diffraction spots disappeared into the noise. Gladly the results obtained by use of the GIF agreed with previously obtained data. Figure 4.18

shows diffraction patterns at different specimen tilts for the three different materials.

**Graphene:**



**hBN:**



**MoS<sub>2</sub>:**

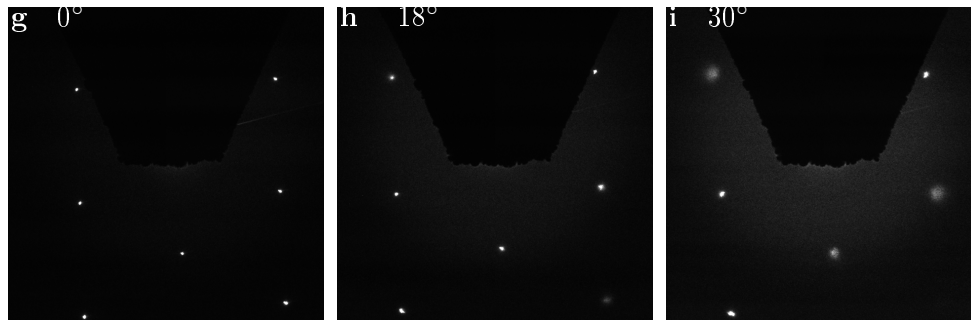


Figure 4.18: **Energy filtered diffraction patterns.** (a) Diffraction pattern of graphene untilted, (b) 30° tilt angle, (c) 39° tilt angle. (d) Diffraction pattern of hBN untilted, (e) 18° tilt angle, (f) 30° tilt angle. (g) Diffraction pattern of MoS<sub>2</sub> untilted, (e) 18° tilt angle and (f) 30° tilt angle.

## 4.5 Pulling graphene

Elastic strain offers many possibilities to alter a materials' mechanical and electronic properties. Strain can be seen as a continuously manipulable variable. Strain engineering can significantly alter the material properties. Unfortunately, for most bulk materials the range of applicable strain is rather limited. Many 2D materials can sustain much more strain [33]. Especially graphene would be an interesting candidate as it can be strained up to 20%, shown by Lee *et al.* [142].

Applying external strain onto 2D materials is a topic of widespread interest, as this could lead to applications. In 1988 Seung and Nelson discussed the subject of strain in thin, continuous membranes in the context of continuum elasticity theory. The result of their calculations lead to the conclusion that defects in thin membranes are a major cause for the buckling of the membranes [143]. Even though strain can alter the interatomic distances, it does not introduce disorder [9]. As 2D materials are rather delicate structures, it is a challenging task to strain them in a controlled manner. However, as will be shown here, it is possible, even using simple methods and techniques.

### Analytical model

The three-dimensional structure of 2D material (here graphene) can be described using molecular mechanical methods [94]. In the following model two-body and three-body interactions between nearest and second nearest neighbors were included into the calculations. With these assumptions, including fixed boundary conditions, it could already be proven that the ideal configuration of such a model material is not flat [144]. The orientation of a single ripple in the material is determined by the orientation of its smallest unit. In graphene the building unit of the lattice is a single hexagon. This consideration makes it possible to reduce the question to a one-dimensional energy optimization problem. The location of each building unit, a single hexagon, is  $(x_i)_{i=1}^{2mn}$  in  $\mathbb{R}^2$ , where  $m$  is the wave number and  $2n + 1$  the index of the

location of each wave, with  $x_i$  and  $x_{i+1}$  depicting neighboring positions (see figure 4.19 (a)). As the graphene lattice consists of indistinguishable hexagons, the distances  $l = |x_{i+1} - x_i|$  between each of them can be assumed as fixed. Furthermore it can be assumed that each hexagon pair forms a certain angle  $\theta$ . The one-dimensional approach of the energy configuration can therefore be written as

$$E(l, \theta) = 2mnk_2(l - l^*)^2 + (2mn - 1)k_3(\theta - \theta^*)^2. \quad (4.1)$$

Here the configuration contains  $2nm$  bonds, forming  $2mn - 1$  angles,  $l^*$  and  $\theta^* \leq \pi$  are the reference distance and angle. The parameter  $k_2 > 0$  arises from the elastic modulus of the in-plane strain and  $k_3 > 0$  from the bending modulus. This model also allows interpreting the response of the structure to external strain and the concomitant change in the bond lengths and angles. To evaluate this, the energy along a chain of hexagons is minimized while applying a mechanical deformation  $s = x_{2mn} - x_1$ . The resulting stretch can be described via trigonometric assumptions

$$s = 2ml \frac{\sin(n(\pi - \theta)/2)}{\tan(n(\pi - \theta)/2)}. \quad (4.2)$$

Figure 4.19 (b) depicts the behavior of the normalized optimal strain  $(l - l^*/l^*)$  as a function of the normalized stretching  $s/s^*$  and  $\theta = \theta^*$  with a normalization such that  $(l - l^*/l^*) = 0$  and  $s/s^* = 1$ . Figure 4.19 (c) on the shows the optimal angle  $\theta$  as a function of  $s/s^*$ . The different plots in figure 4.19 (b) and (c) show the dependence on the choice of parameters. In the first set of simulations, the green graphs in figure 4.19 (b) and (c)  $\theta^* = \pi(2n - 1)/(2n)$ . This assumption describes waves with a wavelength/amplitude aspect ratio of 10 : 1, causing small mechanical strains ( $s/s^* > 1$ ) to promote flattening of waves. This leads to a value for  $(l - l^*/l^*)$  to be close to zero and a monotonously increasing  $s/s^*$ . However, this behavior could not be observed in the following experiments.

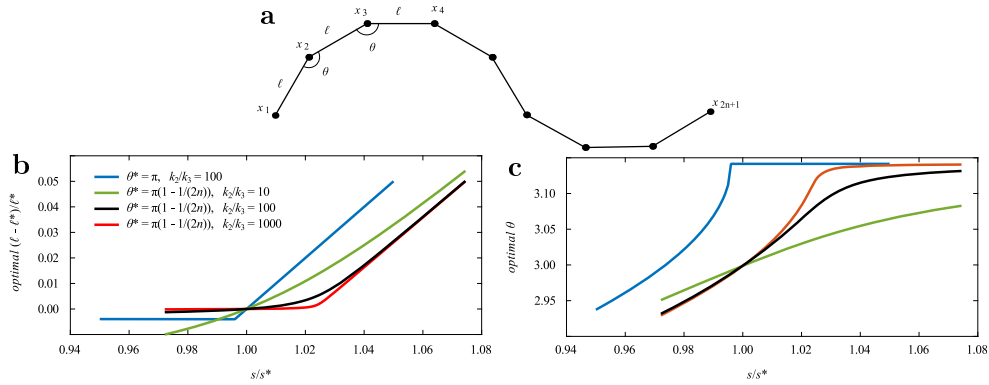


Figure 4.19: **Analytical model for a corrugated wave of locations.**

(a) An elementary wave consisting of  $2n + 1$  locations (corresponding to hexagons in graphene). (b) Optimal (energy minimizing) strain  $\varepsilon = (l - l^*)/l^*$  in the chain as a function of applied stretching  $s/s^*$ . (c) Optimal (energy minimizing) corrugation angle  $\theta$  as a function of applied stretching. For all simulations,  $n = 11, m = 1$  and  $l^* = 1$ .

Further increasing the external strain leads to flattening of the observed hexagon chain ( $\theta$  approaches  $\pi$ , figure 4.19 (c)). Concomitant the bond length of the hexagons increases, leading to a linear behavior. The ratio  $k_2/k_3$  describes the stiffness of the structure (straining vs. bending for a single hexagon chain). The red and blue graphs show the behavior after steadily increasing the ratio of  $k_2/k_3$ . The graphs show a limiting piecewise affine relation. The transition points are reached at the previously mentioned ratio values  $(l - l^*)/l^* = 0$  and  $s/s^* = 1$ . A ratio of  $k_2/k_3 = 100$  agrees best with the experimental results.

The case  $\theta = \pi$  describes buckling of the observed hexagonal chain under external compression. For small compressions the bond lengths decrease without effecting  $\theta = \pi$  and the chain remains flat. Increasing the compression causes an abrupt buckling of the chain with a sudden change in  $\theta$ . This change leads to a deformation of the bonds (in this case to an elongation). This could not be observed in the experiments. Therefore it is suggested to chose the reference angle  $\theta^*$  as strictly smaller than  $\pi$ , indicating a non-flat hexagonal configuration of graphene.

## Simulations of corrugated 2D materials under uniaxial strain

As described above, simulations were used to link the broadening of the diffraction spots with the mean inclination  $\gamma_{RMS}$  of the membrane (figure 4.20 (a) - (b)). As well for these experiments the diffraction pattern were compared to atomistic simulations of the structure (figure 4.20 (e,f)). The created model samples contain 24,000 carbon atoms. The sample was heated up for 5 ns to 6 K, subsequently cooled down for 8 ns to 0.1 K. To simulate one-dimensional strain it was then partially relaxed. From these graphene models diffraction pattern were calculated, again using LAMMPS. The carbon - carbon interactions where, as in the previous experiment, described via the LCBOP potential. Figure 4.20 (e) shows such a structure in the untilted case and (f) at 21° specimen tilt. To allow direct comparison to the experiments, the applied strain is uniaxial.

## Sample preparation for straining TEM holder

It might be worth to mention that the straining holder shown in section 3.2 in figure 3.7 itself already has scarcity value as it was manufactured in 1969. It has a properly working screw drive with an accuracy of 0.05  $\mu\text{m}$ . However, to actually strain a standard TEM grid the specimen needs to be adapted to the device.

The used graphene samples are commercially available graphene membranes on gold TEM grids with an amorphous carbon support film. Other materials were prepared as described above. The grids with the attached 2D films were subsequently transferred on two aluminum platelets with dimensions of  $3 \times 5 \times 0.3 \text{ mm}^3$  size. The gap between the platelets was 300  $\mu\text{m}$ . Each of the platelets has a hole of 1.05 mm in diameter to mount the whole ensemble onto the straining holder shown in figure 3.7. To maintain the needed distances on the ensemble an aluminum mounting stage was built. To fix the grids on the platelets a two-components vacuum compatible epoxy was used. Hardening the applied epoxy takes 30 min on a heating plate at 180 °C.

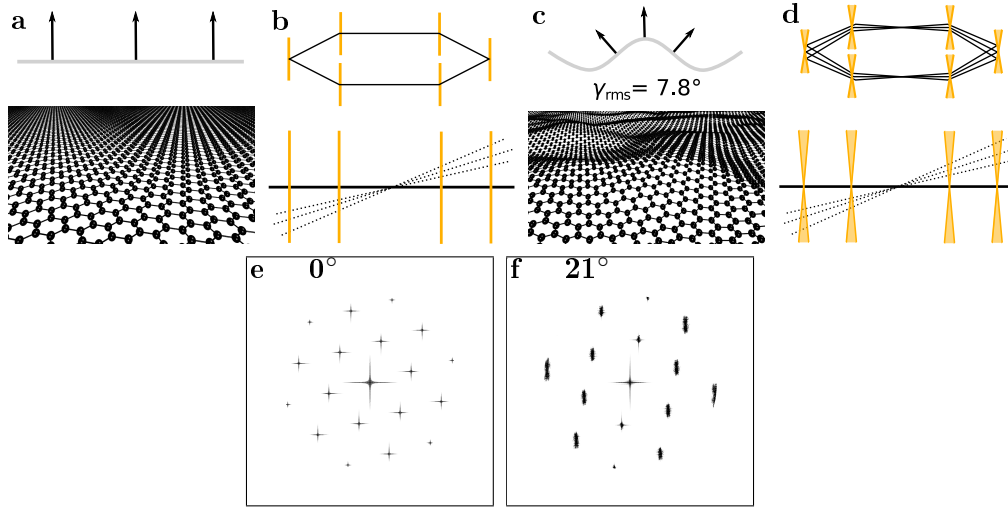


Figure 4.20: **Effect of varying surface inclination on the graphene diffraction pattern.** Flat sample has parallel lattice normals throughout the sample (a), which leads to sharp rods in the reciprocal space (b) giving the same width for diffraction spots regardless of the sample tilt. In contrast, a corrugated sample (c), here with root mean square inclination of  $\gamma_{\text{rms}} = 7.8^\circ$ ) exhibits cone-like volumes in the reciprocal space (d) that lead to increasing diffraction spot sizes for higher sample tilts. (e) Relationship between the diffraction spot size ( $\sigma$ ) and the sample tilt ( $\alpha$ ) for simulated corrugated graphene structures with varying values of  $\gamma_{\text{rms}}$ . The solid line is a fit to the data points. (e) Diffraction pattern of untilted, strained graphene at  $0^\circ$  and at (f)  $21^\circ$  specimen tilt. The diffraction spots orthogonal to the tilt axis exhibit the strongest elongation in direction of the external strain.

The platelet-grid unit is subsequently mounted on the straining holder. The holder has a fixed hook and a moveable part, where the specimen is mounted via a screw (figure 3.7 (b)). The moveable part has a cable linked to a stepper motor at the part outside of the goniometer. The holder is connected to the control unit of the TEM.

### Straining experiment in an uncorrected TEM

The following experiments were conducted with the Phillips CM200. Unlike for the previous experiments the used specimen were not beforehand investigated at the Nion UltraSTEM, because the commercially available graphene (Graphenea  $\text{\textcircled{R}}$ ) specimen have a suitable coverage of monolayered graphene.

As for the experiments of section 4.4.1, a sample position with one crystalline orientation is needed. As can be easily seen in figure 4.27 (a) and (b), the amount of usable sample area is drastically reduced as large parts are either covered with epoxy or aluminum platelets. For preparation (discussed in detail in section 3.2), either a continuous coverage of the remaining gap or good preparations skills and a steady hand, especially for specimen with less coverage, are necessary. This is especially pertinent for samples with low coverage, as valid for specimen of hBN, MoS<sub>2</sub> and heterostructure, where this further reduces the amount of suitable areas.

Once a good spot of suitable size is found, an initial diffraction pattern tilting series is taken. The minimum requirements to a specimen position are: at least 300 nm in diameter, no folds, such as shown in figure 4.27 (b) (third image from left) and no visible pores or holes should be visible. Pores might cause an early end of the experiment as they are a natural weak point of the material and must be avoided. It is advantageous if the lattice is oriented toward the tilting axis, such that one diffraction spot orthogonal to the tilting axis. Like in the previous experiment the tilting series start at a tilt of 0°. In this experiment the maximum tilt angle was 21°. The initial tilt series was taken without external strain. To possibly see a real space deformation in the course of the experiment, an overview image of the full hole of the amorphous carbon support film was taken at each straining increment. After the first tilting series the strain was increased the first time in the experiment. Increasing the strain with the microscope control units causes the specimen to slightly move. Therefore the stage needed to be adjusted to keep the image of the point of interest in the center. Subsequently, after the strain increment was reached, a diffraction pattern was recorded. Tilt series between 0° and 21° were taken at every third step.

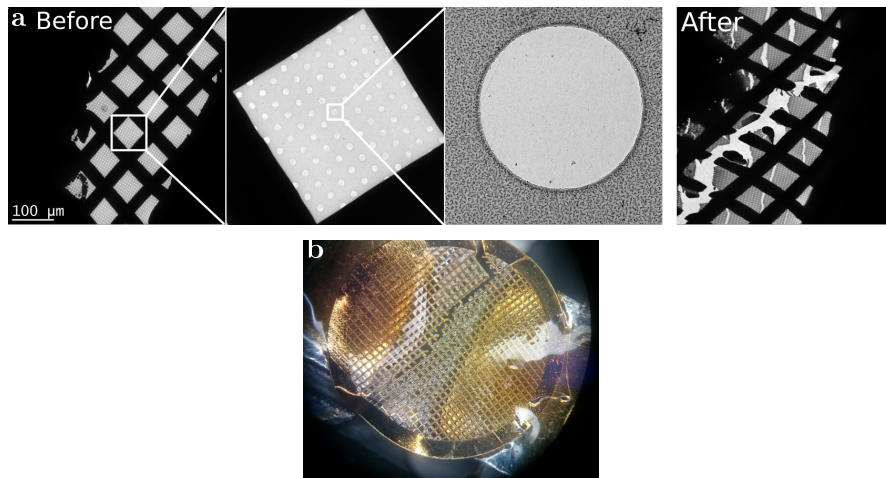


Figure 4.21: **Straining, before and after.** (a) Gap between aluminum platelets in the TEM at low magnification before (left) and after (right) a straining experiment. (b) Image of a broken TEM grid after straining experiment.

The experiment is over when either the graphene membrane and/or the carbon support film breaks, as spectacularly shown in figure 4.27 (a) (rightmost image). The broken grid in figure 4.27 (b) was imaged during one of the test runs for the adapted straining holder. Here the experimental set-up could be tested without the risk of loose parts falling on the pole piece of the objective lens.

### **Analysis of diffraction patterns**

One of the first observations during the straining and tilting series is that with increasing external strain the diffraction spots elongate at increasing specimen tilts. This change is minimal along the tilt axis and reaches its maximum orthogonal to the tilt axis. Figure 4.22 (a) shows the initial, untilted diffraction pattern and (b) the same at a tilt angle of  $21^\circ$ . Figure 4.22 (c) shows the last untilted diffraction pattern and (d) the last diffraction pattern before rupture at  $21^\circ$  specimen tilt. The elongation of the diffraction spots is clearly visible. From its orientation it can be assumed that the deformation occurs along the axis of external strain. Figure 4.26 (a)-(c) gives a more detailed view on

the tilting series at different strain increments. Here only diffraction spots orthogonal to the tilt axis were considered. Figure 4.26 (a) shows broadening of such a spot with an angular increment of  $3^\circ$ . This series is similar to the experiments discussed in section 4.4.1. Figure 4.26 (b) shows broadening of the same spot at an external displacement of  $+0.5 \mu\text{m}$ . Starting from about  $9^\circ$ , an ellipticity of the spot is visible. The last tilting series before rupture was taken at an external displacement of  $+1 \mu\text{m}$  and is shown in Figure 4.26 (c). Here the ellipticity of the spot is pronounced.

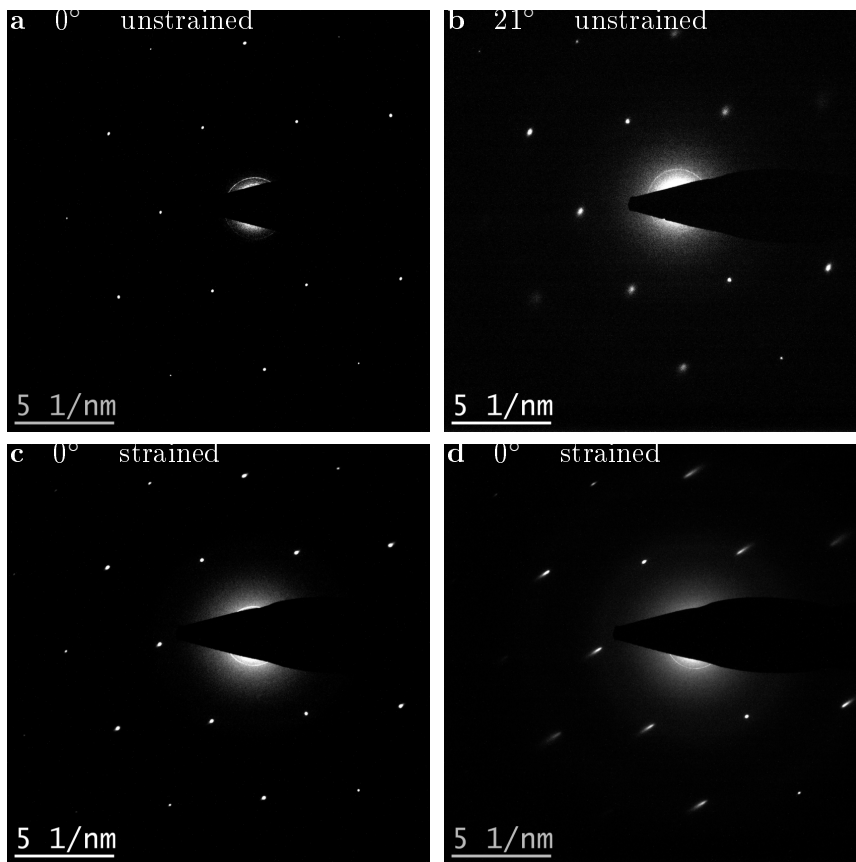


Figure 4.22: **Diffraction pattern of unstrained and strained graphene.** (a) Initial, unstrained and untilted diffraction pattern of graphene and (b) initial, unstrained diffraction patterns of graphene at  $21^\circ$  tilt angle. (c) Untilted and (d) at  $21^\circ$  specimen tilt taken diffraction pattern of graphene of the last tilting series before complete rupture of the material. At this  $21^\circ$  specimen tilt the diffraction spots orthogonal to the tilt axis show strong elongation along this axis.

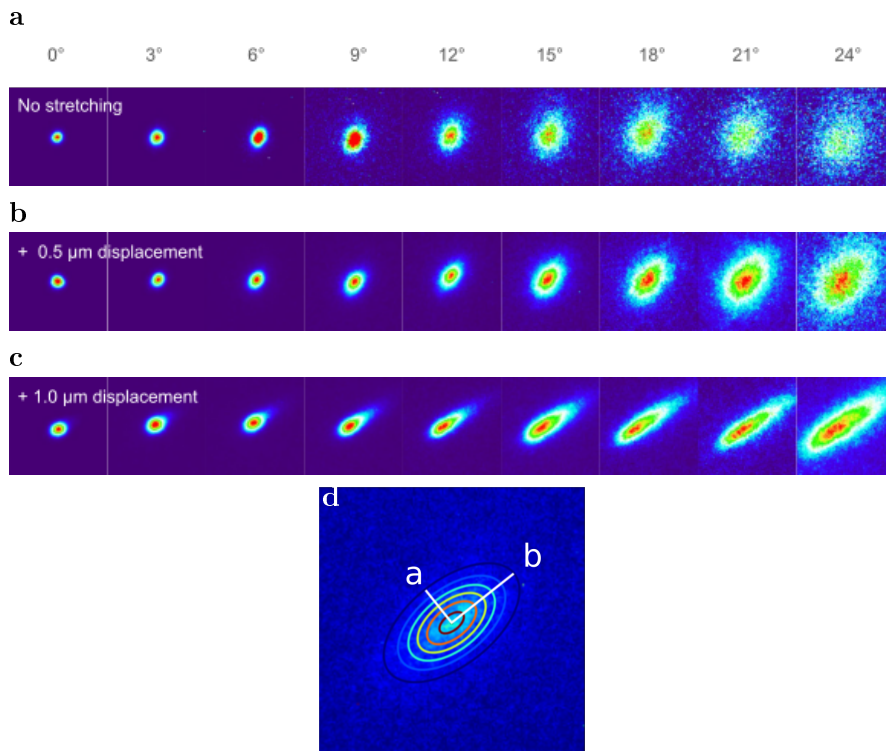


Figure 4.23: **Tilt series for a diffraction spot at different stages of applied strain.** The incremental steps of the tilt angle are  $3^\circ$ . (a) Initial tilt series of the first order diffraction spot, orthogonal to the tilt axis, for unstrained graphene. The diffraction spots stays circular during the tilt series (the ripples are randomly distributed). (b) Tilt series at  $+0.5 \mu\text{m}$  external displacement. The diffraction spot is getting elliptical, as ripples tend to align along the axis of external strain. (c) Last tilt series at  $+1 \mu\text{m}$  external displacement. The diffraction spot is strongly elliptical, the alignment of the ripples is at its maximum value, before the material ruptures. (d) A two-dimensional, asymmetric Gaussian with ellipse axes  $a$  and  $b$  to assess the diffraction spots.

To evaluate the experimental results, a two-dimensional asymmetric Gaussian was taken as a fit function. A typical fit of an elliptical diffraction spot, with the ellipse axis  $a$  and  $b$  is shown in figure 4.23 (d). The two widths  $a$  and  $b$  of the ellipses were evaluated separately and the result of the whole tilt series of the regarded incremental step is shown in figure 4.23 (b). The resulting linear functions have two different slopes, indicating an orientation of the intrinsic corrugations.

This leads to the qualitative conclusion that the structure has been flattened out in the pulling direction during the experiment. Combining the experimental data with the simulated predictions leads to a quantitative statement of how much the structure has been changed. The diffraction patterns have been evaluated as described in section 4.4.1. Here again the diffraction spots with the highest broadening with increasing tilt angle have been investigated. The material broke at the end of the experiment, it is clear that it was strained during the process. In the unstrained case the lattice has a perfect hexagonal symmetry. In case of uniaxially applied strain the hexagons are elongated in the direction of the strain. This small change of interatomic bond lengths in one direction is detectable within the diffraction pattern: if the 2D material gets uniaxially strained, the diffraction pattern changes from a circular shape to a slightly elliptical shape.

## Experimental results

All in all there are several things we can learn from all the ellipticities measured from the diffraction patterns. First among them is the orientation of the ellipses. As shown in figure 4.24 (a) - (c) the diffraction spots rotate with respect to the  $x$ -axis and so does the elliptical diffraction pattern. This is shown in figure 4.24 (d): the blue triangles correspond to the diffraction spots whereas the red dots correspond to the diffraction pattern. The  $x$ -axis shows the orientation in ( $^{\circ}$ ), the  $y$ -axis the relative change in the size of the gap between the aluminum plates. At the end of the experiment ellipses are aligned with each other. It is remarkable that the data spread is the highest for the

diffraction pattern during 2/3 of the experiment. Here the diffraction pattern is still rather circular, which makes it difficult to find the orientation of the ellipse. But in the end as the strain starts to become visible, the elliptical fit becomes unique. This leads to the comparison of the ellipticities over the course of the experiment as shown in figure 4.24 (e). These two independent measurements show an interdependence. This leads to the conclusion that the two separate things (the change on the atomic scale and the change of the intrinsic corrugations) have one common cause: the strain due to the applied relative change in the gap-size.

Figure 4.25 (a) gives an insight into the three-dimensional structure of the 2D membrane changes. The  $y$ -axis is the slope of the linear fit function and the  $x$ -axis corresponds to the relative change in the size of the gap. The downward pointing triangles represent the major axis of the regarded diffraction spot. As the major axis remains basically unaltered during the experiment, it can be assumed that corrugations in this direction remain unperturbed. The minor axis, represented by the upward pointing triangles decreases throughout the experiment. This leads to the conclusion that the corrugations in this direction are getting flattened out. Figure 4.25 (b) represents the interatomic deformation of the material. The  $y$ -axis is the apparent strain  $\epsilon'$  in real space in two orthogonal directions. From the slopes in area (1) and (3) shown in figure 4.25 (b) the Poisson's ratio of graphene can be calculated. The apparent kink in the dataset is a feature found in most experiments and the cause can only be guessed. A plausible cause is braking of parts of the rather rigid amorphous carbon support film, leading to a more direct strain transfer onto the 2D material.

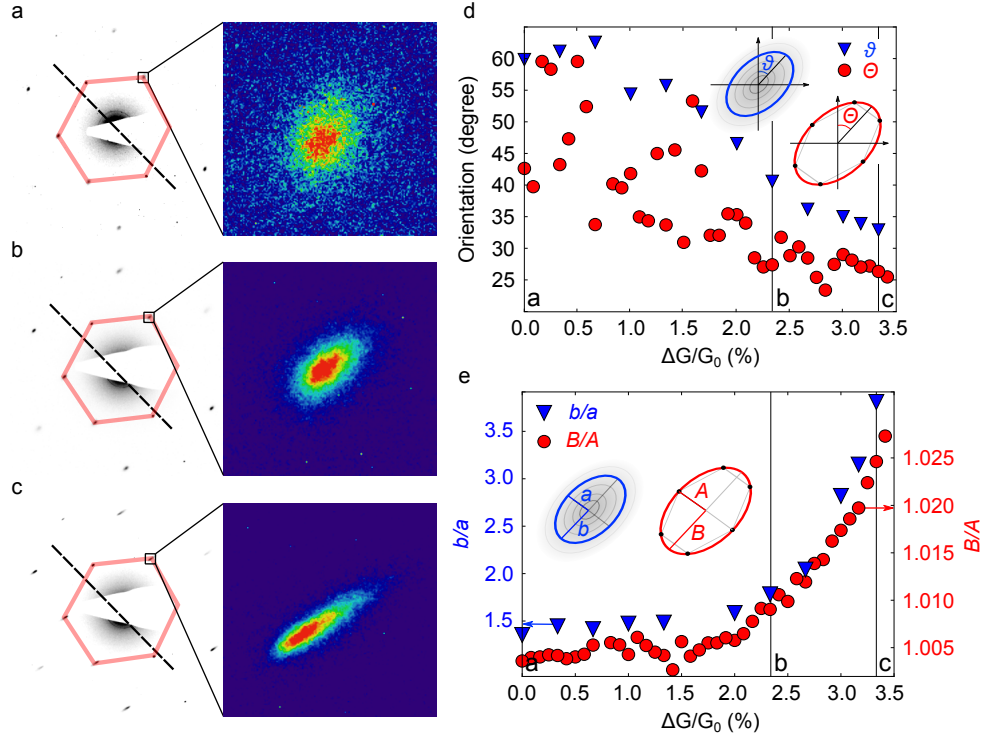


Figure 4.24: **Evolution of the diffraction patterns and individual diffraction spots during the experiment.** (a-c) Diffraction patterns recorded at different stages of the experiment: (a) at the beginning, (b) towards the end and (c) at the end. All shown patterns were recorded at a sample tilt  $\alpha = 21^\circ$ . The dashed lines show the approximate tilt axis and the overlaid hexagons highlight the first set of diffraction peaks. The panels on the right show a zoom-in of the indicated diffraction spots in false color. (d) Orientation of the ellipse fitted to the diffraction patterns ( $\Theta$ ) and that of the diffraction spots ( $\theta$ ) during the experiment. (e) Ellipticity of the diffraction patterns ( $B/A$ , right  $y$ -axis) and spots ( $b/a$ , left  $y$ -axis). Standard deviation from the fits to the measured values are contained within the markers. All diffraction pattern values are for  $\alpha = 0^\circ$  and spot values for  $\alpha = 21^\circ$ . In panels (d) and (e), the values corresponding to the diffraction patterns shown in panels (a-c) are marked with corresponding labels. The  $x$ -axis values ( $\Delta G/G_0$ ) indicate the relative change in the size of the gap in the sample carrier over which the sample was suspended.

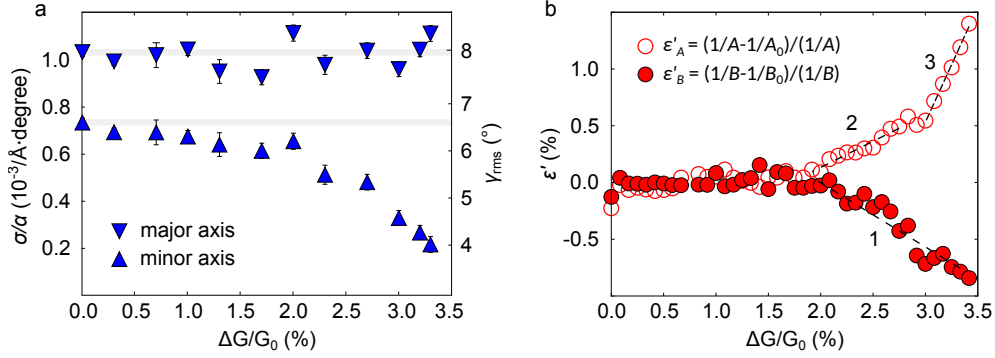


Figure 4.25: **Effect of stretching the sample carrier on the out-of-plane corrugation and strain in suspended graphene.** (a) Changes in the maximum (major axis) and minimum (minor axis) in graphene during the experiment ( $\gamma_{RMS}$ , right  $y$ -axis), as estimated from the  $\sigma/\alpha$  values (left  $y$ -axis) measured from diffraction spots. Error bars show the standard deviation from the fits to the experimental data and horizontal grey lines are guides to the eye. (b) Apparent strain in real space in two orthogonal directions, as estimated from the diffraction patterns at zero tilt ( $\alpha = 0$ ) during the experiment. Initial axes lengths  $A_0$  and  $B_0$  are estimated as the averages of the first fifteen data values for each data set, and the lines marked with labels 1–3 are fits to the corresponding data points with following slopes: (1)  $-0.57 \pm 0.05$ , (2)  $0.46 \pm 0.03$  and (3)  $2.02 \pm 0.09$  (uncertainties are standard errors of the fits). The  $x$ -axis values ( $\Delta G/G_0$ ) indicate the relative change in the size of the gap in the sample holder over which the sample was suspended.

### Pulling MoS<sub>2</sub> and hBN

This experiment was also conducted on MoS<sub>2</sub>, prepared from a CVD grown sample. The samples were prepared in similar manner to those of graphene. For the unstrained specimen an initial tilting series was taken, then the strain was stepwise increased. At every strain step a diffraction pattern of the untilted specimen was recorded and at every fifth strain step a full tilting series. For most of the MoS<sub>2</sub> specimen much higher tilt angles, up to 40°, were possible. A typical example of a straining experiment with MoS<sub>2</sub> is shown in figure 4.26. The analysis of the diffraction pattern included the same processing as for graphene. From diffraction patterns of untilted specimen, atomic displacement could be observed due to elliptical deformation (figure 4.26 (a),

red markers). Similar to the experiments with graphene elliptical deformation of diffraction spots, in the course of the experiments were also observed (figure 4.26 (a), blue markers). However, the observed ellipticities were less pronounced than for the experiments with graphene. As well the orientations of both type of ellipses remained relatively stable during the experiment, except the last data point of the ellipticities of diffraction spots (figure 4.26 (b), blue markers). This spontaneous outlier is caused by the rupture of the material. The intrinsic ripples, which experienced alignment during the experiment changed the orientation when the strain was released due to rupture of the material. Figure 4.26 (c) shows separate evaluation of both ellipse axes of the diffraction spots. In comparison to graphene, it can be observed that towards the end of the experiment the slope in direction of the major axis seems to increase in size. The slope in direction of the minor axis is only fluctuating around the initial value. The right axis of the plot in figure 4.26 (c) shows the corresponding  $\gamma_{rms}$  value. From this figure it appears that the initially flat materials become more corrugated in one direction. Towards the end of the experiment the roughness in two orthogonal directions is different compared to the beginning of the experiment, which is similar to the result for graphene.

By fitting ellipses to untilted diffraction patterns, atomic displacement becomes visible as shown in figure 4.26 (d). Starting at a relative displacement of about  $\Delta G/G_0$  of 3.5% the deviation of the ellipse axis becomes visible. In the plot of  $\epsilon'_B$  an abrupt change is observed. Here the similarities to the graphene experiments can be seen. It is likely that at this point parts of the support ruptured. The last datapoints shown at  $\Delta G/G_0 = 5\%$  indicate the total rupture and release of strain. Figure 4.26 (e) - (h) shows a selection of diffraction patterns of the experiment. The initial diffraction pattern (e) is typical for untilted monolayered MoS<sub>2</sub>, followed by three patterns at 40° tilt. Due to its flatness such high tilts could be reached. Figure 4.26 (g) shows the diffraction pattern at the maximum of relative displacement of  $\Delta G/G_0 = 4\%$  at 40° tilt and (h) the diffraction pattern at the same tilt directly after rupture.

The experiment was also conducted with monolayer hBN. However, due

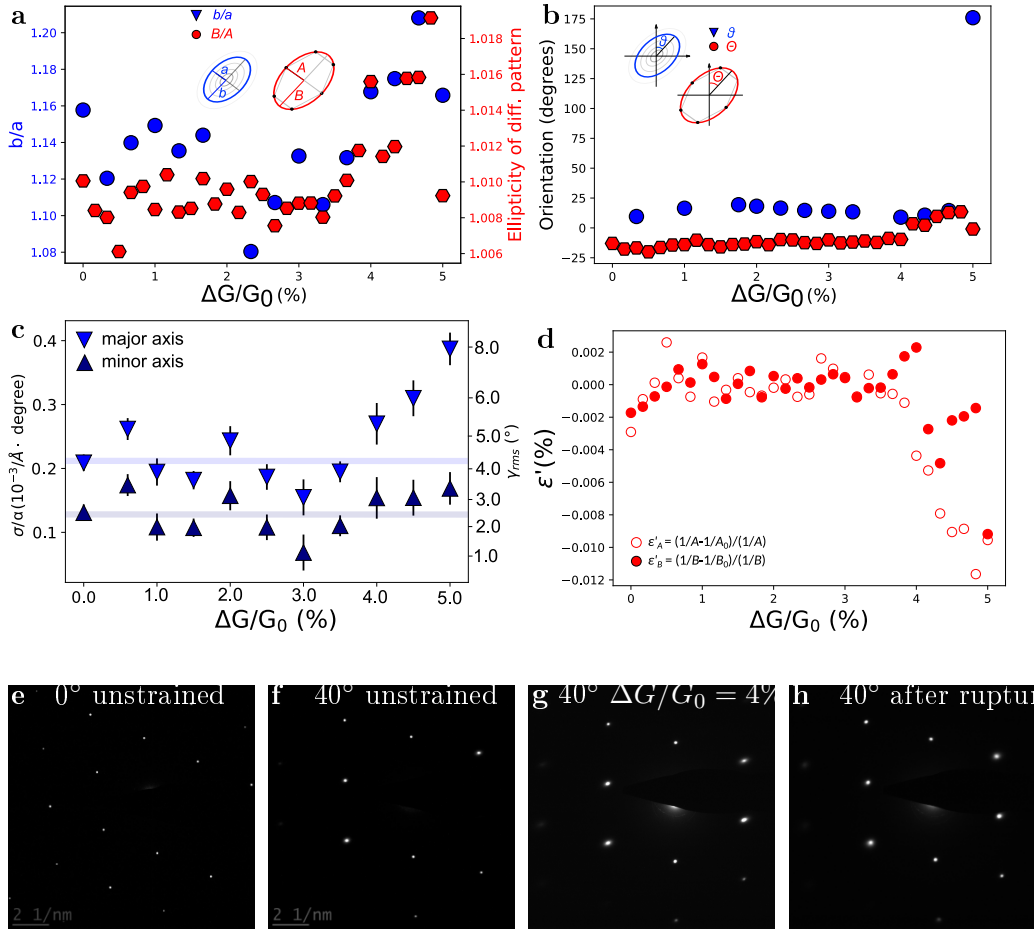


Figure 4.26: **Results of the straining experiment using MoS<sub>2</sub>.** (a) Ratio of the ellipse axes for diffraction spots (blue) at maximum specimen tilt and of untilted diffraction pattern (red). The x-axis shows the course of the experiment as relative displacements  $\Delta G/G_0$ . (b) The orientation of the ellipses of diffraction spots at maximum specimen tilt (blue) and diffraction pattern of the untilted specimen (red). (c) The  $\sigma/\alpha$  values (left y-axis) of the measured diffraction spots in both directions of the ellipses. The right y-axis shows the corresponding  $\gamma$  value. (d) Apparent strain in real space in two orthogonal directions, as measured from the diffraction patterns for untilted specimen.

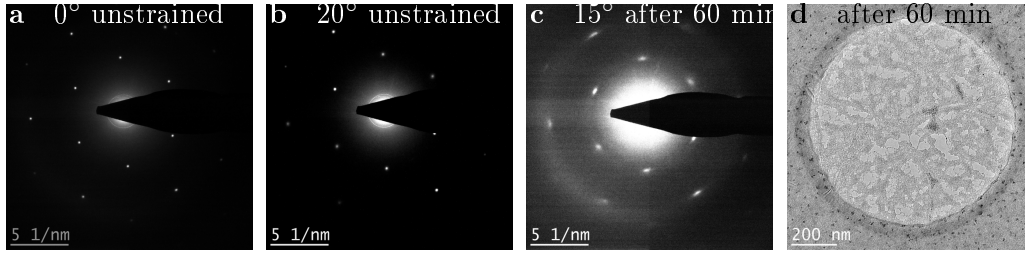


Figure 4.27: **Irradiation damage in hBN.** (a) Initial diffraction pattern at  $0^\circ$  and (b)  $20^\circ$  specimen tilt. (c) Diffraction pattern of hBN after 60 min of electron irradiation at 80 kV, at  $15^\circ$  specimen tilt. (d) The corresponding real space image.

to the irradiation sensitivity of the material, irradiation damage set in rather quickly after the start of the experiments and pores randomly appeared, releasing the strain. The initial diffraction pattern (figure 4.27 (a)) shows a typical pattern for unstrained monolayer hBN, and figure 4.27 (b) of the same structure at  $20^\circ$  specimen tilt. An image after 60 min in the experiment (figure 4.27(d)) shows heavily porous hBN. A diffraction pattern at  $15^\circ$  specimen tilt confirms the presence of strong beam damage. To make the diffraction pattern better visible, the contrast was increased. The initially dot-like diffraction spots were elongated in azimuth direction, but also widened radially. Additionally between the spots in first and second order diffraction events from amorphous structures appear. Due to the immediate beam damage, straining experiments with hBN were therefore not possible.

## 4.6 Defects in graphene

Imaging with high energy electrons causes inevitable damage to the investigated lattice structure. In the following experiments electrons at an accelerating voltage of 200 kV have been used to permanently restructure the graphene lattice into a disordered 2D carbon structure. When single atoms are removed from the lattice, carbon atoms can rearrange around the defective area. These mechanics have been shown by Kotakoski *et al.* [145].

An accelerating voltage of 200 kV is significantly above the knock-on thresh-

old for graphene, which is close to 80 kV [146]. The choice of the acceleration voltage is a trade off between time and damage, as single knock-on also facilitate bond rotations that are crucial for the restructuring. Other types of structurally damaging processes need to be suppressed. Luckily, electrolysis is negligible at these high energies and local charging effects are negligible in the case of graphene [131]. However, chemical etching of graphene is dominant in the following setup and leads to pore generation in the lattice, leading to a complete destruction of the irradiated area [120].

As Eder *et al.* showed in 2014, amorphization of areas in the range of nanometers is possible [147]. The aim of the following experiments was to go beyond the previous studies and to restructure larger areas of graphene, such as a complete graphene-covered hole of a TEM supporting grid ( $\sim 2\mu\text{m}$  in diameter). 200 kV was selected to make this structural transformation within a practical time.

### **Experimental setup to restructure graphene lattices**

The irradiation experiments were conducted in the Phillips CM200. In this instrument the vacuum at the sample is around  $10^{-6}$  torr, which drastically promotes chemical etching compared to ultra high vacuum [120]. To compensate for these processes, heating of the sample was used. This also reduces contamination on the sample. A Gatan heating holder was used for this purpose. In this case, as-prepared TEM gold grid with amorphous, holey carbon foil and industrially produced graphene film (Graphenea) was used. The sample was heated via a metal ring at the tip of the holder. The heating is controlled via an external Gatan controller. The sample was heated up to a temperature of 450 °C. This is sufficiently high to accomplish its purpose and low enough to not require additional water cooling. Heating was started about 30 min before the gun heating, extraction and acceleration voltage was switched on. Due to the elevated temperature, contamination on the specimen is evaporated quickly after switching on the heating. Evaporating the sample contamination usually causes the vacuum to decrease, but is quickly stabilized as the con-

taminant gets trapped at the cooling trap at the specimen holder region of a conventional TEM.

To restructure an area of specific extent on the specimen, in this case a full hole in the amorphous carbon foil, as shown in figure 4.28 (a), the beam has to illuminate the complete area. This was achieved by choosing the largest C1 aperture (2 mm) and setting the illumination via the excitation of the C2 lens, such that the maximum available beam current, at the set acceleration voltage, hit the specimen. The beam was limited to the area of amorphization also in order to estimate the electron dose.

A requirement for the specimen area is that the complete irradiated area is of one crystalline orientation, as grain boundaries could be a limiting factor for restructuring. Likewise, initially present edges or holes as well as folds of the material were avoided. Immediately after finding an area suitable for irradiation, an initial diffraction pattern was recorded. To get the diffraction information of the full non-irradiated illuminated area, a SA aperture of suitable size ( $\sim 2 \mu\text{m}$ ) was chosen. The diffraction patterns were recorded with an Orius SC600A1 camera, with binning 1 and an exposure time of 15 s, through the whole series.

As the CM200 does not offer the possibility of atomically resolved images of graphene, the success of restructuring cannot be directly observed during the irradiation. But even in more modern microscope such as the Titan 80-300(S)TEM changing between rather low magnification,  $3 - 8\text{k}\times$  during the irradiation to high magnification of  $550 \text{ k}\times$  to  $900 \text{ k}\times$  (EFTEM) to obtain lattice resolution in graphene takes time and causes changes of dose rates during the observation. Therefore, the easiest way for controlling the success, without changing illumination parameters, is to monitor the diffraction pattern.

## **Experimental results**

A non-irradiated monocrystalline pristine graphene lattice shows the familiar diffraction pattern as depicted in figure 4.28 (b). Figure 4.28 (a) shows the area intended for irradiation. The selected area is intact, without pores or

grain-boundaries. The spot-like features on the membrane are fixed contamination, which does not change in the course of the experiment, as is visible in figure 4.28 (i). The figure shows the membrane after 135 min of electron irradiation. No major structural damage can be observed neither in the diffraction pattern nor in the real space image.

Diffraction patterns give a measure of the orientation distribution within the lattice. Missing carbon atoms and the following reconstruction leads to a decreasing crystalline order. Changes in crystalline structure cause strain and slight variations in bond-lengths. The former causes spreading of diffraction spots in the azimuthal direction, whereas the latter causes a blurring in the radial direction. These effects increase with irradiation time. It is visible directly from the diffraction pattern that the intensity of the initially sharp diffraction spots decreases, and a ring in azimuthal direction appears.

Even in strongly disordered areas a number of hexagonal rings with the initial lattice orientation remains. The ultimate goal of the experiment is a complete elimination of order and obtaining a completely disordered 2D structure. Figure 4.28 (c) shows the diffraction pattern after an irradiation time of 30 min. As the intensity of the diffraction spots has already decreased significantly, the following diffraction patterns were taken every 15 min (figure 4.28 (d) - (i)). They show the full process of restructuring. Figure 4.28 shows the decrease of intensity for first order spots in the course of the experiment. For equal imaging conditions, the radial intensity distribution was calculated around the diffraction spot.

For all evaluations, the spot along the same lattice plane orientation was chosen. The highest counts are visible for the spot from the initial diffraction spot. Already after 30 min the intensity dropped to less than 50 % of the initial value (red). The maximum intensity value of the same spot after 135 min electron irradiation was at 355 counts, with a background intensity of 100 counts. The amorphized area increases with increasing irradiation time. As this can be directly correlated to the structure of the diffraction pattern, the experiment was stopped after said time. Several attempts for complete

amorphization were made, causing the loss of several specimen due to chemical etching. The irradiated samples were then directly transferred to the Nion ultraSTEM 100 for further investigations. Figure 4.29 shows an example of an irradiation experiment at an accelerating voltage of 200 kV in a Titan 80-300 TEM without in-situ heating. Instead of heating to reduce the effects of chemical etching, a Gatan Solarus II plasma cleaner was used to clean the specimen and specimen holder before the irradiation procedure. Here hydrogen was used as the plasma-producing gas with an exposure time of 50 s. Hydrogen reacts with carbon to produce  $\text{CH}_4$ , the released gas is then pumped by the vacuum pump of the plasma cleaner. Both the BF image in figure 4.29 (b) and the DF image in (c) are taken after the irradiation process. The diffraction spot for taking the DF image (the spot marked with a white circle in figure 4.29 (d)) was also used for the intensity analysis shown in figure 4.29 (g) and (h).

The diffraction pattern shown in figure 4.29 were taken from commercially available CVD grown graphene on a TEM gold grid with holey, amorphous carbon foil (Graphenea). The microscope was aligned and the specimen was set at eucentric height. An initial diffraction pattern was taken in three-condenser settings for a parallel beam with a diameter as large as the size of the freestanding graphene membrane. The advantage of this setup is, that the beam remains unchanged during the change between diffraction mode and imaging mode, as only the excitation of the projector system after the specimen is changed. Every 5 minutes a diffraction pattern was taken over the time span of 110 min. Unfortunately the experiment could not be continued due to unexpected circumstances (failure of the motorized objective aperture), but it shows that by drastically reducing contamination, graphene can endure electron irradiation at 200 kV.

Expectedly the intensity of diffraction spots continuously dropped during the irradiation procedure. Diffraction spots selected for a quantitatively intensity analysis are marked with a white ring in Figure 4.29. Here the diffraction spot was again fitted as described in section 4.3. The resulting maximum intensity was then plotted as a function of irradiation time. In case of agglom-

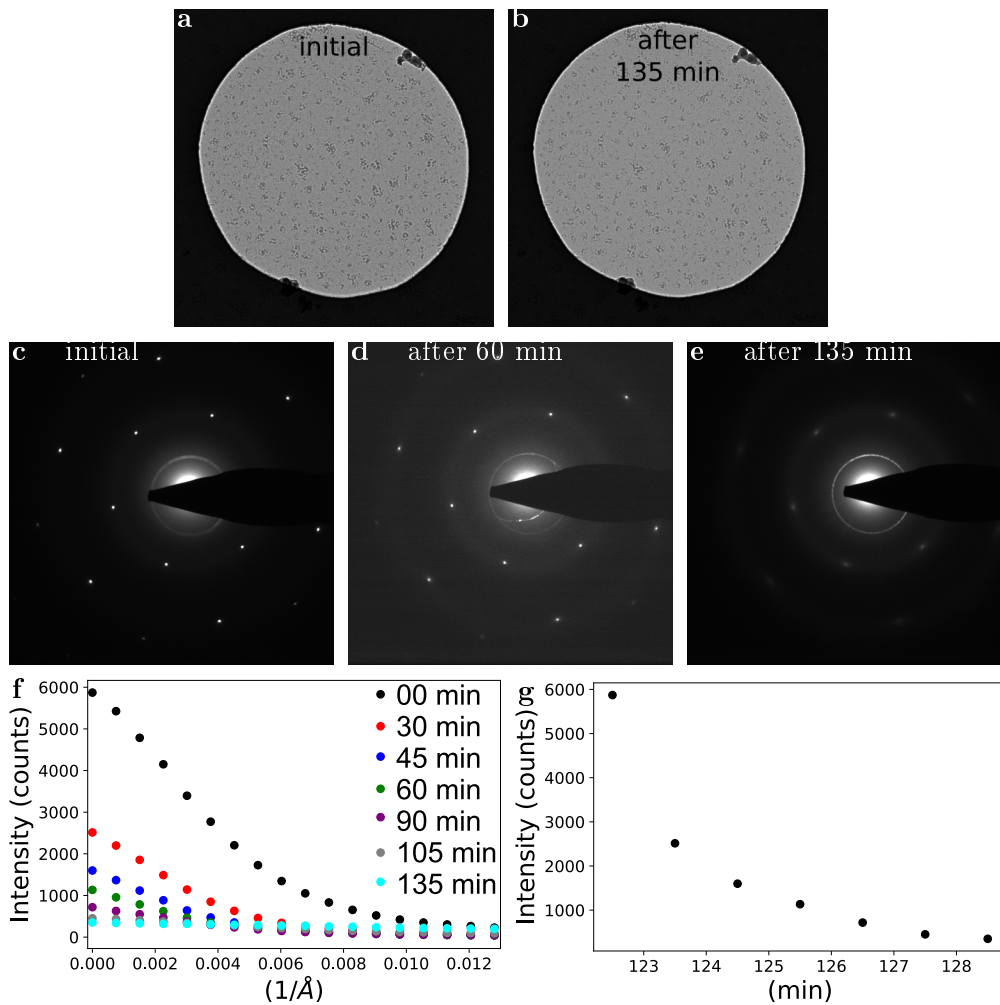


Figure 4.28: **Results of electron irradiation at 200 kV (CM 200).** (a) BF image at 3 k $\times$  of a circular area with a diameter of 2  $\mu\text{m}$  of free-standing graphene. (b) Same after 135 min irradiation with 200 kV. (c) Initial diffraction pattern. (d) Same after 60 min and (e) after 135 min. (f) Radial intensity distribution of diffraction spots. The black dotted curve shows the radial intensity distribution of one spot within the first order spots of the initial diffraction pattern, red after 30 min, blue after 45 min, green after 60 min, purple after 90 min, gray after 105 min and cyan after 135 min. (g) Maximum intensity of diffraction spots as function of irradiation time.

erated contamination it could be argued that the intensity decrease is caused by increasing thickness of the specimen itself. This would have shown a characteristic image, similar to that in figure 4.29 (a), or even more pronounced. However, both the BF as well as the DF image, taken after irradiation do not show structures like that. From this, and the fact that the membrane is intact, it can be assumed that the loss in intensity of the diffraction spot is really due to increasing disorder in the graphene lattice.

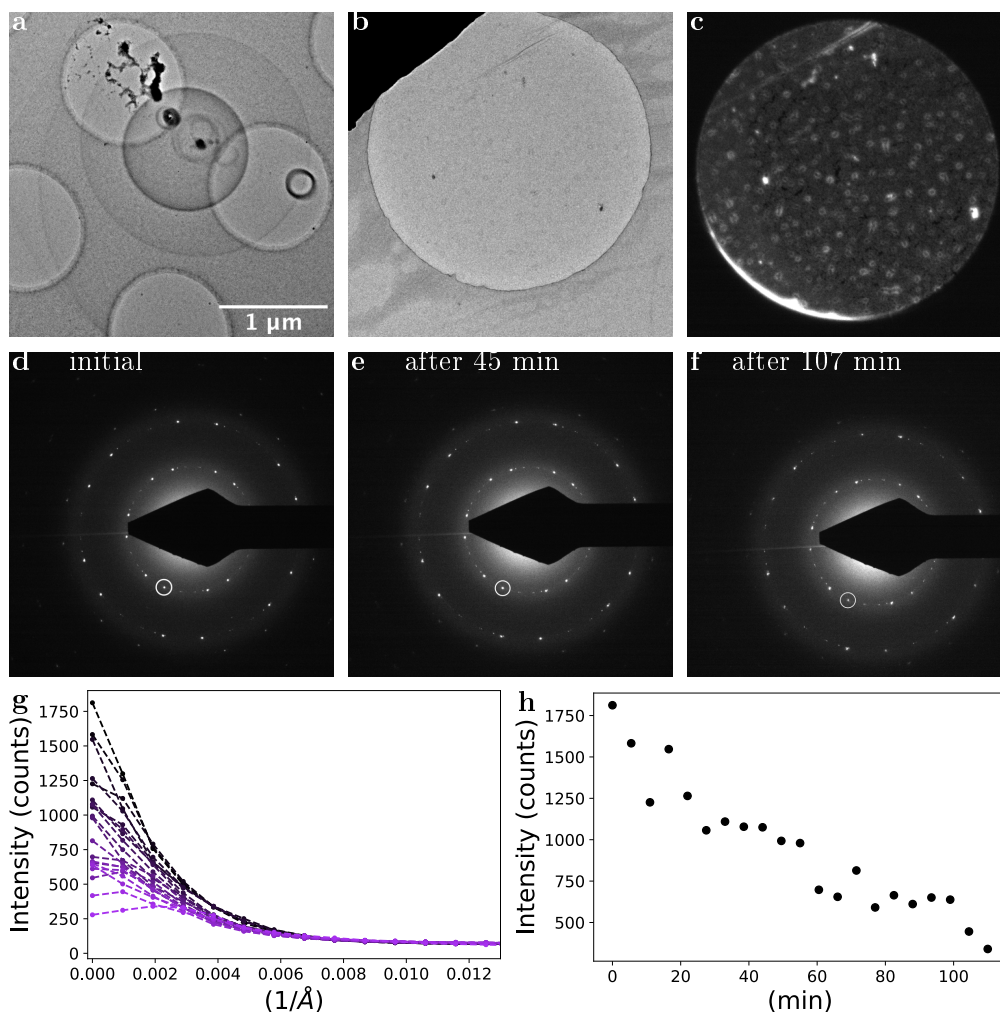


Figure 4.29: **Results of electron irradiation at 200 kV (Titan).** (a) Agglomerated hydro-carbon contamination after 60 min electron irradiation of a contaminating non-plasma cleaned specimen. (b) BF and (c) DF images at 3.4 k $\times$  magnification of a circular area with a diameter of 2  $\mu\text{m}$  of freestanding graphene after 107 min electron irradiation. In both cases no additional contamination is visible. (d) Initial diffraction pattern. (e) Same after 45 min and (f) after 107 min. The white ring mark the diffraction spots for the analysis of the radial intensity distribution. (g) Radial intensity distribution analysis starting with the darkest curve (beginning of the experiment), down to the bright purple curve of the last irradiation step. Every curve describes the radial intensity distribution after additional  $\sim 6$  min. The dashed connecting line serves as guide to the eye. (h) Maximum intensity of the marked diffraction spot as a function of irradiation time.

## Imaging of irradiated graphene structures in the Nion UltraSTEM 100

To avoid further contamination, the specimen-at-air-time was kept as short as possible between experiments with the two instruments. The samples were additionally baked at 150°C before being inserted into the second microscope column. The aim was to investigate specimen with different irradiation times and to correlate subsequently the present defective structures to the irradiation time. Originally, also correlation to Raman spectroscopy was planned. Unfortunately the defective areas are covered in thick layers of fixed carbon contamination, as can be seen in figure 4.30. Some areas were also partially broken as seen in figure 4.30 (a). From this image it can be seen which areas are especially prone for structural failure: Edges such as those of the hole of the amorphous carbon foil, but in other cases also folds. When having a closer look on the non-damaged areas, such as in figure 4.30 (b) areas not covered by contamination show pristine graphene lattice with hints of defective areas as shown in figure 4.30 (d). These images were taken from the specimen presented in figure 4.28.

In conclusion of this experiment, it can be said that according to the resulting structures found in diffraction pattern, disorder was created. Unfortunately the combination of inevitable carbon contamination, insufficient vacuum conditions, defective areas with different binding energies and an ionizing electron beam result in contamination on top of the amorphous areas. This makes a direct interpretation of STEM images and subsequent statistic and analysis of occurring atomic ring numbers impossible at the moment. For further experiments in these directions, a strong emphasis must lie on reducing the hydrocarbon contamination.

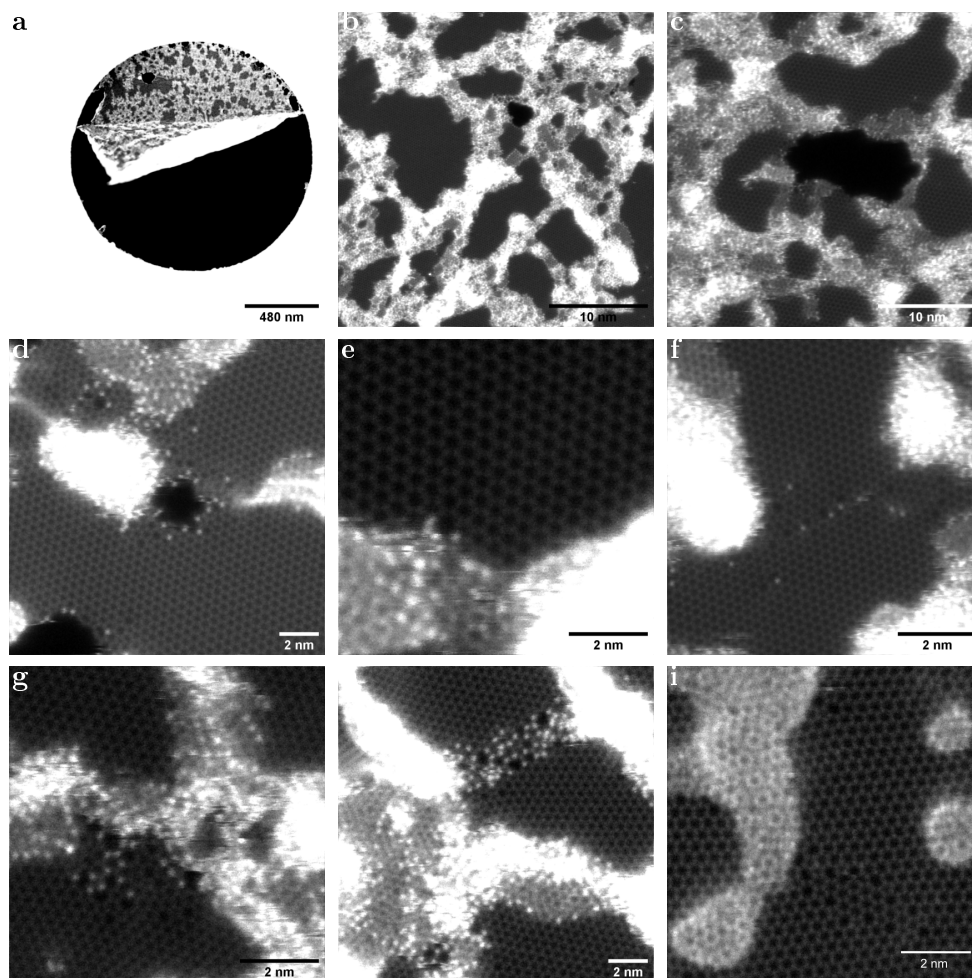


Figure 4.30: **STEM images of irradiated graphene.** (a) Irradiated, partially destroyed graphene membrane. Large areas of contamination (bright contrast) are visible. (b,c) Small pores in the membrane. (d) Atomic resolution image of defective area, including a pore. Si atoms are visible in the defective lattice. (e) Defective areas tend to be covered in contamination. (f) Atomic resolution image of a grain boundary. (g-i) Defective areas, partially covered by contamination.

## Chapter 5

# Conclusion

In this thesis TEM techniques were applied to investigate a variety of low dimensional materials such as graphene, hBN, MoS<sub>2</sub> and carbon nano-onions.

HAADF STEM imaging allows direct interpretation of the composition, especially of 2D materials, as the scattering intensity is proportional to the atomic number. In section 4.1 Si impurities were identified in monolayered hBN solely by their predicted scattering intensities. This method is especially useful in cases of sensitive samples, where spectroscopy methods do not provide sufficient signal to detect them. STEM EELS would have been desirable and could have provided spatial accuracy. In this case the interactions between electron beam and the Si atom in the lattice would have however caused the misplacement of the impurity during the spectrum acquisition. Here the combination with simulation techniques for directly interpreting the nature of the foreign element has been proven useful. The identification of Si was even possible via fast imaging. These fast imaging techniques offered the possibility to observe a pristine structure and ensure that no additional defects were created by the electron beam.

Such direct interpretations are rather applicable in low-dimensional materials such as hBN. For more bulklike materials, especially if containing amorphous regions, additional spectroscopic methods are unavoidable. For potassium intercalated carbon nano-onions, as presented in section 4.2, the presence of

potassium could not be determined by interpreting only the scattering contrasts. Even though MAADF and HAADF imaging showed differences between pristine and intercalated specimen, it could not be concluded that these were caused by potassium intercalation. Here EELS spectrum imaging revealed its presence, even though distinguishing between carbon and potassium using EELS can be challenging. It was assumed that EELS spectra from pristine onions do not vary on different positions of single onions. Taking EELS spectra at multiple locations of pristine onions showed, that the spectra indeed did not differ. They showed a pronounced carbon edge at 248 eV with some fine-structure starting at about 292 eV.

Therefore, in the case of intercalated specimen the presence of potassium was assumed to cause stronger variations at  $L_3 = 294$  eV and  $L_2 = 296$  eV energy loss. For spectrum images energy loss regions were selected to form images. The presence of potassium has no effect on the form or intensity of the  $\pi^*$  peak of carbon, which is the first peak after the onset at 284 eV. Therefore, energy loss images taken in an energy range between 284 – 287 eV was a good reference for the carbon background. Energy loss images taken in an energy range between 294 – 287 eV contained information about potassium. The ratios of images at these regions revealed that potassium was present within the innermost shell of the onions. Here EDX spectra would have given additional insight as the  $K_\alpha$  peaks of both materials have sufficient distance. However, a drawback of this method would have been the lack of spatial resolution.

Here both the in-plane and the out-of-plane structure of 2D materials was investigated using different types of TEM techniques. TEM was used for purely imaging and spectroscopy to study deviations from pristine structures. Apart from imaging, diffraction techniques give further insights into the material properties. Each diffraction spot contains information about the lattice orientation as well as the elemental configuration due to the atomic form factor  $f_a$ . Using image corrected TEM with a spatial and temporal coherent electron source, the intensity of each diffraction spot is largely determined by  $f_a$ . In this study the intensity distribution of diffraction spots for graphene and hBN

could be successfully compared to those obtained through different types of simulation methods.

Electron diffraction techniques can also reveal the true shape of 2D materials. All studied structures (graphene, hBN, MoS<sub>2</sub> and their heterostructures) were shown to exhibit degrees of non-flatness. These differences can be seen by standard parallel beam SA diffraction in the non-corrected TEM with a thermionic electron gun. Changing the experimental setup to a TEM with a gun of higher spatial and temporal coherency and the possibility of aperture-free SA parallel beam diffraction, in combination with a standard CCD, leads to higher accuracy in each data point (diffraction spot). However, this also introduces challenges from the data processing side. Using this experimental setup it is observed that each diffraction spot indeed is a convolution of a Gaussian shaped function coming from the electron source and a specimen response function [115]. The first is largely determined by the spatial coherency of the source. Its contribution can be diminished by choosing a suitable spot-size (excitation of the first condenser lens C1). The evaluation of the specimen response function, especially at high specimen tilts is in this setup highly error prone as inelastic scattering events cause background intensity over a large range of spatial frequencies.

To eliminate these inelastic contributions using an energy filter eases the evaluation of the occasionally rather weak specimen response functions. In such devices an energy selective slit can be placed on an area of certain electron energy loss. By selecting the ZLP, only elastically scattered electrons contribute to the diffraction pattern (if the projector system is set accordingly). This increases the signal-to-noise ratio of the whole diffraction pattern, therefore the specimen response function can be analyzed more easily.

In most experiments MoS<sub>2</sub> appeared relatively flat, except for one dataset. The specimen used for that dataset was previously treated by laser irradiation in order to clean the material. Such treatments cause thinning of the supporting film, which then tend to be prone to vibrations. These vibrations were the likely cause of the observed effect.

For graphene two kinds of samples were studied: CVD grown and mechanically exfoliated graphene. CVD grown graphene exhibited some variations in its non-flatness. For exfoliated samples a flake size dependence seems to be apparent. The first sets of experiments were conducted with rather small graphene flakes with a size range of only a few holes on the carbon support film. Large flakes show a tendency towards waviness. Results for CVD grown hBN were similar to CVD-grown graphene.

For the evaluation of heterostructures the spots corresponding to each material have been analyzed separately. Here the sample preparation plays a crucial role, as was shown for the vdW heterostructure of graphene and hBN, as it can lead to additional rippling of at least one of the membranes. A similar effect is visible for a MoS<sub>2</sub>-graphene heterostructure. As for all heterostructure specimen where CVD-grown graphene was used, a tendency towards more flatness in this material can be observed compared to monolayered membranes.

Taking these results a step further by applying strain results in orientation of intrinsic ripples as well as deformation of the underlying lattice. The most pronounced effect was observed on graphene followed by MoS<sub>2</sub>, where the effects was however less pronounced. For hBN the long exposure to energetic electrons lead to the destruction of the materials.

The experiment could be more refined with an adapted experimental setup by using microelectromechanical systems (MEMS) devices for strain application. Unlike the experiments in this work, the actual applied strain could be measured. As well due to different transfer techniques, the indirect strain transfer by an amorphous carbon film could be avoided. This method could then also be applied to heterostructures. In this case it is very likely that by applying strain on the specimen the lattices of each material misplace with respect to each other. Such changes in lattice mismatches could then be detected in convergent beam electron diffraction (CBED) patterns [148]. This technique would also offer the possibility of CBED strain maps, where a convergent electron beam scans over a specimen area. This step could be repeated for all strain steps until the material breaks. A drawback of this method would

be the long beam exposure. But for accelerating voltages of up to 80 kV the presence of graphene protects non-conductive materials from radiolysis [149].

Knock-on caused removal of carbon atoms from graphene happens due to electron irradiation at sufficiently high acceleration voltages. Here irradiation experiments on micrometer scale were conducted inside a TEM by using electrons with an acceleration voltage of 200 kV. With this method, one atom at a time is removed from the lattice, leading to step-wise restructuring of the lattice from hexagonal structure to a combinations of five-fold to nine-fold rings of carbon atoms. The restructuring of the material can be observed in a parallel beam SA diffraction pattern of the irradiated area. Stopping the electron irradiation immediately stops the transformation process. An obstacle during these experiments was the combination of hydrocarbon contamination and non-UHV conditions causing chemical etching. This results in the loss of a larger number of lattice atoms than by the randomly distributed atom losses caused by knock-on damage. A partial solution was simultaneous heating of the specimen. Subsequent investigations of the irradiated specimen in a STEM showed that defective areas tend to accumulate contamination. A statistical evaluation and correlation of the resulting, disordered graphene structure to the electron dose per irradiation time was therefore not possible.

Overall, the results presented here show that TEM remains a highly relevant technique for the study of low-dimensional materials and their response to external stimuli both in real and reciprocal space.



## Appendix A

- Python code for evaluation of diffraction pattern

```

"""
Created on Fri Nov 25 11:35:13 2016
"""
import tifffile
import glob, os
import numpy as np
import matplotlib.image as mpimg
from numpy.linalg import eig, inv
import scipy
from pylab import *
import scipy.optimize as opt
import pylab as plt
import matplotlib.patches as patches
import scipy.ndimage as ndimage
import scipy.ndimage.filters as filters

def read_img(img_file):
    img = tifffile.imread(img_file)
    return img

def read_peaklist(file, x_scalingfactor, y_scalingfactor):
    peaklist = np.loadtxt(file)
    return peaklist

def _fit_2d_curve(x,y, A, x0, y0, s1, s2 , offset):
    return A*np.exp(- ((x-x0)**2/(2*s1**2) + (y-y0)**2/(2*s2**2)))

def close_event():
    plt.close()

#####
# Rotation of spots
#####

def raw_moment(data, iord, jord):
    nrows, ncols = data.shape
    y, x = np.mgrid[:nrows, :ncols]
    data = data * x**iord * y**jord
    return data.sum()

def inertial_axis(data):
    """Calculate the x-mean, y-mean, and cov matrix of an image."""
    data_sum = data.sum()
    m10 = raw_moment(data, 1, 0)
    m01 = raw_moment(data, 0, 1)
    x_bar = m10 / data_sum
    y_bar = m01 / data_sum
    u11 = (raw_moment(data, 1, 1) - x_bar * m01) / data_sum
    u20 = (raw_moment(data, 2, 0) - x_bar * m10) / data_sum
    u02 = (raw_moment(data, 0, 2) - y_bar * m01) / data_sum
    cov = np.array([[u20, u11], [u11, u02]])
    return x_bar, y_bar, cov

def get_orientation(x_bar, y_bar, cov):
    """Plot bars with a length of 2 stddev along the principal axes."""
    def get_points(eigvals, eigvecs, mean, i):
        """Make lines a length of 2 stddev."""
        std = np.sqrt(eigvals[i])
        vec = 2 * std * eigvecs[:,i] / np.hypot(*eigvecs[:,i])
        x, y = np.vstack((mean-vec, mean, mean+vec)).T
        return x,y
    mean = np.array([x_bar, y_bar])

```

```

eigvals, eigvecs = np.linalg.eigh(cov)
axis1=get_points(eigvals, eigvecs, mean, -1)
Theta = np.arctan((axis1[1][1]-axis1[1][0])/(axis1[0][1] - axis1[1]
[0]))#*180/np.pi
return Theta

```

```

#####
# 2 d Gaussian Fit
#####

```

```

def gaussian2D(height, center_x, center_y, width_x , width_y, Theta):

```

```

    """Returns a gaussian function with the given parameters"""

```

```

    width_x = float(width_x)

```

```

    width_y = float(width_y)

```

```

    return lambda x, y:(height)*exp(-((np.cos(Theta)**2/(2*width_x**2)
+ np.sin(Theta)**2/(2*width_y**2))
*(center_x-x)**2-2*(-np.sin(2*Theta)
/(4*width_x**2)+np.sin(2*Theta)
/(4*width_y**2))*(center_x -x)*(center_y-y)
+( np.sin(Theta)**2/(2*width_x**2)
+np.cos(Theta)**2/(2*width_y**2))
*(center_y-y)**2)) #(height)*exp(-
(((center_x-x)/width_x)**2+((center_y-y)/width_y)**2)/2)

```

```

def gaussian2Dsym(height, center_x, center_y, width_x):

```

```

    """Returns a symmetric gaussian function with the given parameters"""

```

```

    width_x = float(width_x)

```

```

    return lambda x, y: (height)*exp(-(((center_x-x)/width_x)**2+((center_y-
y)/width_x)**2)/2)

```

```

def moments(data):

```

```

    """

```

```

    Returns (height, x, y, width_x, width_y)
    the gaussian parameters of a 2D distribution by calculating its
    moments

```

```

    """

```

```

    ''' New center - with maximum finder '''

```

```

    total = data.sum()

```

```

    Y, X = indices(data.shape)

```

```

    x = (X*data).sum()/total

```

```

    y = (Y*data).sum()/total

```

```

    xbar, ybar, cov = inertial_axis(data)

```

```

    Theta =get_orientation(xbar, ybar, cov)

```

```

    col = data[:, int(y)]

```

```

    width_x = sqrt(abs((arange(col.size)-x)**2*col).sum()/col.sum())

```

```

    row = data[int(x), :]

```

```

    width_y = sqrt(abs((arange(row.size)-y)**2*row).sum()/row.sum())

```

```

    height = data.max()

```

```

    return height, x, y, width_x, width_y, Theta

```

```

def moments_s(data):

```

```

    """

```

```

    Returns (height, x, y, width_x)

```

```

    the gaussian parameters of a 2D distribution by calculating its
    moments

```

```

    """

```

```

total = data.sum()
Y, X = indices(data.shape)
x = (X*data).sum()/total
y = (Y*data).sum()/total

col = data[:, int(y)]
width_x = sqrt(abs((arange(col.size)-x)**2*col).sum()/col.sum())
height = data.max()
return height, x, y, width_x

def fitgaussian2D(data):
    """Returns (height, bgrd, x, y, width_x, width_y)
    the gaussian parameters of a 2D distribution found by a fit"""

    params = moments(data)

    errorfunc = lambda p: ravel(gaussian2D(*p)(*indices(data.shape)) - data)
    p, success = opt.leastsq(errorfunc, params,col_deriv =1,
                             ftol =1e-08, xtol = 1e-08)

    return p

def fitgaussian2D_s(data):
    """Returns (height, bgrd, x, y, width_x, width_y)
    the gaussian parameters of a 2D distribution found by a fit"""

    params_s = moments_s(data)
    errorfunc_sym = lambda p_s: ravel(gaussian2Ds sym(*p_s)(*indices(data.shape))
    - data)
    p_s, success_s= opt.leastsq(errorfunc_sym, params_s,col_deriv =1,
                                 ftol =1e-08, xtol = 1e-08)

    return p_s

#####
#   Defining a function to fit the spots
#####

def fit_function(peaklist, img, boxlength, counter):
    position_list = []
    widths = []
    heightlist = []
    widths_s = []
    heightlist_s = []
    position_list_s = []
    k = 0
    fig1, ax1 = plt.subplots(1,len(peaklist),frameon=False, figsize=(15, 7),
                             facecolor='w', edgecolor='k')

    for i in peaklist:
        x, y = int(i[0]+0.5), int(i[1]+0.5)
        crop_img = img[y-boxlength:y+boxlength, x-boxlength:x+boxlength]

        ny, nx = crop_img.shape
        ix, iy = np.meshgrid(np.arange(nx), np.arange(ny))
        distance = (ix - boxlength)**2 + (iy - boxlength)**2
        r1 = 20.0
        r2 = 30.0
        Iout = np.ma.masked_where(distance > r2**2, crop_img)
        Iin = np.ma.masked_where(distance > r1**2, crop_img)
        bgr = (np.sum(Iout)-np.sum(Iin))/(Iout.count() - Iin.count())
        print(np.sum(Iout),np.sum(Iin))
        fig = plt.figure()

```

```

plt.imshow(Iout)
circ1 =plt.Circle((30,30),20, color='red', fill=False, linewidth =5)
circ2 =plt.Circle((30,30),30, color='red', fill=False, linewidth =5)

fig.add_subplot(111).add_artist(circ1)
fig.add_subplot(111).add_artist(circ2)
plt.savefig('spot.svg')
Int_spot = np.mean(Iin - bgr)

```

```

print('INTENSITY',Int_spot)
position_list.append((x,y,Int_spot,bgr))

```

```

diffp = open('diffpoints_%.dat'%str(filename[:9]), 'a')
header = ['X (px)', 'Y (px)', 'Intensity (I*px*px)', 'BGR']
diffp.write('\t'.join(header) + '\n')
diffp.write('\n'.join('%s\t %s\t %s\t %s' % item for item in position_list))
diffp.close()

```

```

return(position_list)

```

```

#####
# Masking area
#####

```

```

def masked(filename,data, mask_radius1, mask_radius2, center_x, center_y):
    ny, nx = data.shape
    ix, iy = np.meshgrid(np.arange(nx), np.arange(ny))
    distance = (ix - center_x)**2 + (iy - center_y)**2

    mask = np.ma.masked_where(distance < mask_radius1, data)
    mask = np.ma.masked_where(distance > mask_radius2, mask)
    plt.figure()
    plt.imshow(mask, cmap = 'hot', clim = (2,300))
    plt.title('%s' %(filename), fontsize = 30)
    peaklist = peaks(mask)
    return peaklist

```

```

#####
# Find peaks and sort them by their intensity value
#####

```

```

def peaks(data):
    ''' Looking for local maxima in the masked image '''

    neighborhood_size = 100
    threshold = 10
    peaks = []
    data_max = filters.maximum_filter(data, neighborhood_size)
    maxima = (data == data_max)
    data_min = filters.minimum_filter(data, neighborhood_size)
    diff = ((data_max - data_min) > threshold)
    maxima[diff == 0] = 0
    labeled, num_objects = ndimage.label(maxima)
    slices = ndimage.find_objects(labeled)
    x_m, y_m = [], []
    for dy,dx in slices:
        x_center = (dx.start + dx.stop - 1)/2
        x_m.append(x_center)
        y_center = (dy.start + dy.stop - 1)/2
        y_m.append(y_center)
        peaks.append((x_center, y_center))
    plt.scatter(x_m,y_m)
    return peaks

```

```

#####
# Find hexagons
#####

def find_hexagon(self, peaks_sorted, center):
    angle_tolerance = self.angle_tolerance/180*np.pi
    removed_peak = True
    while removed_peak:
        removed_peak = False
        hexagon = []
        peaks_added = []
        for i in range(0, len(peaks_sorted)):
            peak1 = peaks_sorted[i-2]
            peak2 = peaks_sorted[i-1]
            peak3 = peaks_sorted[i]
            edge1 = peak1 - peak2
            edge2 = peak3 - peak2
            lengths = [np.sqrt(np.sum((edge1)**2)), np.sqrt(np.sum((edge2)**2))]
            angle = np.arccos(np.dot(edge1, edge2)/(np.product(lengths)))
            radii = [np.sqrt(np.sum((peak1 - center)**2)),
                    np.sqrt(np.sum((peak2 - center)**2)),
                    np.sqrt(np.sum((peak3 - center)**2))]
            #print(peak1, lengths, angle*180/np.pi)
            if (np.abs(lengths[0] - lengths[1]) <
                self.length_tolerance*np.mean(lengths) and
                np.abs(angle - 2*np.pi/3) < angle_tolerance):
                peak_index = i-2 if i-2 >= 0 else len(peaks_sorted) + (i-2)
                if np.abs(radii[0] - np.mean(radii[1:])) >
                    self.length_tolerance*np.mean(radii):
                    peaks_sorted.pop(peak_index)
                    removed_peak = True
                    break
                elif not peak_index in peaks_added:
                    hexagon.append(peak1)
                    peaks_added.append(peak_index)
                    peak_index = i-1 if i-1 >= 0 else len(peaks_sorted) + (i-1)
                    if np.abs(radii[1] - np.mean((radii[0], radii[2]))) >
                        self.length_tolerance*np.mean(radii):
                    peaks_sorted.pop(peak_index)
                    removed_peak = True
                    break
                elif not peak_index in peaks_added:
                    hexagon.append(peak2)
                    peaks_added.append(peak_index)
                    peak_index = i if i >= 0 else len(peaks_sorted) + i
                    if np.abs(radii[2] - np.mean(radii[:-1])) >
                        self.length_tolerance*np.mean(radii):
                    peaks_sorted.pop(peak_index)
                    removed_peak = True
                    break
                elif not peak_index in peaks_added:
                    hexagon.append(peak3)
                    peaks_added.append(peak_index)
        return hexagon

#####
# Main
#####

if __name__ == '__main__':
    crop_array = []
    #widths = []
    h_flag = True

```

```

if h_flag == True:
    h_flag = False

    FWHM= open('FWHM.dat', 'a')
    header = ['STEP', 'TILTANGLE', 'DIST', 'WIDTH', 'X', 'Y', 'ANGLE']
    FWHM.write('\t'.join(header) + '\n')
    FWHM.close()
for filename in sorted(glob.glob('*.tif'), key = lambda x: (x.split('f')
[0]))):
    print(filename)
    img = read_img(filename)

    if float(filename[4:5]) < 30 :
        print('<30:', float(filename[4:5]) )
        boxlength = 30
        center_x = len(img)*0.45
        center_y = len(img)*0.45

        mask_radius1 = 160**2
        mask_radius2 = 900**2

    img_blur = scipy.ndimage.filters.gaussian_filter(img, 20)
    peaklist = masked(filename, img_blur, mask_radius1, mask_radius2,
                    center_x, center_y)

    fit_function(peaklist, img, boxlength, counter=0)
    plt.show()
    plt.pause(3)

```



# Bibliography

- [1] O. V. Yazyev and Y. P. Chen, “Polycrystalline graphene and other two-dimensional materials,” *Nature Nanotechnology*, vol. 9, no. 10, pp. 755–767, 2014.
- [2] N. D. Mermin, “Crystalline order in two dimensions,” *Physical Review*, vol. 176, no. 1, pp. 250–254, 1968.
- [3] R. Peierls, “Quelques propriétés typiques des corps solides,” *Annales de l’I.H.P.*, vol. 5, no. 3, pp. 177–222, 1935.
- [4] L. D. Landau, “Soviet Physics Uspekhi - From the history of physics,” *Phys. Z. Sowjeunion*, vol. 11, pp. 26–35, 1937.
- [5] H. Wang, F. Liu, W. Fu, Z. Fang, W. Zhou, and Z. Liu, “Two-dimensional heterostructures: fabrication, characterization, and application,” *Nanoscale*, vol. 6, no. 21, pp. 12250–12272, 2014.
- [6] K. S. Novoselov, A. K. Geim, S. V. Morozov, D. Jiang, Y. Zhang, S. V. Dubonos, I. V. Grigorieva, and A. A. Firsov, “Electric field effect in atomically thin carbon films,” *Science*, vol. 306, no. 5696, 2004.
- [7] J. C. Meyer, A. K. Geim, M. I. Katsnelson, K. S. Novoselov, T. J. Booth, and S. Roth, “The structure of suspended graphene sheets,” *Nature*, vol. 446, pp. 60–63, Mar. 2007.
- [8] I. Janowska, F. Vigneron, D. Bégin, O. Ersen, P. Bernhardt, T. Romero, M. J. Ledoux, and C. Pham-Huu, “Mechanical thinning to make few-

- layer graphene from pencil lead,” *Carbon*, vol. 50, no. 8, pp. 3106–3110, 2012.
- [9] A. H. C. Neto and K. Novoselov, “Two-dimensional crystals: beyond graphene,” *Materials Express*, vol. 1, no. 1, pp. 10–17, 2011.
- [10] N. W. Ashcroft and N. D. Mermin, *Solid State Physics*. HRW international editions, Holt, Rinehart and Winston, 2012.
- [11] K. Zhang, Y. Feng, F. Wang, Z. Yang, and J. Wang, “Two dimensional hexagonal boron nitride (2D-hBN): Synthesis, properties and applications,” *Journal of Materials Chemistry C*, vol. 5, no. 46, pp. 11992–12022, 2017.
- [12] K. F. Mak, C. Lee, J. Hone, J. Shan, and T. F. Heinz, “Atomically thin MoS<sub>2</sub>: A new direct-gap semiconductor,” *Physical Review Letters*, vol. 105, no. 136805, pp. 1–4, 2010.
- [13] M. Iliut, C. Silva, S. Herrick, M. McGlothlin, and A. Vijayaraghavan, “Graphene and water-based elastomers thin-film composites by dip-moulding,” *Carbon*, vol. 106, pp. 228–232, 2016.
- [14] Q. H. Wang, K. Kalantar-Zadeh, A. Kis, J. N. Coleman, and M. S. Strano, “Electronics and optoelectronics of two-dimensional transition metal dichalcogenides,” *Nature Nanotechnology*, vol. 7, no. 11, pp. 699–712, 2012.
- [15] A. Splendiani, L. Sun, Y. Zhang, T. Li, J. Kim, C. Y. Chim, G. Galli, and F. Wang, “Emerging photoluminescence in monolayer MoS<sub>2</sub>,” *Nano Letters*, vol. 10, no. 4, pp. 1271–1275, 2010.
- [16] T. H. Han, H. Kim, S. J. Kwon, and T. W. Lee, “Graphene-based flexible electronic devices,” *Materials Science and Engineering R: Reports*, vol. 118, pp. 1–43, 2017.

- [17] C. Brand, M. Sclafani, C. Knobloch, Y. Lilach, T. Juffmann, J. Kotakoski, C. Mangler, A. Winter, A. Turchanin, J. Meyer, O. Cheshnovsky, and M. Arndt, “An atomically thin matter-wave beamsplitter,” *Nature Nanotechnology*, vol. 10, 2015.
- [18] J. S. Bunch, S. S. Verbridge, J. S. Alden, A. M. Van Der Zande, J. M. Parpia, H. G. Craighead, and P. L. McEuen, “Impermeable atomic membranes from graphene sheets,” *Nano Letters*, vol. 8, no. 8, pp. 2458–2462, 2008.
- [19] S. Hu, M. Lozada-Hidalgo, F. C. Wang, A. Mishchenko, F. Schedin, R. R. Nair, E. W. Hill, D. W. Boukhvalov, M. I. Katsnelson, R. A. W. Dryfe, I. V. Grigorieva, H. A. Wu, and A. K. Geim, “Proton transport through one-atom-thick crystals,” *Nature*, vol. 516, pp. 227–230, dec 2014.
- [20] M. Lozada-Hidalgo, S. Hu, O. Marshall, A. Mishchenko, A. N. Grigorenko, R. A. W. Dryfe, B. Radha, I. V. Grigorieva, and A. K. Geim, “Sieving hydrogen isotopes through two-dimensional crystals,” *Science*, vol. 351, no. 6268, pp. 68–70, 2016.
- [21] M. Heiranian, A. B. Farimani, and N. R. Aluru, “Water desalination with a single-layer MoS<sub>2</sub> nanopore,” *Nature Communications*, vol. 6, p. 8616, 2015.
- [22] K. Liu, J. Feng, A. Kis, and A. Radenovic, “Atomically thin molybdenum disulfide nanopores with high sensitivity for dna translocation,” *ACS Nano*, vol. 8, no. 3, pp. 2504–2511, 2014.
- [23] A. B. Farimani, K. Min, and N. R. Aluru, “DNA base detection using a single-layer MoS<sub>2</sub>,” *ACS Nano*, vol. 8, no. 8, pp. 7914–7922, 2014.
- [24] C. Wang, W. Chen, Y. Zhang, Q. Sun, and Y. Jia, “Effects of vdW interaction and electric field on friction in MoS<sub>2</sub>,” *Tribology Letters*, vol. 59, no. 1, 2015.

- [25] G. Cassabois, P. Valvin, and B. Gil, “Hexagonal boron nitride is an indirect bandgap semiconductor,” *Nature Photonics*, vol. 10, pp. 262–266, dec 2016.
- [26] M. Ishigami, J. H. Chen, W. G. Cullen, M. S. Fuhrer, and E. D. Williams, “Atomic structure of graphene on SiO<sub>2</sub>,” *Nano Letters*, vol. 7, pp. 1643–1648, June 2007.
- [27] C. H. Lui, L. Liu, K. F. Mak, G. W. Flynn, and T. F. Heinz, “Ultraflat graphene,” *Nature*, vol. 462, pp. 339–341, nov 2009.
- [28] T. T. Tran, K. Bray, M. J. Ford, M. Toth, and I. Aharonovich, “Quantum emission from hexagonal boron nitride monolayers,” *Nature Nanotechnology*, vol. 11, no. 1, pp. 37–41, 2016.
- [29] Q. Chen, H. Li, W. Xu, S. Wang, H. Sawada, C. S. Allen, A. I. Kirkland, J. C. Grossman, and J. H. Warner, “Atomically flat zigzag edges in monolayer MoS<sub>2</sub> by thermal annealing,” *Nano Letters*, vol. 17, no. 9, pp. 5502–5507, 2017.
- [30] C. Zhang, A. Johnson, C. L. Hsu, L. J. Li, and C. K. Shih, “Direct imaging of band profile in single layer MS<sub>2</sub> on graphite: Quasiparticle energy gap, metallic edge states, and edge band bending,” *Nano Letters*, vol. 14, no. 5, pp. 2443–2447, 2014.
- [31] E. Scalise, M. Houssa, G. Pourtois, V. Afanas, and A. Stesmans, “Strain-induced semiconductor to metal transition in the two-dimensional honeycomb structure of MoS<sub>2</sub>,” *Nano Research*, vol. 5, no. 1, pp. 43–48, 2012.
- [32] W. S. Yun, S. Han, S. C. H, I. G. Kim, and J. Lee, “Thickness and strain effects on electronic structures of transition metal dichalcogenides: 2H-MX<sub>2</sub> semiconductors (M = Mo, W; X = S, Se, Te),” *Physical Review B*, vol. 85, no. 3, pp. 1–5, 2012.

- [33] J. Feng, X. Qian, C. W. Huang, and J. Li, “Strain-engineered artificial atom as a broad-spectrum solar energy funnel,” *Nature Photonics*, vol. 6, no. 12, pp. 866–872, 2012.
- [34] H. Peelaers and C. G. Van De Walle, “Effects of strain on band structure and effective masses in MoS<sub>2</sub>,” *Physical Review B - Condensed Matter and Materials Physics*, vol. 86, no. 24, 2012.
- [35] S. Z. Butler, S. M. Hollen, L. Cao, Y. Cui, J. A. Gupta, H. R. Gutiérrez, T. F. Heinz, S. S. Hong, J. Huang, A. F. Ismach, E. Johnston-Halperin, M. Kuno, V. V. Plashnitsa, R. D. Robinson, R. S. Ruoff, S. Salahuddin, J. Shan, L. Shi, M. G. Spencer, M. Terrones, W. Windl, and J. E. Goldberger, “Progress, challenges, and opportunities in two-dimensional materials beyond graphene,” *ACS Nano*, vol. 7, no. 4, pp. 2898–2926, 2013.
- [36] J. Wintterlin and M. L. Bocquet, “Graphene on metal surfaces,” *Surface Science*, vol. 603, no. 10-12, pp. 1841–1852, 2009.
- [37] J. K. Cockcroft, *Space group diagrams and tables, 1997–1999* (accessed 20181202).
- [38] K. S. Novoselov, D. Jiang, F. Schedin, T. J. Booth, V. V. Khotkevich, S. V. Morozov, and A. K. Geim, “Two-dimensional atomic crystals,” *PNAS*, vol. 102, no. 30, pp. 10451–10453, 2005.
- [39] K. S. Novoselov, A. K. Geim, S. V. Morozov, D. Jiang, M. I. Katsnelson, I. V. Grigorieva, S. V. Dubonos, and A. A. Firsov, “Two-dimensional gas of massless Dirac fermions in graphene,” *Nature*, vol. 438, no. 7065, pp. 197–200, 2005.
- [40] A. H. Castro Neto, F. Guinea, N. M. R. Peres, K. S. Novoselov, and A. K. Geim, “The electronic properties of graphene,” *Reviews of Modern Physics*, vol. 81, pp. 109–162, Jan. 2009.

- [41] F. Schwabl and W. D. Brewer, *Statistical Mechanics*. Advanced texts in physics, Springer Berlin Heidelberg, 2006.
- [42] W. Tian, W. Li, W. Yu, and X. Liu, “A review on lattice defects in graphene: Types generation effects and regulation,” *Micromachines*, vol. 8, no. 5, 2017.
- [43] Y. Liu, X. Zou, and B. I. Yakobson, “Dislocations and grain boundaries in two-dimensional boron nitride,” *ACS Nano*, vol. 6, no. 8, pp. 7053–7058, 2012.
- [44] L. D. Landau, “On the theory of phase transitions. I,” *Phys. Z. Sowjet.*, vol. 11, p. 26, 1937.
- [45] V. N. Do and T. H. Pham, “Graphene and its one-dimensional patterns: From basic properties towards applications,” *Advances in natural sciences: Nanoscience and nanotechnology*, vol. 1, no. 3, pp. 33001–14, 2010.
- [46] M. B. Elinski, Z. Liu, J. C. Spear, and J. D. Batteas, “2D or not 2D? the impact of nanoscale roughness and substrate interactions on the tribological properties of graphene and MoS<sub>2</sub>,” *Journal of Physics D: Applied Physics*, vol. 50, no. 10, 2017.
- [47] A. Reina, X. Jia, J. Ho, D. Nezich, H. Son, V. Bulovic, M. S. Dresselhaus, and K. Jing, “Large area, few-layer graphene films on arbitrary substrates by chemical vapor deposition,” *Nano Letters*, vol. 9, no. 1, pp. 30–35, 2009.
- [48] X. Li, W. Cai, J. An, S. Kim, J. Nah, D. Yang, R. Piner, A. Velamakanni, I. Jung, E. Tutuc, S. K. Banerjee, L. Colombo, and R. S. Ruoff, “Large-area synthesis of high-quality and uniform graphene films on copper foils,” *Science*, vol. 324, no. 5932, pp. 1312–1314, 2009.

- [49] D. G. Papageorgiou, I. A. Kinloch, and R. J. Young, “Mechanical properties of graphene and graphene-based nanocomposites,” *Progress in Materials Science*, vol. 90, pp. 75–127, 2017.
- [50] S. Tanabe, Y. Sekine, H. Kageshima, M. Nagase, and H. Hibino, “Carrier transport mechanism in graphene on SiC(0001),” *Physical Review B - Condensed Matter and Materials Physics*, vol. 84, no. 11, 2011.
- [51] G. R. Bhimanapati, D. Kozuch, and J. A. Robinson, “Large-scale synthesis and functionalization of hexagonal boron nitride nanosheets,” *Nanoscale*, vol. 6, no. 20, pp. 11671–11675, 2014.
- [52] A. Nagashima, N. Tejima, Y. Gamou, T. Kawai, and C. Oshima, “Electronic structure of monolayer hexagonal boron nitride physisorbed on metal surfaces,” *Physical Review Letters*, vol. 75, no. 21, pp. 3918–3921, 1995.
- [53] W.-Q. Han, L. Wu, Y. Zhu, K. Watanabe, and T. Taniguchi, “Structure of chemically derived mono- and few-atomic-layer boron nitride sheets Synthesis of boron nitride nanotubes from carbon nanotubes by a substitution reaction A solid-state process for formation of boron nitride nanotubes Structure of chemically derived mono- and few-atomic-layer boron nitride sheets,” *Applied Physics Letters*, vol. 93, no. 74, pp. 223103–133107, 2008.
- [54] K. Watanabe, T. Taniguchi, and H. Kanda, “Direct-bandgap properties and evidence for ultraviolet lasing of hexagonal boron nitride single crystal,” *Nature Materials*, vol. 3, no. 6, pp. 404–409, 2004.
- [55] J. Kotakoski, C. H. Jin, O. Lehtinen, K. Suenaga, and A. V. Krasheninnikov, “Electron knock-on damage in hexagonal boron nitride monolayers,” *Physical Review B - Condensed Matter and Materials Physics*, vol. 82, no. 11, 2010.

- [56] N. Alem, Q. M. Ramasse, C. R. Seabourne, O. V. Yazyev, K. Erickson, M. C. Sarahan, C. Kisielowski, A. J. Scott, S. G. Louie, and A. Zettl, “Subangstrom edge relaxations probed by electron microscopy in hexagonal boron nitride,” *Physical Review Letters*, vol. 109, no. 20, 2012.
- [57] G. H. Ryu, H. J. Park, J. Ryou, J. Park, J. Lee, G. Kim, H. S. Shin, C. W. Bielawski, R. S. Ruoff, S. Hong, and Z. Lee, “Atomic-scale dynamics of triangular hole growth in monolayer hexagonal boron nitride under electron irradiation,” *Nanoscale*, vol. 7, no. 24, pp. 10600–10605, 2015.
- [58] C. Jin, F. Lin, K. Suenaga, and S. Iijima, “Fabrication of a freestanding boron nitride single layer and its defect assignments,” *Physical Review Letters*, vol. 102, no. 19, 2009.
- [59] A. L. Gibb, N. Alem, J. H. Chen, K. J. Erickson, J. Ciston, A. Gautam, M. Linck, and A. Zettl, “Atomic resolution imaging of grain boundary defects in monolayer chemical vapor deposition-grown hexagonal boron nitride,” *Journal of the American Chemical Society*, vol. 135, no. 18, pp. 6758–6761, 2013.
- [60] O. L. Krivanek, M. F. Chisholm, V. Nicolosi, T. J. Pennycook, G. J. Corbin, N. Dellby, M. F. Murfitt, C. S. Own, Z. S. Szilagyi, M. P. Oxley, S. T. Pantelides, and S. J. Pennycook, “Atom-by-atom structural and chemical analysis by annular dark-field electron microscopy,” *Nature*, vol. 464, no. 7288, pp. 571–574, 2010.
- [61] C. R. Dean, A. F. Young, I. Meric, C. Lee, L. Wang, S. Sorgenfrei, K. Watanabe, T. Taniguchi, P. Kim, K. L. Shepard, and J. Hone, “Boron nitride substrates for high-quality graphene electronics,” *Nature Nanotechnology*, vol. 5, no. 10, pp. 722–726, 2010.
- [62] J. Bao, K. Jeppson, M. Edwards, Y. Fu, L. Ye, X. Lu, and J. Liu, “Synthesis and applications of two-dimensional hexagonal boron nitride in electronics manufacturing,” *Electronic Materials Letters*, vol. 12, no. 1, pp. 1–16, 2016.

- [63] K. K. Kim, A. Hsu, X. Jia, S. M. Kim, Y. Shi, M. Hofmann, D. Nezich, J. F. Rodriguez-Nieva, M. Dresselhaus, T. Palacios, and J. Kong, "Synthesis of monolayer hexagonal boron nitride on Cu foil using chemical vapor deposition," *Nano Letters*, vol. 12, no. 1, pp. 161–166, 2012.
- [64] S. Najmaei, Z. Liu, W. Zhou, X. Zou, G. Shi, S. Lei, B. I. Yakobson, J. C. Idrobo, P. M. Ajayan, and J. Lou, "Vapour phase growth and grain boundary structure of molybdenum disulphide atomic layers," *Nature Materials*, vol. 12, no. 8, pp. 754–759, 2013.
- [65] J. Wu, P. Cao, Z. Zhang, F. Ning, S.-S. Zheng, J. He, and Z. Zhang, "Grain-size-controlled mechanical properties of polycrystalline monolayer MoS<sub>2</sub>," *Nano Letters*, pp. 1543–1552, 2018.
- [66] M. Chhowalla, H. S. Shin, G. Eda, L. J. Li, K. P. Loh, and H. Zhang, "The chemistry of two-dimensional layered transition metal dichalcogenide nanosheets," *Nature Chemistry*, vol. 5, no. 4, pp. 263–275, 2013.
- [67] S. G. Sørensen, H. G. Füchtbauer, A. K. Tuxen, A. S. Walton, and J. V. Lauritsen, "Structure and electronic properties of in-situ synthesized single-layer MoS<sub>2</sub> on a gold surface," *ACS Nano*, vol. 8, no. 7, pp. 6788–6796, 2014.
- [68] R. A. Neville and B. L. Evans, "The band edge excitons in mos<sub>2</sub>," *Physica Status Solidi (B)*, vol. 73, no. 2, pp. 597–606, 1976.
- [69] W. Zhou, X. Zou, S. Najmaei, Z. Liu, Y. Shi, J. Kong, J. Lou, P. M. Ajayan, B. I. Yakobson, and J. C. Idrobo, "Intrinsic structural defects in monolayer molybdenum disulfide," *Nano Letters*, vol. 13, no. 6, pp. 2615–2622, 2013.
- [70] S. W. Kim, J. H. Na, W. L. Choi, H.-J. Chung, S. H. Jhang, S. H. Choi, W. Yang, and S. W. Lee, "Patterning of periodic ripples in monolayer MoS<sub>2</sub> by using laser irradiation," *Journal of the Korean Physical Society*, vol. 69, no. 10, pp. 1505–1508, 2016.

- [71] I. Yakovkin, “Dirac cones in graphene, interlayer interaction in layered materials, and the band gap in MoS<sub>2</sub>,” *Crystals*, vol. 6, p. 143, nov 2016.
- [72] A. K. Geim and I. V. Grigorieva, “Van der Waals heterostructures,” *Nature*, vol. 499, no. 7459, pp. 419–425, 2014.
- [73] B. Lian, Z. Wang, and B. A. Bernevig, “Twisted bilayer graphene: A phonon-driven superconductor,” *Phys. Rev. Lett.*, vol. 122, p. 257002, Jun 2019.
- [74] Z. B. Aziza, H. Henck, D. Di Felice, D. Pierucci, J. Chaste, C. H. Naylor, A. Balan, Y. J. Dappe, A. T. C. Johnson, and A. Ouerghi, “Bandgap inhomogeneity of MoS<sub>2</sub> monolayer on epitaxial graphene bilayer in van der Waals p-n junction,” *Carbon*, vol. 110, pp. 396–403, 2016.
- [75] M. Yankowitz, J. Xue, D. Cormode, J. D. Sanchez-Yamagishi, K. Watanabe, T. Taniguchi, P. Jarillo-Herrero, P. Jacquod, and B. J. Leroy, “Emergence of superlattice Dirac points in graphene on hexagonal boron nitride,” *Nature Physics*, vol. 8, no. 5, pp. 382–386, 2012.
- [76] J. R. Wallbank, A. A. Patel, M. Mucha-Kruczyński, A. K. Geim, and V. I. Falko, “Generic miniband structure of graphene on a hexagonal substrate,” *Physical Review B - Condensed Matter and Materials Physics*, vol. 87, no. 24, 2013.
- [77] B. Hunt, J. D. Sanchez-Yamagishi, A. F. Young, M. Yankowitz, B. J. Leroy, K. Watanabe, T. Taniguchi, P. Moon, M. Koshino, P. Jarillo-Herrero, and R. C. Ashoori, “Massive Dirac Fermions and Hofstadter Butterfly in a van der Waals Heterostructure,” *Science*, vol. 340, pp. 1427–1430, 2013.
- [78] G. Giovannetti, P. A. Khomyakov, G. Brocks, P. J. Kelly, and J. Van Den Brink, “Substrate-induced band gap in graphene on hexagonal boron nitride: Ab initio density functional calculations,” *Physical Review B - Condensed Matter and Materials Physics*, vol. 76, no. 7, 2007.

- [79] J. Sławińska, I. Zasada, and Z. Klusek, “Energy gap tuning in graphene on hexagonal boron nitride bilayer system,” *Physical Review B - Condensed Matter and Materials Physics*, vol. 81, no. 15, 2010.
- [80] J. Sławińska, I. Zasada, P. Kosiński, and Z. Klusek, “Reversible modifications of linear dispersion: Graphene between boron nitride monolayers,” *Physical Review B - Condensed Matter and Materials Physics*, vol. 82, no. 8, 2010.
- [81] J. Xue, J. Sanchez-Yamagishi, D. Bulmash, P. Jacquod, A. Deshpande, K. Watanabe, T. Taniguchi, P. Jarillo-Herrero, and B. J. Leroy, “Scanning tunnelling microscopy and spectroscopy of ultra-flat graphene on hexagonal boron nitride,” *Nature Materials*, vol. 10, no. 4, pp. 282–285, 2011.
- [82] H. Coy Diaz, J. Avila, C. Chen, R. Addou, M. C. Asensio, and M. Batzill, “Direct observation of interlayer hybridization and dirac relativistic carriers in graphene/MoS<sub>2</sub> van der waals heterostructures,” *Nano Letters*, vol. 15, no. 2, pp. 1135–1140, 2015.
- [83] W. Yang, G. Chen, Z. Shi, C. C. Liu, L. Zhang, G. Xie, M. Cheng, D. Wang, R. Yang, D. Shi, K. Watanabe, T. Taniguchi, Y. Yao, Y. Zhang, and G. Zhang, “Epitaxial growth of single-domain graphene on hexagonal boron nitride,” *Nature Materials*, vol. 12, no. 9, pp. 792–797, 2013.
- [84] X. Liu, I. Balla, H. Bergeron, G. P. Campbell, M. J. Bedzyk, and M. C. Hersam, “Rotationally Commensurate Growth of MoS<sub>2</sub> on Epitaxial Graphene,” *ACS Nano*, vol. 10, no. 1, pp. 1067–1075, 2015.
- [85] S. J. Haigh, A. Gholinia, R. Jalil, S. Romani, L. Britnell, D. C. Elias, K. S. Novoselov, L. A. Ponomarenko, A. K. Geim, and R. Gorbachev, “Cross-sectional imaging of individual layers and buried interfaces of graphene-based heterostructures and superlattices,” *Nature Materials*, vol. 11, no. 9, pp. 764–767, 2012.

- [86] E. Khestanova, F. Guinea, L. Fumagalli, A. K. Geim, and I. V. Grigorieva, “Universal shape and pressure inside bubbles appearing in van der Waals heterostructures,” *Nature Communications*, vol. 7, 2016.
- [87] G. Argentero, R. Z. A. Mittelberger, Monazam, Y. Cao, T. J. Pennycook, C. Mangler, C. Kramberger, J. Kotakoski, A. K. Geim, and J. C. Meyer, “Unraveling the 3D Atomic Structure of a Suspended Graphene/hBN van der Waals Heterostructure,” *Nano Letters*, vol. 17, no. 3, pp. 1409–1416, 2017.
- [88] S. Ulstrup, A. Čabo Grubišić, J. A. Miwa, J. M. Riley, S. S. Grønberg, J. C. Johannsen, C. Cacho, O. Alexander, R. T. Chapman, E. Springate, M. Bianchi, M. Dendzik, J. V. Lauritsen, P. D. C. King, and P. Hofmann, “Ultrafast band structure control of a two-dimensional heterostructure,” *ACS Nano*, vol. 10, no. 6, pp. 6315–6322, 2016.
- [89] L. Britnell, R. M. Ribeiro, A. Eckmann, R. Jalil, B. D. Belle, A. Mishchenko, Y.-J. Kim, R. V. Gorbachev, T. Georgiou, S. V. Morozov, A. N. Grigorenko, A. K. Geim, C. Casiraghi, A. H. C. Neto, and K. S. Novoselov, “Strong light-matter interactions in heterostructures of atomically thin films,” *Science*, vol. 340, pp. 1311–1314, 2013.
- [90] L. Britnell, R. V. Gorbachev, R. Jalil, and B. D. Belle, “Field-effect tunneling transistor based on vertical graphene heterostructures,” *Science*, vol. 335, no. 6071, pp. 947–950, 2012.
- [91] W. J. Yu, Y. Liu, H. Zhou, A. Yin, Z. Li, Y. Huang, and X. Duan, “Highly efficient gate-tunable photocurrent generation in vertical heterostructures of layered materials,” *Nature Nanotechnology*, vol. 8, no. 12, pp. 952–958, 2013.
- [92] Y. Zhang, M. Heiranian, B. Janicek, Z. Budrikis, S. Zapperi, P. Y. Huang, H. T. Johnson, N. R. Aluru, J. W. Lyding, and N. Mason, “Strain modulation of graphene by nanoscale substrate curvatures: A molecular view,” *Nano Letters*, pp. 2098–2104, 2018.

- [93] C. Carraro and D. R. Nelson, “Grain-boundary buckling and spin-glass models of disorder in membranes,” *Physical Review E*, vol. 48, no. 4, pp. 3082–3090, 1993.
- [94] A. Fasolino, J. H. Los, and M. I. Katsnelson, “Intrinsic ripples in graphene,” *Nature Materials*, vol. 6, pp. 858–861, nov 2007.
- [95] J. Brivio, D. Alexander, and A. Kis, “Ripples and layers in ultrathin MoS<sub>2</sub> Membranes,” *Nano Letters*, vol. 11, pp. 5148–5153, Dec. 2011.
- [96] O. Lehtinen, S. Kurasch, A. V. Krasheninnikov, and U. Kaiser, “Atomic scale study of the life cycle of a dislocation in graphene from birth to annihilation,” *Nature Communications*, vol. 4, 2013.
- [97] J. H. Warner, E. R. Margine, M. Mukai, A. W. Robertson, F. Giustino, and A. I. Kirkland, “Dislocation-driven deformations in graphene,” *Science*, vol. 337, pp. 209–212, jul 2012.
- [98] J. H. Warner, Y. Fan, A. W. Robertson, K. He, E. Yoon, and G. D. Lee, “Rippling graphene at the nanoscale through dislocation addition,” *Nano Letters*, vol. 13, no. 10, pp. 4937–4944, 2013.
- [99] V. Geringer, M. Liebmann, T. Echtermeyer, S. Runte, M. Schmidt, R. Rückamp, M. C. Lemme, and M. Morgenstern, “Intrinsic and extrinsic corrugation of monolayer graphene deposited on SiO<sub>2</sub>,” *Physical Review Letters*, vol. 102, no. 7, pp. 1–4, 2009.
- [100] Y. Wei, J. Wu, H. Yin, X. Shi, R. Yang, and M. Dresselhaus, “The nature of strength enhancement and weakening by pentagong-heptagon defects in graphene,” *Nature Materials*, vol. 11, no. 9, pp. 759–763, 2012.
- [101] Y. Zhang, V. W. Brar, C. Girit, A. Zettl, and M. F. Crommie, “Origin of spatial charge inhomogeneity in graphene,” *Nature Physics*, vol. 5, no. 10, pp. 722–726, 2009.

- [102] S. Rajput, Y.-Y. Li, M. Weinert, and L. Li, “Indirect interlayer bonding in graphene— topological insulator van der Waals heterostructure: Giant spin—orbit splitting of the graphene Dirac states,” *ACS Nano*, vol. 10, pp. 8450–8456, 2016.
- [103] R. Decker, Y. Wang, V. W. Brar, W. Regan, H. Z. Tsai, Q. Wu, W. Gannett, A. Zettl, and M. F. Crommie, “Local electronic properties of graphene on a BN substrate via scanning tunneling microscopy,” *Nano Letters*, vol. 11, no. 6, pp. 2291–2295, 2011.
- [104] P. Blake, E. W. Hill, A. H. Castro Neto, K. S. Novoselov, D. Jiang, R. Yang, T. J. Booth, and A. K. Geim, “Making graphene visible,” *Applied Physics Letters*, vol. 91, no. 6, p. 063124, 2007.
- [105] R. V. Gorbachev, I. Riaz, R. R. Nair, R. Jalil, L. Britnell, B. D. Belle, E. W. Hill, K. S. Novoselov, K. Watanabe, T. Taniguchi, A. K. Geim, and P. Blake, “Hunting for monolayer boron nitride: Optical and Raman signatures,” *Small*, vol. 7, no. 4, pp. 465–468, 2011.
- [106] M. H. Khan, Z. Huang, F. Xiao, G. Casillas, Z. Chen, P. J. Molino, and H. K. Liu, “Synthesis of large and few atomic layers of Hexagonal boron nitride on melted copper,” *Scientific Reports*, vol. 5, 2015.
- [107] M. Xu, T. Liang, M. Shi, and H. Chen, “Graphene-like two-dimensional materials,” *Chemical Reviews*, vol. 113, no. 5, pp. 3766–3798, 2013.
- [108] Y. Stehle, H. M. Meyer, R. R. Unocic, M. Kidder, G. Polizos, P. G. Datskos, R. Jackson, S. N. Smirnov, and I. V. Vlassiouk, “Synthesis of hexagonal boron nitride monolayer: Control of nucleation and crystal morphology,” *Chemistry of Materials*, vol. 27, no. 23, pp. 8041–8047, 2015.
- [109] Y.-H. Lee, T.-W. Lin, C.-S. Chang, K.-D. Chang, W. Zhang, Y.-C. Yu, X.-Q. Zhang, M.-T. Chang, L.-J. Li, J. T.-W. Wang, and C.-T. Lin, “Syn-

- thesis of large-area MoS<sub>2</sub> atomic layers with chemical vapor deposition,” *Advanced Materials*, vol. 24, no. 17, pp. 2320–2325, 2012.
- [110] D. B. Williams and C. B. Carter, *Transmission electron microscopy: A textbook for materials science*. No. Bd. 2 in Cambridge library collection, Springer, 2009.
- [111] P. A. Doyle and P. S. Turner, “Relativistic Hartree–Fock X-ray and electron scattering factors,” *Acta Crystallographica Section A*, vol. 24, pp. 390–397, may 1968.
- [112] W. Zhou, M. P. Oxley, A. R. Lupini, O. L. Krivanek, S. J. Pennycook, and J. C. Idrobo, “Single atom microscopy,” in *Microscopy and Microanalysis*, vol. 18, pp. 1342–1354, 2012.
- [113] T. C. Lovejoy, Q. M. Ramasse, M. Falke, A. Kaepfel, R. Terborg, R. Zan, N. Dellby, and O. L. Krivanek, “Single atom identification by energy dispersive x-ray spectroscopy,” *Applied Physics Letters*, vol. 100, no. 15, pp. 154101–211913, 2012.
- [114] K. Suenaga, T. Okazaki, E. Okunishi, and S. Matsumura, “Detection of photons emitted from single erbium atoms in energy-dispersive X-ray spectroscopy,” *Nature Photonics*, vol. 6, no. 8, pp. 545–548, 2012.
- [115] R. Erni, *Aberration-corrected imaging in transmission electron microscopy: An introduction*. ICP/Imperial College Press, 2010.
- [116] S. Yamashita, J. Kikkawa, K. Yanagisawa, T. Nagai, K. Ishizuka, and K. Kimoto, “Atomic number dependence of Z contrast in scanning transmission electron microscopy,” *Scientific Reports*, vol. 8, no. 1, p. 12325, 2018.
- [117] K. Suenaga and M. Koshino, “Atom-by-atom spectroscopy at graphene edge,” *Nature*, vol. 468, no. 7327, pp. 1088–1090, 2010.

- [118] J. Cazaux, “Correlations between ionization radiation-damage and charging effects in transmission electron-microscopy,” *Ultramicroscopy*, vol. 60, no. 3, pp. 411–425, 1995.
- [119] I. G. Gonzalez-Martinez, A. Bachmatiuk, V. Bezugly, J. Kunstmann, T. Gemming, Z. Liu, G. Cuniberti, and M. H. Rummeli, “Electron-beam induced synthesis of nanostructures: a review,” *Nanoscale*, vol. 8, no. 22, pp. 11340–11362, 2016.
- [120] G. T. Leuthner, S. Hummel, C. Mangler, T. J. Pennycook, T. Susi, J. C. Meyer, and J. Kotakoski, “Scanning transmission electron microscopy under controlled low-pressure atmospheres,” *Ultramicroscopy*, 2019.
- [121] K. Ishizuka, “Coma-free alignment of a high-resolution electron microscope with three-fold astigmatism,” *Ultramicroscopy*, vol. 55, no. 4, pp. 407–418, 1994.
- [122] J. Hillier and R. F. Baker, “Microanalysis by means of electrons,” *Journal of Applied Physics*, vol. 15, no. 9, pp. 663–675, 1944.
- [123] J. Ping and M. S. Fuhrer, “Layer number and stacking sequence imaging of few-layer graphene by transmission electron microscopy,” *Nano Letters*, vol. 12, no. 9, pp. 4635–4641, 2012.
- [124] V. Ronchi, “Due nuovi metodi per lo studio delle superficie e dei sistemi ottici,” *Annali della Scuola Normale Superiore di Pisa - Classe di Scienze*, vol. Ser. 1, 15, pp. 1–50, 1927. talk:1.
- [125] A. R. Lupini, P. Wang, P. D. Nellist, A. I. Kirkland, and S. J. Pennycook, “Aberration measurement using the Ronchigram contrast transfer function,” *Ultramicroscopy*, vol. 110, no. 7, pp. 891–898, 2010.
- [126] J. H. Warner, Y.-C. Lin, K. He, M. Koshino, and K. Suenaga, “Atomic level spatial variations of energy states along graphene edges,” *Nano Letters*, vol. 14, no. 11, pp. 6155–6159, 2014.

- [127] W. Zhou, J. Lee, J. Nanda, S. T. Pantelides, S. J. Pennycook, and J. C. Idrobo, “Atomically localized plasmon enhancement in monolayer graphene,” *Nature Nanotechnology*, vol. 7, no. 3, pp. 161–165, 2012.
- [128] W. Zhou, M. D. Kapetanakis, M. P. Prange, S. T. Pantelides, S. J. Pennycook, and J. C. Idrobo, “Direct determination of the chemical bonding of individual impurities in graphene,” *Physical Review Letters*, vol. 109, no. 20, 2012.
- [129] W. Zhou, S. J. Pennycook, and J. C. Idrobo, “Localization of inelastic electron scattering in the low-loss energy regime,” *Ultramicroscopy*, vol. 119, pp. 51–56, 2012.
- [130] Y. C. Lin, D. O. Dumcenco, Y. S. Huang, and K. Suenaga, “Atomic mechanism of the semiconducting-to-metallic phase transition in single-layered MoS<sub>2</sub>,” *Nature Nanotechnology*, vol. 9, no. 5, pp. 391–396, 2014.
- [131] J. C. Meyer, F. Eder, S. Kurasch, V. Skakalova, J. Kotakoski, H. J. Park, S. Roth, A. Chuvilin, S. Eyhusen, G. Benner, A. V. Krashenninnikov, and U. Kaiser, “Accurate measurement of electron beam induced displacement cross sections for single-layer graphene,” *Physical Review Letters*, vol. 108, no. 19, pp. 1–6, 2012.
- [132] M. R. A. Monazam, U. Ludacka, H.-P. Komsa, and J. Kotakoski, “Substitutional Si impurities in monolayer hexagonal boron nitride,” *Appl. Phys. Lett*, vol. 115, p. 71604, 2019.
- [133] C. Koch, “Determination of core structure periodicity and point defect density along dislocations,” 2002.
- [134] F. Langenhorst and V. L. Solozhenko, “ATEM-EELS study of new diamond-like phases in the B–C–N system,” *Phys. Chem. Chem. Phys.*, vol. 4, no. 20, pp. 5183–5188, 2002.
- [135] R. F. Egerton and M. J. Whelan, “The electron energy loss spectrum and band structure of diamond,” *The Philosophical Magazine: A Journal of*

- Theoretical Experimental and Applied Physics*, vol. 30, no. 4, pp. 739–749, 1974.
- [136] T. Susi, J. Madsen, U. Ludacka, J. J. Mortensen, T. J. Pennycook, Z. Lee, U. Kaiser, and J. C. Meyer, “Efficient first principles simulation of electron scattering factors for transmission electron microscopy,” *Ultramicroscopy*, vol. 197, pp. 16–22, 2018.
- [137] S. Plimpton, “Fast parallel algorithms for short-range molecular dynamics,” *Journal of Computational Physics*, vol. 117, no. 1, pp. 1 – 19, 1995.
- [138] S. Plimpton and A. P. Thompson, “Computational aspects of many-body potentials,” *MRS Bulletin*, vol. 37, pp. 513–521, 5 2012.
- [139] S. P. Coleman, D. E. Spearot, and L. Capolungo, “Virtual diffraction analysis of ni [010] symmetric tilt grain boundaries,” *Modelling and Simulation in Materials Science and Engineering*, vol. 21, p. 055020, 2013.
- [140] J. H. Los and A. Fasolino, “Intrinsic long-range bond-order potential for carbon: Performance in monte carlo simulations of graphitization,” *Physical Review B*, vol. 68, p. 024107, Jul 2003.
- [141] M. Tripathi, A. Mittelberger, K. Mustonen, C. Mangler, J. Kotakoski, J. C. Meyer, and T. Susi, “Cleaning graphene: Comparing heat treatments in air and in vacuum,” *Physica Status Solidi - Rapid Research Letters*, vol. 11, no. 8, 2017.
- [142] C. Lee, X. Wei, J. W. Kysar, and J. Hone, “Measurement of the elastic properties and intrinsic strength of monolayer graphene,” *S. R. Ortner, Acta Metall. Mater*, vol. 54, p. 635, 2008.
- [143] H. S. Seung and D. R. Nelson, “Defects in flexible membranes with crystalline order,” *Physical Review A*, vol. 38, no. 2, pp. 1005–1018, 1988.
- [144] M. Friedrich and U. Stefanelli, “Ripples in graphene: A variational approach,” 2018.

- [145] J. Kotakoski, F. R. Eder, and J. C. Meyer, “Atomic structure and energetics of large vacancies in graphene,” *Physical Review B - Condensed Matter and Materials Physics*, vol. 89, no. 20, pp. 1–6, 2014.
- [146] T. Susi, C. Hofer, G. Argentero, G. T. Leuthner, T. J. Pennycook, C. Mangler, J. C. Meyer, and J. Kotakoski, “Isotope analysis in the transmission electron microscope,” *Nature Comm.*, vol. 7, p. 13040, 2016.
- [147] F. R. Eder, J. Kotakoski, U. Kaiser, and J. C. Meyer, “A journey from order to disorder - atom by atom transformation from graphene to a 2D carbon glass,” *Scientific reports*, vol. 4, p. 4060, 2014.
- [148] T. Latychevskaia, C. R. Woods, Y. B. Wang, M. Holwill, E. Prestat, S. J. Haigh, and K. S. Novoselov, “Convergent beam electron holography for analysis of van der Waals heterostructures,” *PNAS*, vol. 115, no. 29, pp. 7473–7478, 2018.
- [149] G. Algara-Siller, S. Kurasch, M. Sedighi, O. Lehtinen, and U. Kaiser, “The pristine atomic structure of MoS<sub>2</sub> monolayer protected from electron radiation damage by graphene,” *Applied Physics Letters*, vol. 1036012045, no. 134, 2013.